FROM GENE EXPRESSION TO BEHAVIOR: A STUDY IN BACTERIAL CELLS

by

Jing He

B.S. in Physics, Beijing Normal University, 2009

Submitted to the Graduate Faculty of

the Kenneth P. Dietrich School of Arts and Sciences in partial

fulfillment

of the requirements for the degree of

Doctor of Philosophy

University of Pittsburgh

2016

UNIVERSITY OF PITTSBURGH

KENNETH P. DIETRICH SCHOOL OF ARTS AND SCIENCES

This dissertation was presented

by

Jing He

It was defended on

July 14th 2016

and approved by

Xiao-Lun Wu, Department of Physics and Astronomy

Hanna Salman, Department of Physics and Astronomy

David Jasnow, Department of Physics and Astronomy

Joseph Boudreau, Department of Physics and Astronomy

Robert Duda, Department of Biological Sciences

Dissertation Director: Xiao-Lun Wu, Department of Physics and Astronomy

FROM GENE EXPRESSION TO BEHAVIOR: A STUDY IN BACTERIAL CELLS

Jing He, PhD

University of Pittsburgh, 2016

Gene expression plays an important role in cell metabolism, motility, and replications. Using fluorescence microscopy, I found that the expression profile of LamB, an *Escherichia coli* outer membrane protein, is unimodal in cell cytosol. The bimodal distribution of λ phage, which binds to LamB receptors on the outer membrane, should result from the heterogeneity in protein export and assembly processes. The study also estimates the burst-like LamB expression to have a mean bursting rate of 9.4 bursts per cell-cycle and a mean bursting number of 82 copies per burst. In another study on bacterial growth curves, I unexpectedly discovered that depletion of 4 amino acids (arginine, methionine, isoleucine, and glycine) can cause diauxie-like growth arrests, which last for 5 to 30 minutes depending on the amino acids used. As a quantitative measure of response times of gene regulations upon starvation, this technique could potentially provide a simple and robust means to determine the time constants in metabolic networks of a variety of bacteria. Normal expression of genes is also significant for robust bacterial swimming and chemotaxis. I observed strikingly that very small *Vibrio alginolyticus* cells are able to reorient by a π-flip (180^{o}) in $\sim$ 60 ms, but this ability is gradually lost when the cell size becomes larger. I also observed that in a *cheY* deletion mutant of *V. alginolyticus*, over expression of CheY, or its phosphorylated form CheY-p, significantly diminishes the mutant's ability to change swimming directions. To understand how *Vibrio alginolyticus* reorients during a flick, H. Fu came up with a dynamic model incorporating flagellar off-axial rotation during a flick and I performed the calculation. Comparing the model prediction with the experiment, my observations are consistent with

the physical picture that *V. alginolyticus*' flagellum follows some closed path Σ on the surface of a unisphere characterized by the polar θ and azimuthal ϕ angles. Fitting the data of *cheY* deletion mutant using this model suggests the possibility of motor remodeling and "stiffening" when CheY concentration is increased.

TABLE OF CONTENTS

LIST OF TABLES

LIST OF FIGURES

1.0 INTRODUCTION

From bacteria to animals, from basic metabolisms in maintaining living states to replication or reproduction in generating offspring, or from motility patterns in food hunting and repellent evasion to human's sophisticated intellectual works, gene expression provides building blocks that constitute organisms and controls every aspect of biological activities in an organism's lifetime. In this dissertation, I present studies related to bacterial gene expression, gene regulation, and chemotactic motility controlled by normal and abnormal gene expressions.

From the notion of inheritable "genes" first conceived by Mendel in 1865, which determines phenotypes of organisms, to the discovery of DNA double helix structure by Watson and Crick in 1952, scientists for the first time found the substance which carries genetic information. These findings form the foundations for modern genetics and molecular biology. According to the Central Dogma of molecular biology, DNA molecules are firstly transcribed into messenger RNA (mRNA) by RNA polymerases, and then translated into amino acid peptides by ribosomes. In this way, information coded on DNA molecules is used to produce protein peptides, which provide structural components, such as organelles for motility and pores for transport small molecules, enzymes for biochemical reactions, and machinary for transcription and translation in living cells. From one generation to the next generation, the genetic information is inherited through DNA by replications, in which the double strands unwind, and a new DNA strand is synthesized by DNA polymerases in complementary to the old strand.

Although every cell shares the same genetic information, gene expression may have a huge cell-to-cell variation in an isogenic population. The mean protein copy number N inside a population is approximately equal to the product of the average mRNA copy number per cell cycle and the average copy of protein molecules produced per mRNA [2]. N is also

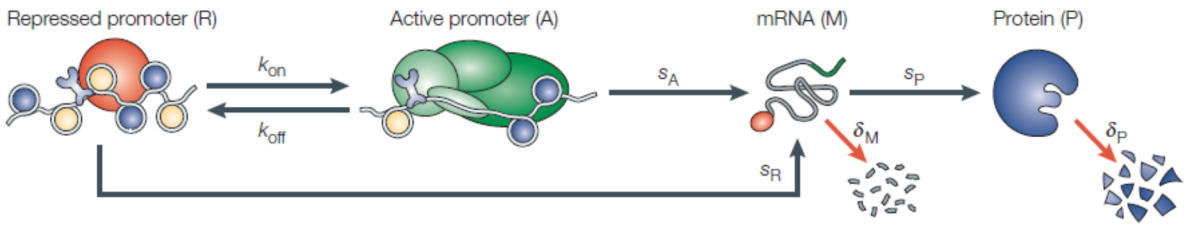

Figure 1.1: A Model of the Expression of a Single Gene. Here k_{on} and k_{off} are promoter ON and OFF rates, s_{A}, s_{R}, and s_{P} are transcription rate in promoter ON state, in promoter OFF state, and translation rate, respectively. δ_{M} and δ_{P} are mRNA and protein degradation rates. Adapted from Kaern et al. (2005) [1].

proportional to the product of transcription rate (s_{A}) and translation rate (s_{P}) [2]. The relative deviation from the mean is termed noise $\eta = \sigma/N$, where σ is the standard deviation.

Stochastic gene expression can result from an intrinsic noise, where different numbers of proteins are produced from the same concentrations of transcriptional factors, RNA polymerases, and ribosomes, or from extrinsic noise, where their concentrations are different. Elowitz, et al. showed that by increasing the induction level of a protein, the intrinsic noise η decreases as $1/\sqrt{N}$ as the transcription rate increases [3]. In another work, Ozbudak et al. showed that the noise strength increases linearly with protein abundance by increasing translation rate [4]. In general, for two populations with the same protein abundance, the one with a smaller mRNA number and higher translation rate is subject to higher gene-expression noise (standard deviation divided by mean $\frac{\sigma}{N}$) compared to the other with a higher mRNA number and a lower translation rate. It is generally expected that a fluctuation in mRNA copy number will enhance fluctuations in the rate of protein synthesis, and thus increase the gene expression noise [1].

Genes and proteins form networks to transfer stimuli to responses. Noise propagates in such a network as well. In general, a network with a negative feedback loop reduces protein number fluctuations in a population whereas a positive feedback loop increases such fluctuations. A network with a strong positive feedback loop often causes bistability [5],

such as an all-or-none kind of phenotype [6]. Multistability can play an important role in differentiation of multicellular organisms and in bacterial survival under an environmental stress.

An operon is a cluster of genes which are transcribed into one single mRNA under the control of a single promoter. The well studied *lac* operon contains 3 genes: *lacZ*, *lacY*, and *lacA*, which encode for β-galactosidase, lactose permease, and galactoside O-acetyltransferase, respectively. β-galactosidase and permease are responsible for lactose metabolism and transport. In the absence of glucose, a metabolite of lactose inactivates *lac* repressor, and induces the expression of lactose permease and galactosidase, which generates a higher concentration of the lactose metabolite, forming a positive feedback loop. As discussed above, strong positive feedback in gene regulations can result in bistability in gene expression levels [5]. A bimodal distribution of proteins expressed from *lac* operon was observed when induced by a non-metabolizable inducer, TMG [7, 6].

In Chapter 2, I will discuss the stochastic expression of the *lamB* gene product, which is a maltose outer membrane transporter of *E. coli*. LamB is located in *mal* regulon, which consists of 10 genes on 5 operons related to the transport and metabolism of maltose and maltodextrin [8]. In comparison to an operon, a regulon consists of a group of genes controlled by the same activator or repressor. However, genes on the same regulon may locate at different loci on the chromosome. The 5 operons in the maltose regulon are controlled by the activator MalT and a global transcription factor cAMP/CRP [8].

Bacteria have different faculties to deal with environmental stresses [9]. It is thought that stochastic gene expression is one way to prepare a cell population to cope with an unforeseen environmental stress. This is a biologically economical strategy and is effective for a rapid changing environment. Another way is for a bacterium to sense the environment and make corresponding changes in gene expressions. Since sensing and regulation of genes are biologically costly, this strategy is more effective for a bacterium to cope with an environment that changes slowly or in a timely ordered fashion. Evolution is believed to be the engine behind the continuous remodeling of biological pathways that enable organisms to survive under different conditions.

Catabolite repression is one example of gene regulations. When bacteria are supplied

with multiple carbon sources, like glucose, lactose, and maltose, *E. coli* would preferentially consume glucose first. Its molecular mechanism is delineated in Fig. E1. In the presence of glucose, glucose is transported into the cell through the phosphotransferase system (PTS), which leaves most enzyme IIA in a unphosphorylated state. Unphosphorylated EIIA is unable to activate adenylate cyclase, which leaves the intracellular cyclic AMP concentration low. When cAMP concentration is low, catabolic activator protein (CAP) remains in an inactive form. Genes activated by cAMP/CAP complexes, like *lac* and *mal* operons remain repressed. These genes are related to carbon transport and utilizations. A classic phenomenon related to catabolic repression is the diauxie effect. It was discovered by Jacques Monod and was reported in his PhD thesis (1941). Monod measured *E. coli* growth curves in media containing a pair of sugars and one of them is glucose [10]. *E. coli* grows rapidly in the initial phase when consuming glucose. Upon glucose depletion, the growth comes to a stop, which lasted for tens of minutes to hours before growth resumes. In the refractory period, the bacterium activates genes required for metabolizing the second sugar. The ecological rationale behind diauxie and catabolite repression is that the utilization of glucose is more efficient requiring fewer enzymes.

When studying *E. coli* growth curves, I found a new "growth-stop" phase. Unlike the classical diauxic effect, the phenomenon involves amino acid biosyntheses upon amino acid starvation. Similar to the role of CAP or cAMP that is produced in large amounts in response of glucose depletion, when amino acid is depleted, a signal molecule ppGpp is produced. It up and down regulates a group of genes, and prepares *E. coli* to internally synthesize amino acids that are in shortage. In Chapter 3, I'm going to discuss this phenomenon and its implications.

Sugar and amino acids are important nutrients for bacteria. They are the energy sources as well as the essential building blocks for all cell's components. It is amazing that through millions years of evolution, bacteria developed efficient means to utilize carbon sources and to synthesize amino acids. However, to understand how these regulatory networks come into being and how a bacterium optimize its energy budget remain significant challenges.

Living in a real world instead of in a culture tube, bacteria usually have to actively search for nutrients and evade hazardous chemicals. This is realized by its powerful flagella,

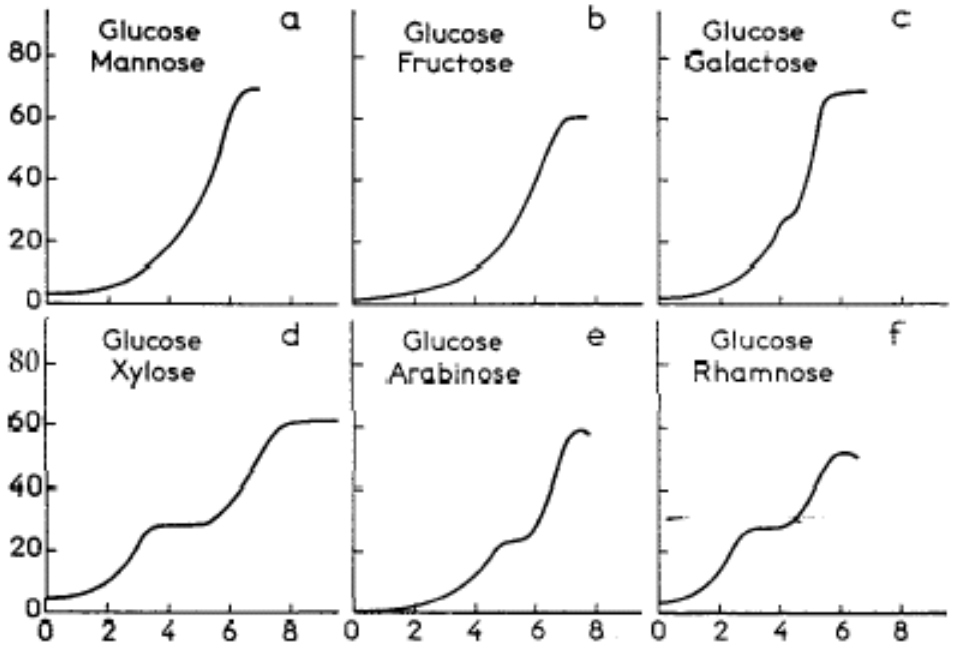

Fig.1. Growth of *Escherichia coli* in the presence of different carbohydrate pairs serving as the only source of carbon in a synthetic medium[50].

Figure 1.2: Monod's Original Diauxie Growth Curves. Sugar pairs are annotated in each plot. The x axis is in unit of hours, and y axis is the optical density with some unclear units. This figure is adapted from Wikipedia on Diauxie.

which are driven by the motors at their bases. A group of genes (*mot*, *flg*, *fli*, and *fla*) are responsible for the synthesis and assembly of flagella and flagellar motors [11]. The *che* gene products are responsible for regulating flagellar rotation directions, and they steer bacteria in liquids toward regions rich in nutritions [12].

There are a variety of bacterial motility patterns. In the most studied case, *Escherichia coli* swims in a run-tumble fashion (see Fig. 1.3). *E. coli* has 4-10 flagella around the cell body [13]. When all flagella are rotating in a counter clockwise (CCW) direction, they form a bundle and propel the cell body forward. This is called a "run interval". When any of these flagella reverses its rotation direction to clockwise (CW), the bundle falls apart and the bacterium tumbles around. During the tumbling interval, bacteria change its swim direction and is ready for the next run [12].

This motility pattern is regulated by *E. coli* chemotaxis network as shown in Fig. 1.4. The attractant or repellent concentrations are sensed by a protein assembly consisting of receptors, CheW, and histidine kinase CheA. The autophosphorylation activity of CheA decreases upon attractant binding and increases upon repellent binding. CheA transfers its phosphoryl group to CheY and CheB. The phosphorylated CheY molecules (CheY-p) diffuse to flagellar motors, and increases the probability of the motor to switch from the default CCW rotation, which is the run state, to the CW rotation, which is the tumble state. CheZ catalyzes CheY-p dephosphorylation process to ensure a rapid response. The phosphorylated CheB (CheB-p) removes methyl groups on receptors, which decreases CheA phosphorylation activity. On the other hand CheR transfers methyl groups onto the receptor, which increases CheA activity and increases its sensitivity to attractants. CheR and CheB are responsible for chemotaxis adaptations, which keeps bacteria sensitive to a large range of ligand concentrations [15, 12].

As a result, upon increased attractant binding, CheA becomes less active. CheY-p concentration decreases, and the motor tumbles less. Bacteria swim with elongated run intervals. On the other hand, upon repellent binding, CheA becomes more active, which increases CheY-p concentration, and induces more tumbling events [15, 12].

Different from *E. coli*'s run-and-tumble motility pattern, marine bacteria *Vibrio alginolyticus* adopts a run-reverse-flick swim pattern (see Fig. 4.1(A) in Chapter 4). When

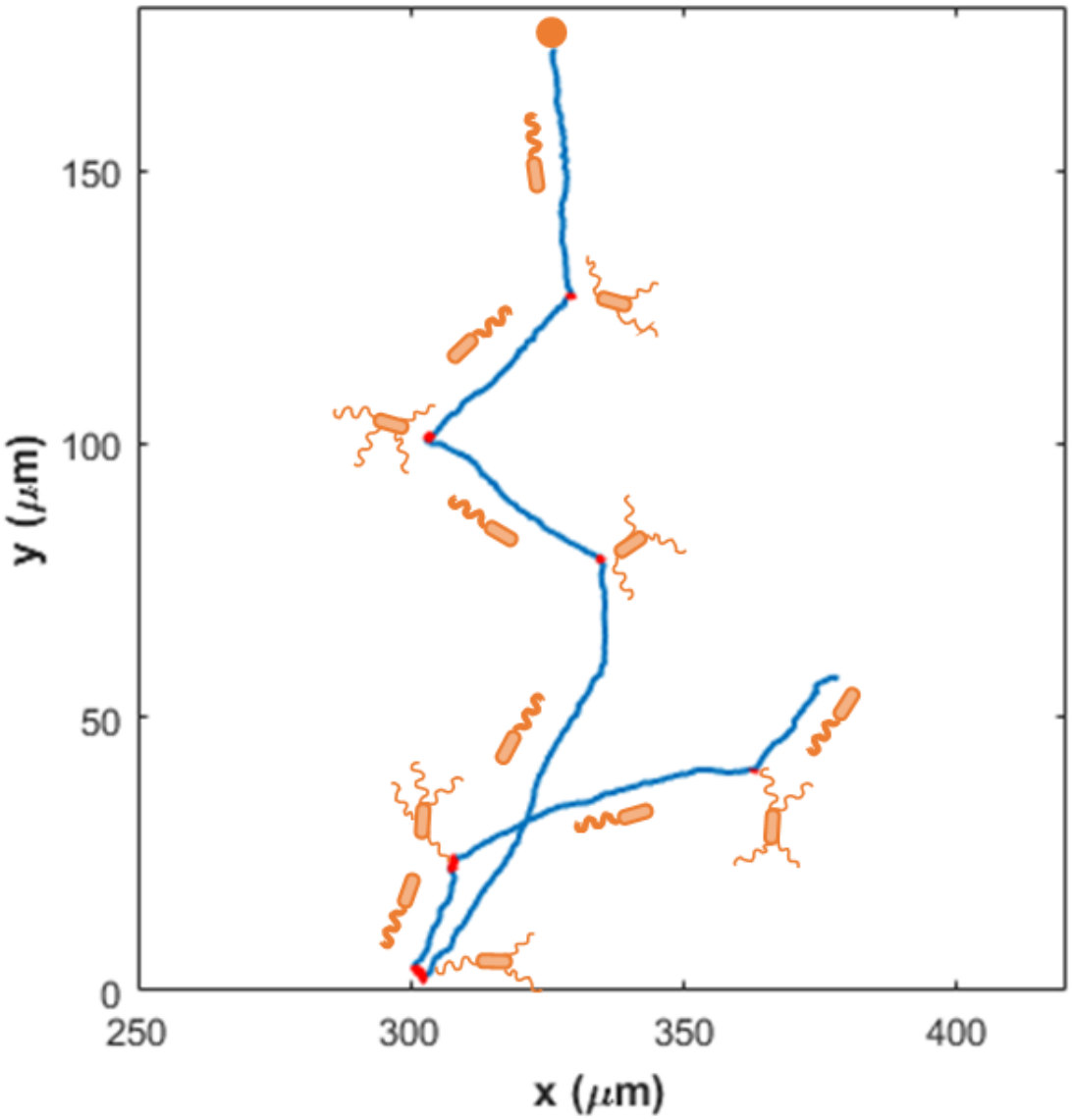

Figure 1.3: *Escherichia coli* Motility Pattern. A typical *E. coli* swim trajectory is labeled with blue "run" segments and red "tumble" segments. The starting point is labeled as an orange dot. This bacterium was swimming at 24.9 μm/s in motility buffer [14]. The bacterial size is not to scale.

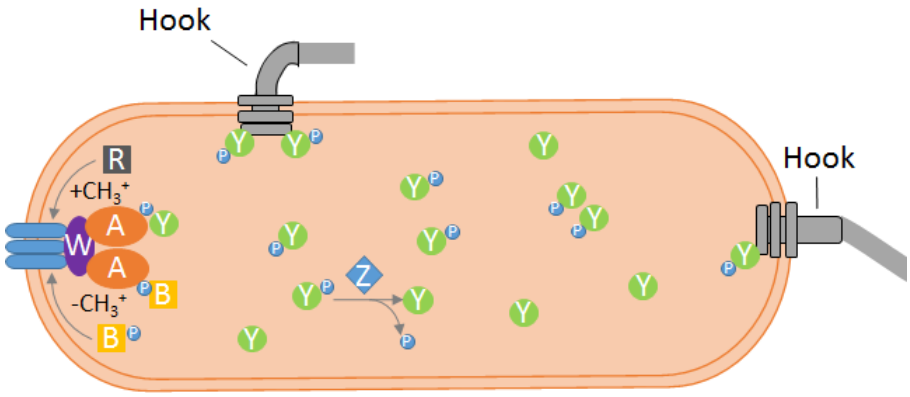

Figure 1.4: Chemotaxis Network. CheW, CheA, CheY, CheZ, CheR, and CheB proteins are shown in purple, orange, green, blue, black, and yellow colors. Also shown in the plot are one *Escherichia coli* peritrichous flagellum and one *Vibrio alginolyticus* polar flagellum. Flagellar hooks are highlighted with black outlines, which connects flagellum to the motor. *E. coli* has a curved hook, while the hook of *V. alginolyticus* is straight [16, 17].

living in liquids, *V. alginolyticus* develops one sheathed polar flagellum, and it is regulated by a chemotaxis network similar to the one shown in Fig. 1.4. The CCW and CW rotations of a polar flagellum would only drive the cell to move in a straight line, forward or backward. Our group found that at the backward to forward transitions, the flagellum conducts an off-axis rotation around its base, which reorients the cell body to a new random direction with a most probable reorientation angle being around 90° [18]. This is called a "flick". A work by Son et al. (2013) [19] showed that the flick happens at $\sim 10\,\mathrm{ms}$ after the onset of a forward swimming interval, and bacteria with low speed and large cell size are less likely to "flick". They deduced that the flick results from an instability in the flagellar hook. A hook connects a bacterial flagellum to its motor, which is illustrated in Fig. 1.4. It translates the motor torque to the flagellum. Since a swimming bacterium is a free body, its cell body and flagellum are rotating in opposite directions to conserve the total angular momentum. The flagellar hook is twisted tightly in forward and backward runs. However, at the backward-to-forward transition, the hook is loose and subject to a pushing force and

a torque. According to the buckling instability criteria shown in Eq. (1.1), the hook will buckle when the load (a combination of torque T and force F) exceeds critical values (T_{cr} and F_{cr}) [20].

$$\frac{F}{F_{cr}} + \left(\frac{T}{T_{cr}}\right)^2 > 1, \tag{1.1}$$

where $F_{cr} = \pi^2 \frac{EI}{L^2}$, and $T_{cr} = 2\pi \frac{EI}{L}$. EI is the bending stiffness of the hook with E being the elastic modulus, and I being the area moment of inertia of the flagellar cross-section. In this model, the hook length L is an important parameter in determining the critical force and torque. An electron microscope (EM) measurement assured that the hook length of *V. alginolyticus* is stringently controlled and is around $97.3 \pm 10.6\,\text{nm}$. Fig. 5.3 shows the EM pictures of hooks of *V. alginolyticus*. Prof. Hughs from University of Utah discovered a hook-length-control mechanism in which the hook length is determined by the length of a flagellar secreted protein FliK [21].

The buckling instability model provides a possible mechanism for flagellar off-axis rotation. However, it is not clear how such an off-axis rotation causes cell-body reorientation. In experiments, I found *V. alginolyticus* occasionally can reorient by 180° if the cell-body size is sufficiently small. In Chapter 4, this question is explained by a dynamic model introduced by Prof. Fu of University of Nevada (personal communications). The dynamic model also predicts a cell body reorientation angle and displacement when the path of a flagellar off-axis rotation is predefined and agrees reasonably well with my measurements using wild-type *V. alginolyticus*.

As shown in Fig. 1.4, the chemotaxis network of wild-type *E. coli* is carefully modulated by appropriate concentration and activity of chemotactic proteins. When CheY concentration is increased by over induction with a constant CheA activity, CheY-p concentration will rise. It is expected that the net effect is that the flagellar motor will switch more frequently compared to the wild-type bacterium but nothing else will happen. However this is not what was found. In Chapter 5, I describe an experiment in which the effect of CheY over-expression in *V. alginolyticus* is studied. I found that in addition to increased motor switching rate, bacteria with large amounts of CheY-p are less likely to reorient the cell body in large angles, suggesting that the bacterial basal body may be modified by the over-

expression of CheY. The stiffening of the basal body can affect flagellar off-axis rotation and hence a reduced ability for the cell body to alter directions.

Gene expression, bacterial behavior, and their regulatory networks are highly dynamic and complex. Physicists may use mathematical models and physical principles to shine new light on stochastic gene expression and bacterial motility. In this thesis, I'm going to present my studies of gene expression and regulation in the second and third chapters. A flagellar off-axis rotation model is described in the fourth chapter to explains the bacterial reorientation during a flick. In the fifth chapter, this model will be utilized to predict the reduced flagellar off-axis rotation amplitude due to an increased CheY-p concentration.

2.0 STOCHASTIC EXPRESSION OF OUTER MEMBRANE PROTEIN LAMB

2.1 INTRODUCTION

Living in an environment that undergoes perpetual changes in temperature, pH, salinity, and availability of nutrients, bacteria developed their own strategies to cope with the fluctuating environment and to optimize their chance of survival. However the responses of cells in a population to an environmental change are often very heterogeneous. An archetypal case is when a population bifurcates into two subpopulations with one responding to the change but the other not. When this happens, more often than not, the regulatory system in a cell that makes such a stochastic decision is bistable. It was shown that certain regulatory networks consisting of a positive feedback, double-negative feedback, or combinations of different feedbacks together with non-linear responses, can generate bistability [2].

In *Escherichia coli, lac* operon consists of 3 genes, which play important roles in lactose transport and metabolism: *lacZ*, encoding β-galactosidase; *lacY*, encoding lactose permease; and *lacA,* encoding a transacetylase. The expression of *lac* genes is repressed by the repressor LacI, which can be inactivated by allolactose, a metabolite of lactose, or by IPTG/TMG, a non-metabolizable analog of allolactose. High concentration of lactose leads to accumulation of allolactose inside a cell, which in turn inhibits the activity of LacI, and elevates the *lac* operon expression, including lactose permease gene *lacY*. Thus, it constitutes a positive feedback loop. When induced at intermediate levels by gratuitous inducers (IPTG/TMG), *lac* genes are highly expressed in only a fraction of a population, whereas in the rest of the population the expression level remains low, which forms a stable bimodal distribution. Here, the coexistence of two subpopulations involves the positive feedback regulation [7, 22].

Another naturally occurring bistability is the bifurcation of *E. coli* into lytic and lysogenic pathways after a cell is infected by bacteriophage λ. The key elements in this switch are the transcriptional regulators Cro and CI. The CI protein represses genes that are required for phage propagation while stimulates its own expression, whereas Cro represses one of the two promoters that drives the expression of *cI*. This forms a double-negative regulatory circuit [23]. The last example is for *Bacillus subtilis*. For this bacterium, the competence for genetic transformation involves only a part of the population ($\sim 10\,\%$). ComK is the transcriptional factor that regulates more than 100 genes responsible for DNA binding and uptaking. ComK binds to its own promoter as a dimer of dimers, and is required for its own expression. This forms a positive feedback loop. Experiments have shown that the bimodal distribution depends on this positive auto-regulatory feedback loop [24, 25].

The maltose system of *E. coli* is a typical catabolite-sensitive regulon [26]. It consists of eleven genes encoding proteins for uptake and metabolism of maltose and maltodextrins [8]. These genes are specifically and positively controlled by an activator MalT. Expression of *malT*, as well as of some, but not all, *mal* genes, is under control of the cAMP-CAP-dependent catabolite repression as well as by Mlc, a global negative regulator of carbohydrate metabolism [26]. A maltose metabolite, maltotriose, and ATP are required for the activation of MalT. An increase in the active MalT concentration enhances *mal* gene expression, including maltose transport gene *lamB*, and maltotriose synthesis genes *malPQZ*, which further increases the active MalT concentration, and forms a positive feedback regulation loop. Appendix E shows the response of maltose regulon in the presence of glucose or maltose.

The work presented in this chapter is motivated by Emily Chapman's observation that binding of λ phage on the outer membrane protein LamB is strongly heterogeneous [27] (see Fig. 2.1) . The large variation in the phage binding affinity was postulated as the cause of a persistent population that can evade a λ phage attack [27]. However, on the cell surface, a phage only recognizes mature receptors. From gene expression to mature receptors, several biophysical steps are involved, such as transcription; translation; translocation of prematured polypeptide across the inner membrane; insertion into the outer membrane; trimerization; and finally becoming functional [28]. Each of these steps can potentially introduce cell-to-cell

variability as seen in Chapman's experiment. The current experiment is designed to quantify the variation in the first two steps of gene expression, transcription and translation. The experimental result presented below indicates that the large heterogeneity, in particular the presence of a minority population seen in Chapman's experiment, is not due to the noise in *lamB* gene expression, but from protein export and assembly processes.

2.2 EXPERIMENT

To quantify LamB expression level inside *E. coli* strain LE392, I constructed a strain JH1 in which a yellow fluorescent protein (*yfp*) gene *venus* [29] was inserted after *lamB* on the chromosome of LE392 (See Appendix B for experimental details). The gene construct is shown in Fig. 2.2. Since *lamB* and *venus* are transcribed into one mRNA, and have the same ribosome binding site (RBS) sequences, which confers the same ribosome recruiting ability during translation, the expression level of LamB is well correlated to the expression level of Venus, and can be measured through the fluorescence intensity or the concentration of Venus.

2.2.1 Bistability

The fluorescence intensity of maltose-induced JH1 cells is shown in Fig. 2.3, where two separate expriments were conducted. In the first experiment with more than 9×10^4 cells (Fig. 2.3(A)), a subpopulation shows up as a small peak around fluorescence intensity 1300 A. U. (arbitrary unit), and majority of the cells forms a peak around 4900 A. U., suggesting that the maltose regulon might be bistable. The small population of dark cells occupies $\sim 4.7\,\%$ of the whole population. Fig. 2.4 displays some dark cells identified in this experiment using fluorescence microscopy. However, in the second experiment where propidium iodide was used to distinguish dead cells (see Appendix C for methods), there's no dark cell population. All cells reside in the bright population as shown in Fig. 2.3(B).

If all the cells in the small population of Fig. 2.3(A) are low-expressing cells, according

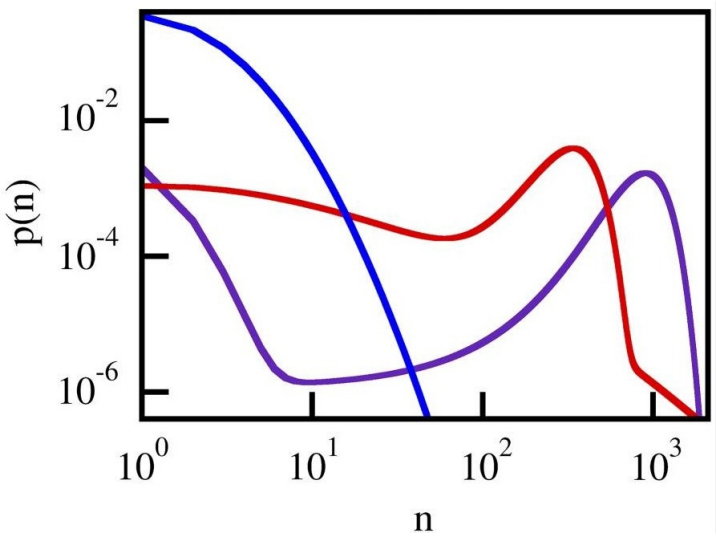

Figure 2.1: Recepter-Bound Phage Number Distributions. Fluorescent λ phages were used to display LamB receptor number (n) per cell. The probability density curves $p\,(n)$ correspond to uninduced LE392 (*blue*), Ymel (*red*) (*mel-1*, *supF58*, *tyrT58*, *su+ III*) with less LamB recepters, and induced LE392 (*purple*) bacteria. This figure is adapted from Chapman-McQuiston et al. (2008) [27].

Figure 2.2: Gene Construct of Strain JH1. A copy of *venus* gene was inserted in the *malK-lamB-malM* operon on *E. coli* chromosome. To ensure that Venus reports LamB expression level correctly, I replicated *lamB*'s RBS for *venus*, which is shown as an orange stripe in the graph.

to the statistics, there should be around 100 dark cells in the second experiment. Now that, we don't see any dark cells in the second experiment of 2500 cells, the dark cell population if ever exist, should be no more than 0.04 %. That is, no more than 36 dark cells in the small population shown in Fig. 2.3(A).

2.2.2 Autofluorescence Deconvolution

Almost all cells are autofluorescent due to aromatic amino acids inside them [30]. To eliminate the unwanted contributions from autofluorescence in the Venus intensity measurements, a control experiment was carried out to calibrate the autofluorescence of strain LE392 (see Fig. 2.5(A)). The total fluorescence (Fig. 2.3(A)) and autofluorescence (Fig. 2.5(A)) are normalized, and the resulting probability density functions (or histograms) $p_{total}(I)$ and $p_{auto}(I)$ are deconvoluted using Eq. (2.1). The deconvoluted Venus fluorescence intensity distribution $p_{net}(I)$ is shown in Fig. 2.5(B), where the dark (around 0) and bright (around 4000 A. U.) cell subpopulations persist.

$$p_{net}(I) = \int_{I}^{\infty} dI' p_{total}(I')\, p_{auto}(I' - I) \tag{2.1}$$

2.2.3 Bursting Statistics

According to Golding et al. (2005) [31], *E. coli* genes switch between ON and OFF states with exponentially distributed intervals. The number of mRNA transcripts produced in the ON state follows a geometric distribution. In general, the ON states are separated by exponentially distributed OFF intervals. Since only a few mRNA transcripts are produced in an ON state and such states are sparsely distributed, it is described as a burst-like transcription. A burst-like gene expression model is described by Friedman et al. (2006) [5]. It suggests that the distribution $p(x)$ of a given protein in a population of cells satisfies a Gamma distribution,

$$p(x) = \frac{1}{b^a \Gamma(a)} x^{a-1} e^{-x/b}, \tag{2.2}$$

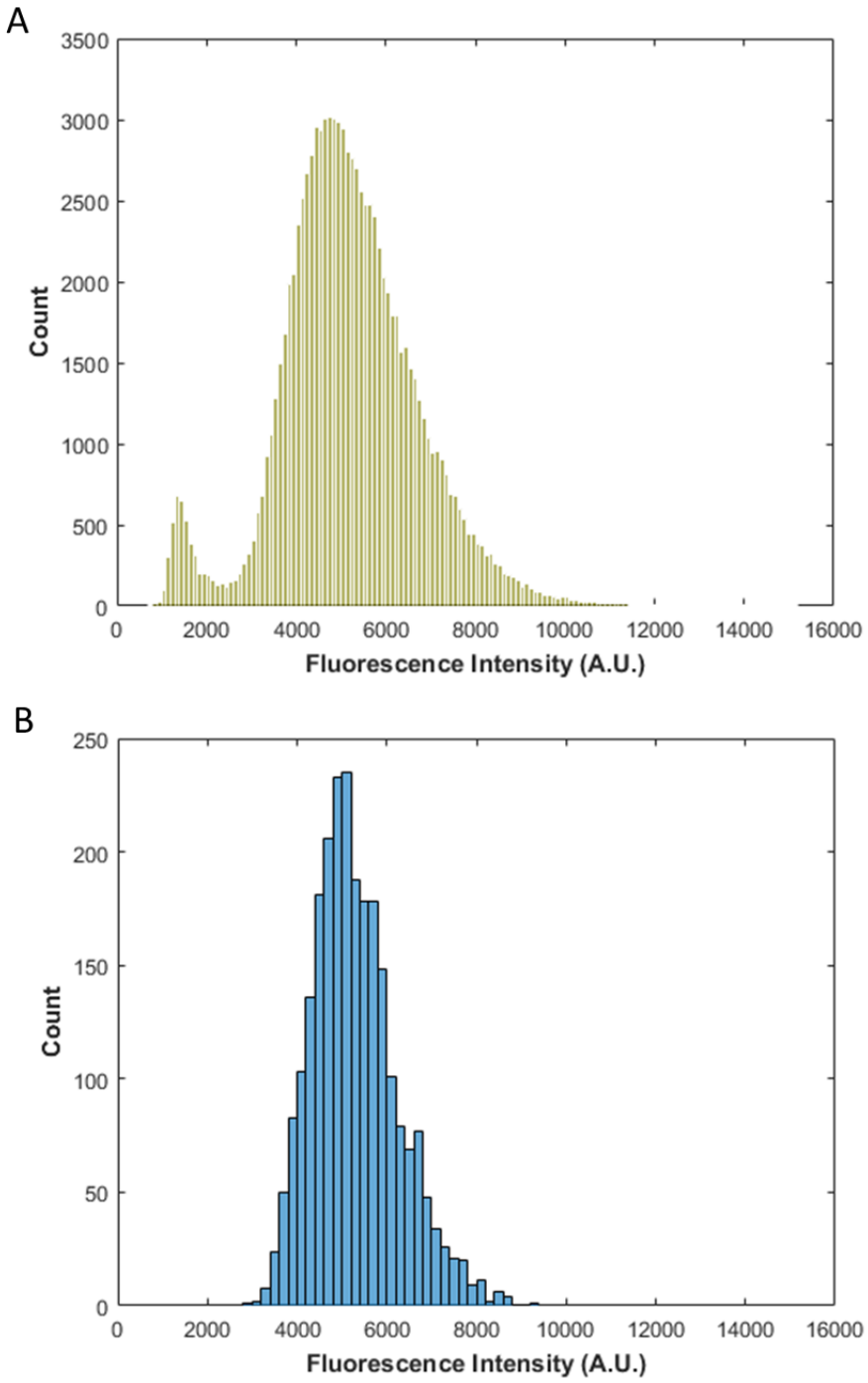

Figure 2.3: Pixel Fluorescence Intensity Histograms. Each count in a histogram represents the average fluorescence intensity of all pixels within one cell. (A) Experiment I includes more than 9×10^4 cells. (B) Experiment II includes a population of ~ 2500 cells, where dead cells are excluded.

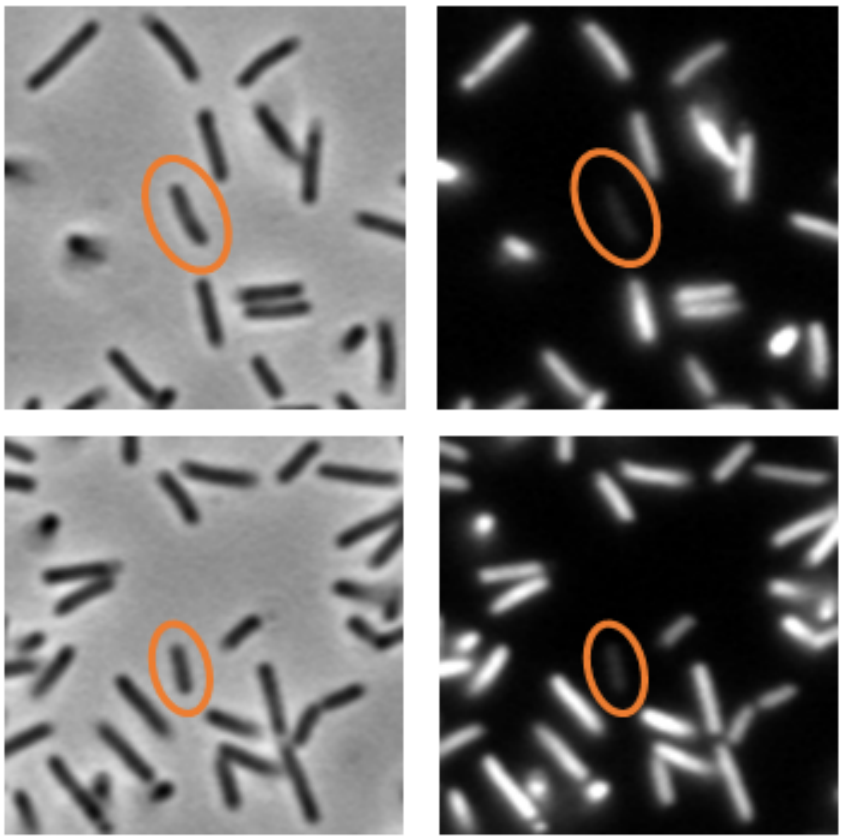

Figure 2.4: Dark Cells (circled in orange) are observed under phase contrast and fluorescence microscopy.

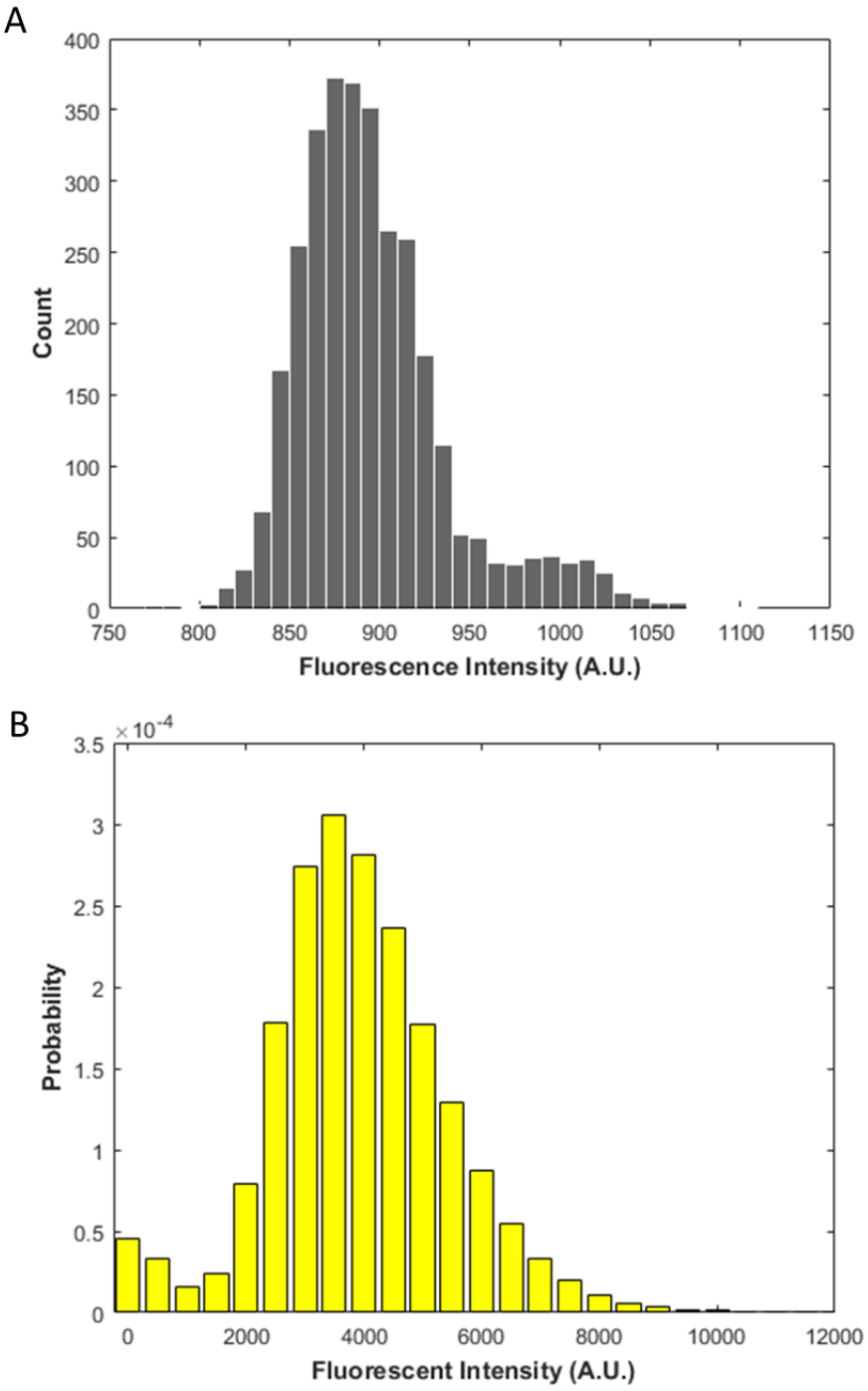

Figure 2.5: Averaged Fluorescence and Copy Number Distributions. All the quantities presented here are cell pixel averaged values. Autofluorescence from a control group of LE392 cells is shown in (A). The autofluorescence is deconvoluted from Fig. 2.3(B). The resulting net YFP fluorescence intensity distribution is shown in (B).

where $x\,(t)$ is the concentration of that protein inside a cell, a is the mean number of bursts per cell life-cycle, and b is the mean number of protein molecules produced in each burst divided by the cell volume or area. b shares the same unit with x, that is, (protein) copy number per pixel area in my experiment. To extract the burst-like features in LamB expression, the large population in Fig. 2.3(A) is fitted with the Gamma function shown in Eq. (2.2). Similar results follows when the data in Fig. 2.3(B) is used. To transform the fluorescence into protein copy numbers, a single-molecule fluorescence measurement was conducted to calibrate the intensity of a single Venus molecule (See Appendix D). Fig. 2.6(A) shows a typical Venus cluster photobleaching curve, where each step corresponds to one fluorophore bleaching event. The intensity of one Venus fluorophore is measured to be 500 ± 26 A. U. under the illumination condition of that day. Microspheres with fixed fluorescence intensity were used to calibrate the illumination variations from day to day. After taking illumination variations into account, the fluorescence intensity of a single Venus molecule is estimated to be around 337 ± 18 A. U.. Using this result, the fluorescence intensity in Fig. 2.5(B) is converted into Venus copy number, as shown in Fig. 2.6(B). It describes the Venus copy number concentration (per pixel area) distribution in a population of maltose-induced JH1 cells. For a cell of an average area ~ 60 pixel area, and with a most probable Venus concentration ~ 10 copy/pixel area, it has around 600 copy of Venus proteins inside the cell. The bright cell population in Fig. 2.6(B) is fitted with the burst model [5], which yields $a = 9.383$, $b = 1.281$. Namely, in a bacterial life-cycle, on average $a \approx 9.4$ bursts happen, and in each burst, $b\bar{A} \approx 82$ molecules of Venus protein are produced, where $\bar{A} = 64.4$ is the averaged cell area in pixels. This result is consistent with Taniguchi's measurement [32]. They got $a = 6.36$, $b\bar{A} = 14.5$ for *malK*, which is on the same operon, and shares the same promoter with *lamB* (see Fig. 2.2). The six fold difference in $b\bar{A}$ may come from different ribosome binding site strength of *lamB* and *malK*.

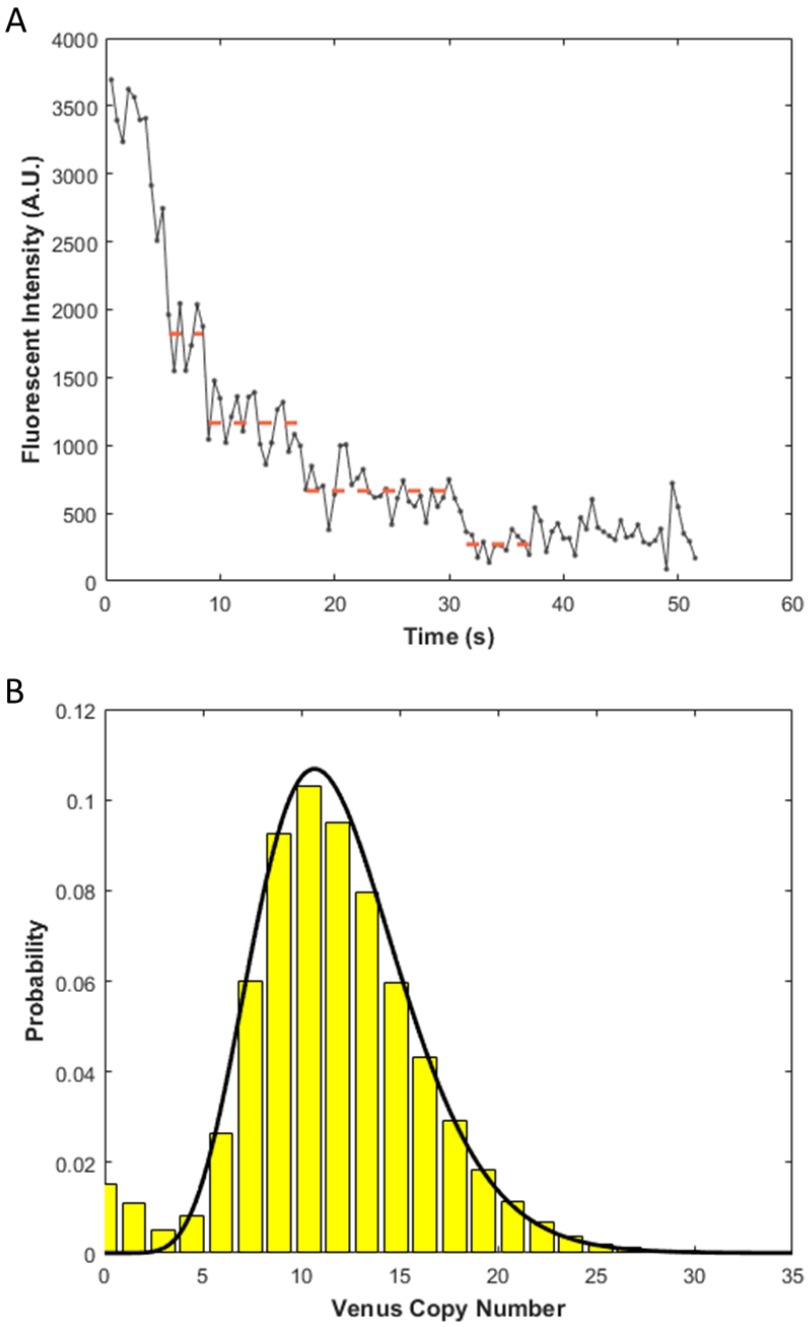

Figure 2.6: (A) A Tsr-Venus Cluster Photobleach Cuve. A gift strain SX4 from Xie's lab [33] was used for this measurement. The curve is presented after background and autofluorescence subtractions. Orange dashed lines show the step positions for a guide of eye. (B) The fluorescence intensity is transformed into Venus copy number per pixel per cell, and its distribution is fitted with a Gamma gene bursting curve [5]. On average each cell occupies 64.4 pixel area (0.16 μm/pixel).

2.3 DISCUSSION

In Chapman's paper (2008) [27], they reported that 0.7% of induced LE392 population had less than 2 copies of LamB receptors per cell. However, my fluorescence measurement suggested that dark cells should contitute no more than 0.04% of the population, which is 16 fold smaller than that in Chapman's measurement. Cells with less than 2 receptors per cell (or 0.03 copy of Venus per pixel) would take a fraction even smaller than 0.04%. Thus, the bimodal distribution observed in Chapman's experiment can not be explained by the stochastical noise in transcription and translation processes.

For LamB to be functional on the outer membrane, additional biophysical steps, such as transport, maturation, and assembly, are required. As seen in Fig. 2.7 [28], at least 13 proteins are involved in the LamB assembly process from its precurser form in cytosol to correctly assembled trimers on the outer membrane. Any of these proteins getting under-expressed, folded incorrectly, or malfunctioning may decrease the amount LamB receptors on the outer membrane. This might reduce the number of functional receptors in a minority of cells and explain the bimodal distribution seen in the phage binding experiment [27]. Although this minority of cells is partially malnutritious with a low maltose-uptake rate, it may help the whole population survive from phage attacks, and overall improves a population health.

2.4 MATERIAL AND METHODS

Strain: LE392 (F-, Δ*(codB-lacI)3*, *glnX44*(AS), *galK2*(Oc), *galT22*, λ^-, *tyrT58*(AS), *metB1*, *hsdR514*, *trpR55*). Strain JH1 was constructed from LE392 by inserting a *venus* (Excitation: 515 nm, Emission: 528 nm) gene behind *lamB* using $\lambda -$ Red recombination technique [34]. *venus* has its own RBS, which is a replicate of *lamB* RBS. Appendix B describes detailed steps for the construction of strain JH1.

Growth Conditions: LE392 and JH1 were grown overnight in M9 minimal medium (6.78 g/L Na_2HPO_4, 3 g/L KH_2PO_4, 1 g/L NH_4Cl, 0.5 g/L NaCl, 0.4% Maltose, 2 mM $MgSO_4$,

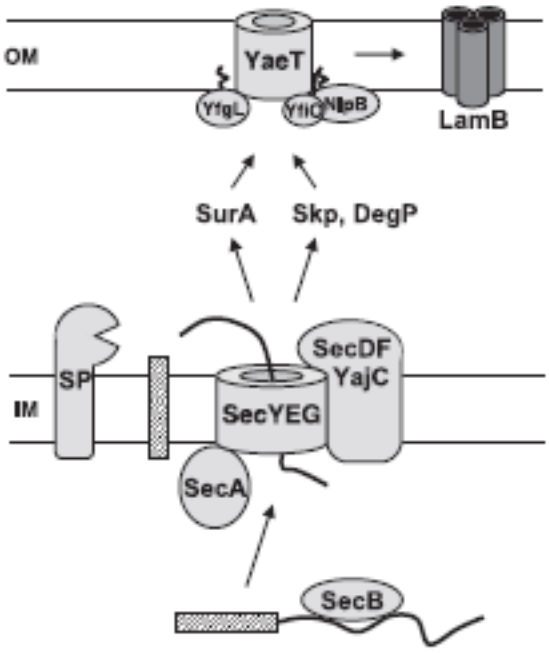

Figure 2.7: LamB Assembly Pathway. LamB precursers are synthesized in cell cytosol with a signal sequence in the amino terminal. SecB works as a cytosolic chaperone, which keeps LamB unfolded in a transport-competent conformation, and delivers it to the inner membrane transportation machinary SecYEG. In the periplasm, chaperon SurA or Skp and DegP delivers LamB to the outer membrane assembly machine YaeT, YfgL, YfiO, and NlpB. Adapted from Ureta, et al. (2007) [28].

0.1 mM $CaCl_2$). The overnight culture was diluted 1:100 fold in fresh M9 medium (maltose), and then grow to midlog $OD_{600} = 0.2$ ($\sim 4\,\mathrm{hr}$).

Slide Preparation: The midlog cells were washed twice in 0.85% NaCl solution, concentrated, and then incubated on poly-L-lysine (Sigma, Mol. Wt. 150,000-300,000, 0.01% solution) coated coverslips (Fisher Scientific) for 30 min. The slide was washed in NaCl solution for several times, and then assembled into a chamber for microscopic observations.

Microscopic Observation: All the pictures were taken using Nikon TE300 inverted microscope. Fluorescence images were captured using Hamamatsu C9100 camera with a fluorescence filter set consisting of a dichroic mirror q515lp, an excitation filter hq500-40x, and an emission filter hq545-40m (Chroma). The exposure time was 0.5 s for the fluorescence pictures.

Image Processing: A phase contrast image and a fluorescence image were taken for each field of view. Cell contours are identified on the phase-contrast image using a self-developed MATLAB script, which also collects cellular area, major and minor axis lengths information. The mean fluorescence intensity of each identified cell is extracted from the fluorescence picture, and was plotted in Fig. 2.3.

3.0 AMINO ACID "DIAUXIE" EFFECT OBSERVED IN *E. COLI*

3.1 INTRODUCTION

Carbon utility and amino acid biosynthesis are important subjects and have been studied for a long time in simple organisms such as bacteria and in high-level organisms such as humans. Amino acid biosynthesis is a set of biochemical processes, catabolic and anabolic together known as metabolic activities, by which different amino acids are produced from other compounds. Unlike human, which can only synthesize 8 out of 20 amino acids and all others, called essential amino acids, have to be supplemented from food, bacteria such as *E. coli* have the unusual ability to synthesize all amino acids needed to support growth. A fundamental problem for biological systems is to obtain nitrogen in an easily usable form. This problem is solved by certain microorganisms capable of reducing the inert nitrogen gas in the environment to molecules of ammonia in one of the most remarkable reactions in biochemistry. Ammonia is the source of nitrogen for all the amino acids. The carbon backbones come from the glycolytic pathway, the pentose phosphate pathway or the citric acid cycle. The availability of carbon and nitrogen is represented by the cAMP level inside a cell as shown in Fig. 3.1. A very beautiful recent work conducted in Prof. Hwa's lab at UCSD has illustrated how the carbon and nitrogen afflux in *E. coli* cells is sensed and regulated by cAMP [35].

Biosynthetic pathways are highly regulated such that the building blocks are synthesized only when supplies are low. This promotes the notion that "each amino acid is its own suppressor" meaning that when extracellular concentration of an amino acid is above a threshold value, the cell shuts down the pathway that is responsible for the synthesis of this amino acid. Such a strategy saves energy because making amino acids is energetically

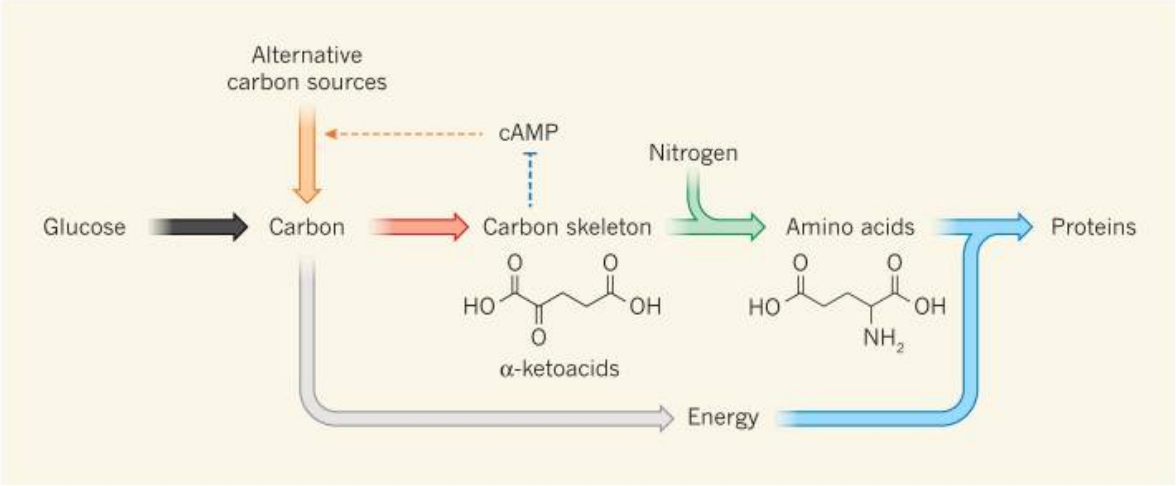

Figure 3.1: Carbon Utility and Protein Synthesis Pathway in Bacteria. The main biosynthetic task of the bacterium *Escherichia coli* is protein production. This requires energy generation (grey arrow), carbon-skeleton synthesis, nitrogen incorporation to make amino acids, and protein synthesis. The anabolic fluxes (red, green and blue arrows) increase linearly with growth rate, as does the required anabolic proteome fraction except for processes that are directly slowed by nutrient limitation (such as amino-acid synthesis during nitrogen limitation). Carbon catabolism provides energy and building blocks for anabolism, and cAMP allocates the proper fraction of the proteome to carbon-catabolic enzymes. Adopted from J.D. Rabinowitz and T.J. Silhavy, Nature (2013).

costly [36, 37, 38]. Since most amino acids are made in a hierarchical fashion, often a high concentration of the final product of a pathway inhibits the activity of enzymes that function early in the pathway.

Most information we know today about the metabolic reactions and pathways is gained by genetic studies of metabolically impaired bacteria and by biochemical analyses of metabolites at different stages of synthesis [39, 40, 41]. In this thesis I would like to report new observations that perhaps are reasonably well understood by biochemists, but they are novel nonetheless and potentially a very useful tool for a quick peek into complicated metabolic pathways in a variety of bacteria. Specifically I study how the presence of certain amino acids affects growth of *E. coli* K12 under the condition when carbon is not restricting.

Traditional growth curve measurement using a spectrometer is rather crude, and it does not have the sensitivity nor the time resolution required for the study. What makes the measurement possible is a state-of-the-art multi-well plate reader (Tecan, infinite M200) that provides temperature control, aeration by shaking, and accurate reporting of O.D. in a large number of samples. In an attempt to reproduce the classical diauxie effect [42, 43, 44] in *E. coli* LE392, a strain used in our early experiment to investigate lamB and λ-phage interaction, we performed the measurement using the 96-well plate reader in Prof. Salman's lab. The M9 medium was supplemented by 0.005% glucose, 0.05% of maltose, and 0.1% of casamino acids. The composition of casamino acids is shown in Table (3.1). The classical experiment by F. Jacob and J. Monod used glucose and lactose in a growth medium, and their study of how bacteria grew in such medium led to the discovery of *lac* operon and the 1965 Nobel prize [10]. Subsequent work demonstrated that in the presence of glucose many sugars exhibit the same effect, showing that different sugars are consumed by the microorganism at different times and glucose is the most preferred one. Indeed, we observed the classic two-step growth, which is delineated in Fig. 3.2. *E. coli* LE392 consumed glucose first and followed by maltose. The switch occurred at t $\sim$ 100 min as indicated by the black arrow. Surprisingly, in this data a short delay in growth also appeared at t $\sim$ 300 min, which is totally unexpected. Despite noise in the measurement, the delay, which is marked with a purple arrow, is present in every well used in the measurement. We found that the delay is independent of the maltose concentration in the medium as long as its carrying capacity is

large enough (¿0.01% maltose) as seen in the graph. It is interesting to note that while the bacterium took about 100 min to adapt to the new carbon source, from 100 to $\sim$ 200 min, the small delay lasted for only about 10 minutes. Moreover, we also noticed that the growth rates γ, the slopes on the graph, just prior and just after the growth delay are about the same, yielding the doubling time $\left(\gamma_{1/2}\right)^{-1}\left(=\frac{\ln 2}{\gamma}\right) \sim 130\,\text{min}$. This is not the case in the classical diauxic effect, such as glucose-to-maltose switching as seen at $t \simeq 100$ min.

In retrospect, the above finding is very fortuitous in that such a miniature feature was captured in our first trial and was immediately recognized; this small anomaly would most likely be ignored if the observation were not made in a plate reader that offered parallel runs with many identical replicates and a sufficiently fine time resolution.

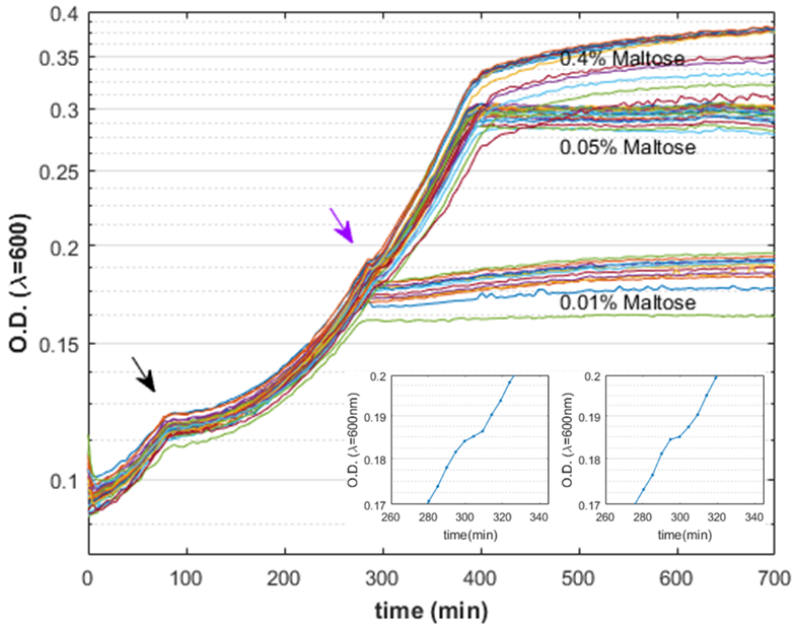

Figure 3.2: Growth Curves of LE392 in M9 media supplemented with mixtures of glucose and maltose. Various amount of maltose (w/v: 0.01%, 0.05%, and 0.4%) and a fixed amount of glucose (w/v: 0.005%) was added into M9 minimal medium as the carbon source. For each maltose concentration, 24 wells were measured and plotted. The inserts provide a closer look of the kinks in two separate wells. The time separation between two successive points is 290 s.

To ascertain what we have seen is intrinsic to bacterial metabolism but not some arti-

fact, control experiments were conducted to show: (i) the growth delay is not due to the specific carbon source used in the measurement. The data in Fig. 3.3 indicates that growth arrest occurs for LE392 grown in glucose, maltose, glycerol, but not in LB rich medium. (ii) The effect is not restricted to LE392 but can be seen in MG1655 strain, which is the model *E. coli* strain for metabolic studies (data not shown) [45, 46, 47]. Putting together all the above findings, amino acid starvation appeared to be a reasonable explanation. I performed painstaking measurements by systematically eliminating amino acids in the growth medium. I eventually singled out a single amino acid, arginine, in the M9 medium to be solely responsible for the delay seen in Fig. 3.2. Most importantly I further showed that by adding arginine to the growth medium M9, the delay can be moved to a later time on the growth curve, which is demonstrated in Fig. 3.4.

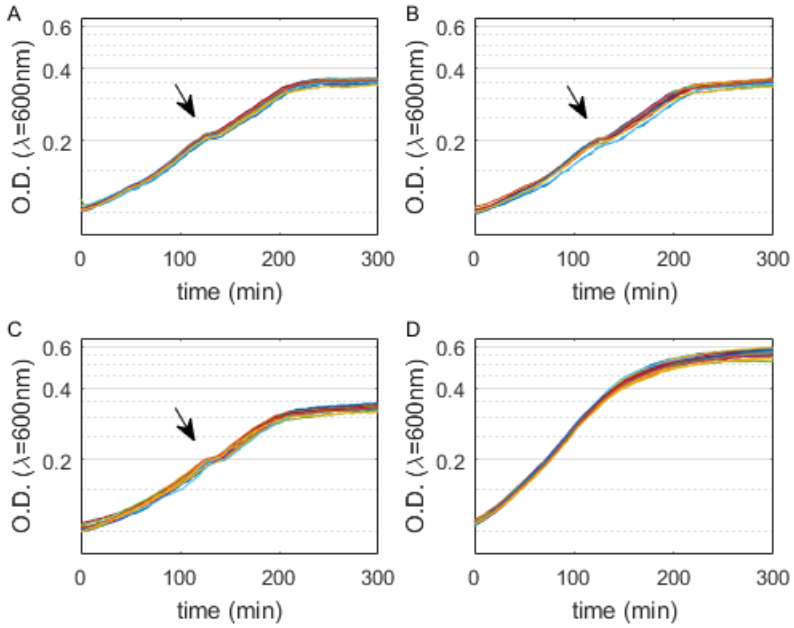

Figure 3.3: Strain LE392 was grown in the minimal medium supplemented with maltose (w/v: 0.2%) (A); glucose (w/v: 0.5%) (B); glycerol (w/v: 0.2%) (C); and in LB rich medium (D). The arrows indicate the beginning positions of the transition. 24 growth curves are plotted under each condition.

The next question we asked is the generality of the phenomenon. Do all individual amino

acids produce a delay in *E. coli* growth when it is depleted in the extracellular medium? In order to address this question, we first need to know whether LE392 is capable of making all twenty amino acids for protein synthesis. To find out, measurements were carried out in M9 that contains only glucose, again 0.4%, and no amino acid. The data displayed in Fig. 3.5(A) makes it clear that LE392 is capable of synthesizing all amino acids for growth, and interestingly the growth curve is smooth, showing no growth arrest of the kind displayed in Figs. 3.2 - 3.4. This behavior is consistent with the prevailing view that "each amino acid is its own repressor".

Motivated by the above observations, systematic measurements were conducted in the growth medium, M9+0.4%-glucose, containing only a single amino acid. Some rather striking effects were observed in this case. The most outstanding effect happened when valine is present as the sole amino acid. We found that even a tiny amount of it can completely suppress growth, behaving almost like an antibiotic, as shown in Fig. 3.5(B). However, such a repression can be relieved by doping the growth medium with a small amount of isoleucine, which is shown in Fig. 3.5(C). This is an amazing effect, and made us very excited. Unfortunately we soon found out that the phenomenon was known and well understood. According to Umbarger [48], valine produces feedback inhibitions on acetohydroxy acid synthase (AHAS), which is an enzyme essential for isoleucine biosynthesis. The addition of isoleucine immediately reverses the inhibition. This striking effect is not universal in all bacteria, and appears to be specific to *E. coli* K12. *E. coli* K12 has three different AHAS enzymes: AHAS I (ilvBN) uses pyruvate exclusively for the production of valine, AHAS II (ilvGM) uses pyruvate and α-ketobutyrate for the production of isoleucine, and AHAS III (ilvIH) catalyze both reactions but favors pyruvate and α-ketobutyrate as substrates. Both AHAS I and III are feedback inhibited by valine. K-12 strains of *E. coli* harbor a frame-shift mutation in the ilvG gene, which renders the AHAS II enzyme inactive. Thus, when isoleucine is limiting and valine is in excess, AHAS I and III are inhibited, causing the bacterium unable to synthesize isoleucine.

In this regard, the effect of valine is quite different. It inhibits growth at all concentrations tested in this experiment, 8 μM ¡ [Valine] ¡ 0.8 mM, and it represses gene expression of not only itself but also others, such as isoleucine. The repressive effect of valine can only

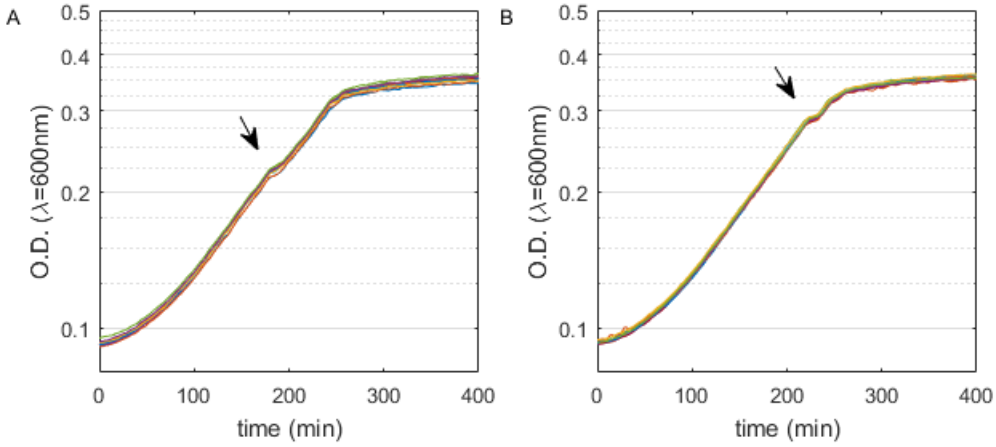

Figure 3.4: LE392 cultured in M9 supplemented with 0.4% glucose and casamino acids. In (A) the arginine concentration is the normal amount (80 μM) and in (B) the amount of arginine is doubled. The arrows indicate the location of the transition.

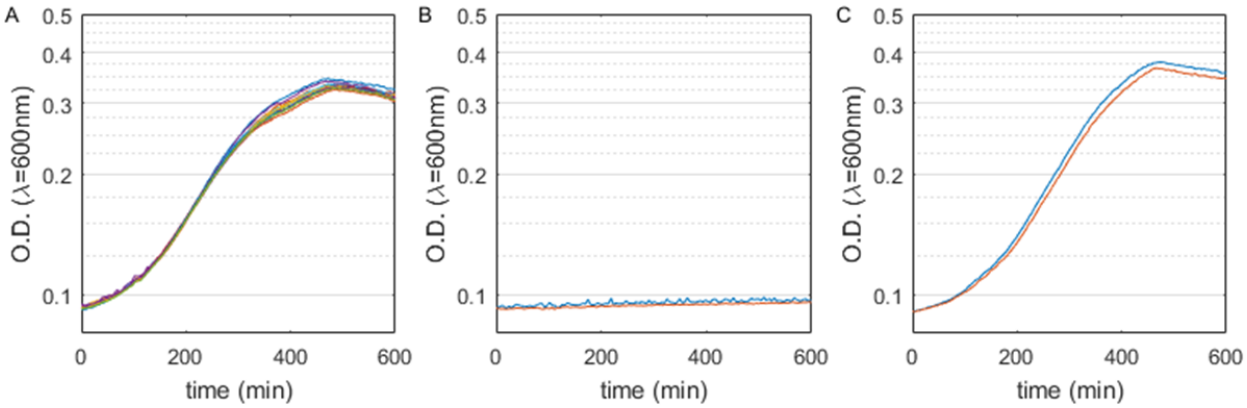

Figure 3.5: Strain MG1655 was grown in M9 supplemented with 0.2% glucose and no amino acid (A), in 0.2% glucose and 80 μM of valine (B), and 0.2% glucose with 80 μM valine and 80 μM isoleucine (C).

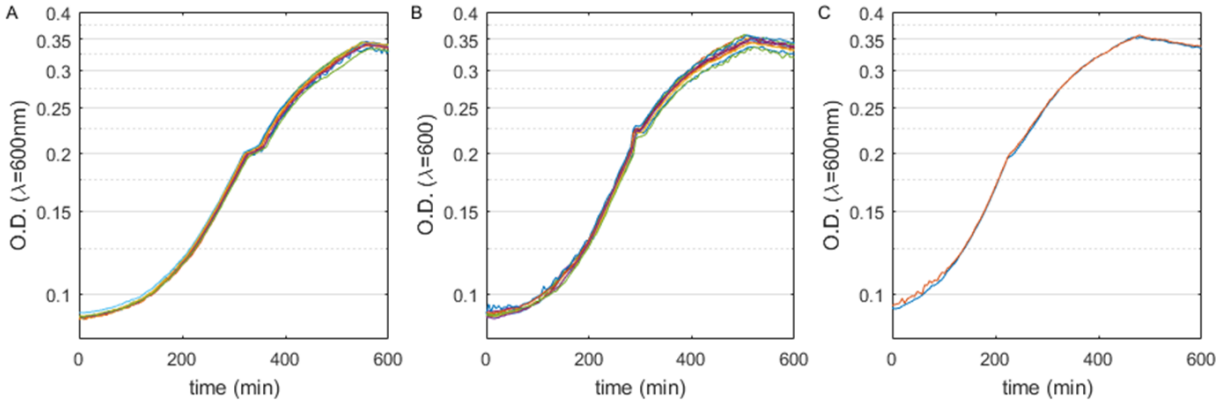

Figure 3.6: Strain MG1655 was grown in M9 supplemented with 0.2% glucose and 80 μM isoleucine (A), with 0.2% glucose and 40 μM methionine (B), in 0.2% glucose and 240 μM glycine (C).

be elevated when isoleucine is present in the medium [48]. Isoleucine that relieves valine inhibition can cause growth arrest similar to arginine, which is shown in Fig. 3.6(A). The effect is quite strong and lasts for 30 min. Isoleucine is one of the three branched amino acids. The other two being valine and leucine. Glutamate and α-ketoglutarate are the precursors for its synthesis. Methionine is the universal translation start code, but the first methionine is removed from most mature proteins [49]. This implies that without methionine, most protein synthesis cannot even get started in a cell, which perhaps is more serious than starvation of other amino acids. Methionine is also an essential methyl donor in a cell, after it has been converted to S-adenosylmethione (SAM) [50, 51]. Bacterium LE392 responded to methionine deprivation in a quite dramatic way as shown by the growth curve in Fig. 3.6(B). Here, instead of exhibiting a plateau when starvation occurs, OD increases sharply and forms a vertical step before leveling off. The arrest last about 15 min, which is again comparable to arginine. The sudden increase in OD is striking, implying a sudden burst of biomass or a significant change in cell's morphology, which gives rise to a higher scattering power. Finally, a small arrest is seen in the growth curve with glycine being the sole amino acid (see Fig. 3.6(C)). Glycine is the smallest of the 20 amino acids, and indeed is the

smallest possible with a single hydrogen as its side chain. It is also the only amino acid that is achiral. It can fit into hydrophilic or hydrophobic environments when a protein folds. Glycine is synthesized by a single step using L-serine as the starting molecule [52]. The kink in the growth curve, in this case, appeared different from that of arginine or methionine. The plateau region is narrower, and the growth rates prior and after the kink are quite different; it looks like a miniature version of the classical diauxic effect shown in Fig. 3.2.

In our current search, no anomaly was found in the growth curves of other 15 amino acids.

3.2 DISCUSSION

It is known that amino acid starvation causes a so-called stringent response, and the growth arrest seen in this experiment may be related to such a response. Below we briefly discuss the current knowledge of this fascinating phenomenon and its possible connection to our observations.

3.2.1 Stringent Response

When facing environmental stresses, such as osmotic shock, a pH change, amino acid depletion, and fatty acid limitation, a bacterium rapidly triggers a stringent response during which it transcriptionally down regulates growth promoting genes, such as rRNA and tRNA encoding genes, also known as stable RNAs [53, 54, 55], and up regulates stress resistance and starvation survival genes [56, 57]. An alarmone molecule, ppGpp, acts as an effector of the stringent response [58].

E. coli uses two pathways to produce ppGpp. Upon amino acid starvation, ribosome associate enzyme RelA produces ppGpp in responce to uncharged tRNA in the ribosome A-site, whereas SpoT is responsible for producing ppGpp due to stresses other than amino acid starvation. In addition, SpoT also serves as a hydrolase for ppGpp [59, 60, 61, 62], and thus plays a role of regulating the ppGpp level in a cell.

DksA works with ppGpp as a partner, which potentiates ppGpp's effect to inhibit or to activate gene expressions.[63, 64, 65, 56]

Every RNA polymerase (RNAP) holoenzyme contains one sigma factor, which enables the binding of RNAP to promoters, and initiates RNA synthesis. Different sigma factors are expressed or utilized under different conditions. In rapidly growing *E. coli* cells, σ^{70} is the factor for transcription of the "house-keeping" genes during rapid cell growth.

In an exponentially growing bacterial population, when ppGpp concentration is low, stable RNA promoters are more competitive than other promotors in recuiting RNAP with σ^{70} as the transcriptional factor. This machine-making-machine scheme ensures there is no shortage of "hardware" to maintain a maximal growth. We note that although only 1% of the whole genome is transcribed into rRNA and tRNA, these promotors sequester 60% RNA polymerases inside the cell [55]. During transcription, RNAP open complexes form on the stable RNA promoters and these complexes are intrinsically unstable; they are extremely sensitive to external perturbations [66, 67]. When a cell is short of an amino acid, ppGpp and Dsk bind to RNAP and make the open complexes unstable [68, 66]. RNAPs fall off from stable RNA promoters, and it increases the freely available RNAPs during starvation. These newly librated RNAPs are now, with the help of a variety of sigma factors, able to bind to other promotors to initiate a new set of gene expressions; amino acid biosynthesis is one among many classes of genes during the stringent response that help cells to survive [69, 70, 71].

3.2.2 Future Experiments

Different from the bacterial strains used in stringent response studies, my experiment used the wild type *E. coli* strain MG1655, which is also capable of synthesizing all amino acids. This leads to the resumption of growth after a brief growth arrest as seen in Fig. 3.2-3.4, and Fig. 3.6. To verify that the phenomenon I observed here is related to stringent response, an experiment could be carried out to assay ppGpp concentrations before, during and after the growth arrest. Isoleucine induced growth arrest can be studied for this purpose, since it lasts for $\sim 30\,\text{min}$. My expectation is that [ppGpp] increases at the beginning of the transition

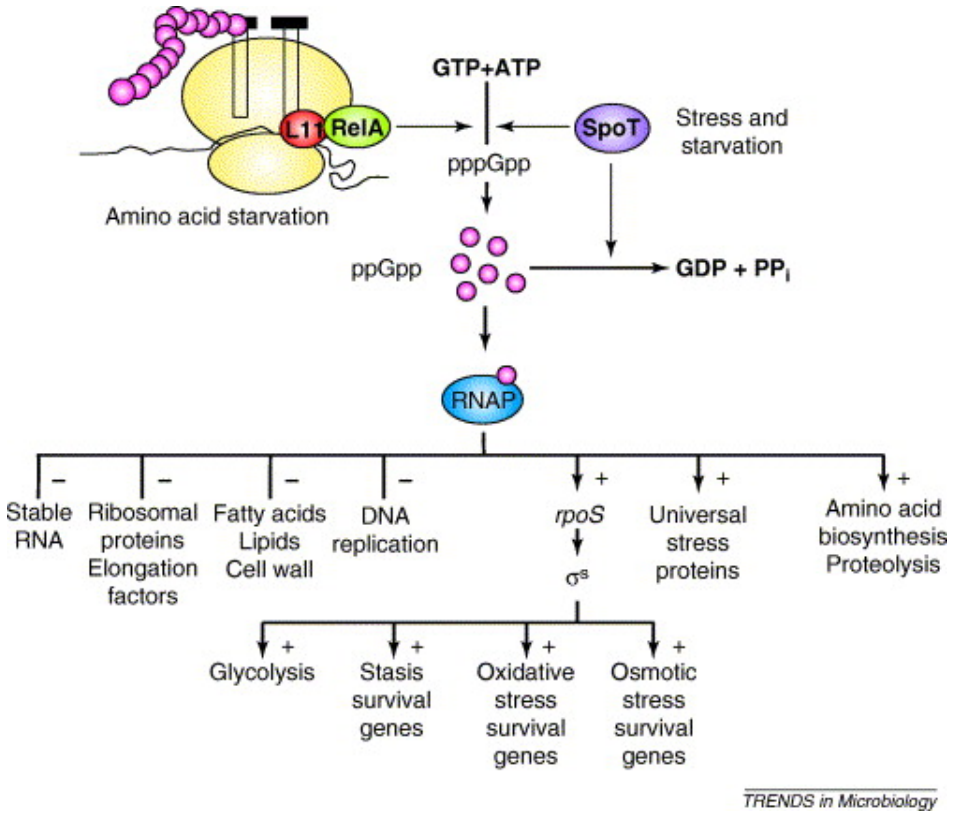

Figure 3.7: The Stringent Response. pppGpp is produced by RelA and SpoT two parellel pathways in response to starvation and stress, and is later converted into ppGpp. ppGpp binds to RNA polymerase (RNAP), and redirects transcription from growth-related genes to genes involved in starvation survival and stress resistance. Adapted from Magnusson, et al. [72]

in response to the amino acid depletion, resulting in RNAP redistribution and a period of very slow growth; at the end of the growth arrest, [ppGpp] decreases, RNAP will "refocus" on the promotors of stable RNAs, and growth resumes.

Further experiments could be conducted to study the RNAP distribution inside a cell during growth arrest. An *E. coli* MG1655 strain with fluorescent RNAP has been constructed by Cabrera et al [73]. If ppGpp is related with the growth arrest seen in my experiment, we might be able to visualize RNAP diffusion at the beginning of amino acid starvation and re-clustering around stable RNA loci after the cessation of the stringent response. This experiment can be conducted under a microscope in real-time when cells are kept at a constant temperature. It would be interesting to assay intracelluar concentrations of amino acids [74, 75] when a bacterium enters and exits from the stringent response.

A set of DNA microarray experiments could be conducted to measure gene transcription profiles around the transition point seen in our experiment. This would provide useful information about which genes are upregulated and which are down regualted in the process. In a previous study using *E. coli* cells, the stringent response was induced by a serine analogue, which could not be metabolized by the bacteria. It was shown that up to 110 genes get up or down regulated within the first 5 min of induction [55].

It would be interesting to examine bacterial division rate, cell length, and shape change before, during, and after the growth arrest in my experiment, to see how these factors contribute to a population-wide growth arrest [76, 77, 78]. This is especially the case for methionine starvation as shown in Fig. 3.6(B), where the growth curve increased very sharply before stepping into the arrest. Since our optical density measurement is non-specific, it would be very interesting to perform direct microscopic observation to see what kind of morphological change leads to the unexpected increase in O.D.. Is it due to a sudden change in cell sizes or due to a change in the optical properties of the cells?

Aside from valine only 4 out of 19 amino acids display growth arrests that are strong enough to be seen in our experiment. This is not consistent with the notion that every amino acid has a repressive effect on its own biosynthesis when present exogenously in a sufficient amount. For instance it is well known that exogenous serine inhibits the endogenous synthesis of both serine and glycine, whereas exogenous glycine fails to inhibit serine synthesis [52].

In our experiment while growth inhibition has been observed in glycine (see Fig. 3.6C), we never observed serine inhibition. Failure to identify more cases can be due to one of the following three reasons: (i) Our search in the concentration space is not thorough enough. The lowest concentration for each amino acid we used in the experiment is 1/10 of what was listed on the table for casamino acid. For an example, the lowest concentration of serine used is 8 μM. There is a good possibility that by restricting serine further, we may be able to see a growth arrest. (ii) A more interesting possibility is that the four amino acids, arginine, glycine, isoleucine, and methionine, are special and they cause a different response than other amino acids. The hallmark of growth arrest when these four amino acids are present in the medium is the sharpness by which the event takes place. This means that the exogenous signal is sensed and acted upon uniformly by all cells in the population. We don't know why this is the case, but if this were not the case, a rounded transition would result and would be much harder to identify in the growth curve. (iii) Cells respond slowly to the four amino acids that we have identified, i.e., the kinetics for all other amino acids is too fast to follow in our measurements. However, (iii) may be refuted on the bases that the response time we observed does not seem to correlate with the size and complexity of the regulatory networks. For instance, to make arginine requires eight enzymic steps but to make glycine, only one is required. But the response times for both are about the same.

Lastly, it would be interesting to know whether other amino acids are made from the supplied carbon or from the supplemented amino acids. In other words, to find out how does the cell make decision on when to make amino acids from an amino acid and when to make them from a carbon source. A carefully designed experiment using the plate reader should allow us to address some of these questions.

According to my expierence, experiments involved with cell shape and size monitoring are feasible under our experimental conditions, provided the samples are stably fixed on the stage without drifting. The fluorescent RNAP diffusion and re-clustering experiment can be easily finished since I already obtained the strain from D. J. Jin [79]. The microarray experiment is expensive and requires some experience since we've never analyzed microarray data before. The search for growth arrests in all amino acids can be an open ended problem. There's no guarantee about what one would find. Maybe there are some interesting and

unknown phenomena still to be found. The last question about whether amino acid is synthesized from carbon source or other amino acids could be a big good question. To tackle this problem, more knowledge on the carbon and nitrogen metabolism networks is required.

3.3 CONCLUSION

A major but unexplained finding of this experiment is the uniformity by which a bacterial population responded to the stress induced by amino acid starvation. The sharpness of the transitions is in stark contrast with many other known biological responses that are typically uncoordinated among different cells and hence sluggish at a population level. Moreover, despite the signal being small and short lived, which surely could not be detected by the conventional OD measurement, the 96-well plate reader gives reliable measurements that are consistent between duplicated samples and for different runs. The transient arrests seen in the growth curves when arginine, glycine, isoleucine, and methionine are individually present in the extracellular medium, are consistent with the biophysical picture that the amino acid biosynthesis networks are end-product inhibited. The interesting but puzzling question is why the effect is seen for these four amino acids, not the others. As pointed out, more work is needed and in the Discussion, some future works are proposed. Clearly, searches should be extended to lower amino acid concentrations than currently surveyed, and the measurement can be improved by better temperature control and aeration in the plate reader. These will reduce well-to-well variations and allows signals from different wells to be better averaged. We believe that by averaging the OD data from different wells, the sensitivity in detecting small anomalies can be significantly increased.

Metabolic networks are among the most complicated networks in biological cells. These networks are evolutionarily linked in different organisms, but there are significant variations from organism to organism. Even for the best studied *E. coli* K12 strain, not all issues concerning carbon utility and amino acid biosynthesis are understood; not to mention that the vast majority of microorganisms have never been studied. Therefore, a simple and robust method to peek into the inner working of their metabolisms could be very significant.

The method described here, with perhaps some improvements, can provide such a robust tool. At an elementary level, the technique will yield important time constants, such as the activation and termination of the starvation for different amino acids and their threshold values. There are important but unsolved questions concerning how amino acid starvation is connected to a larger, global response to stress in bacteria, known as the stringent response. The method described here can contribute to such study. At a more advance level, one can use the technique to study interactions between different pathways in a metabolic network by depleting some key intermediates in the pathways and measure how a cell responds. In other words, it may be used to diagnose how a network is wired. There are many important questions in system biology, and understanding how metabolic networks work is one of them. The big questions include (i) how a cell partitions its resource, such as carbon, oxygen, and nitrogen for instance, in a given environment; (ii) how metabolic networks deal with different stresses; (iii) is there a logic behind such regulation; and (iv) what are the universal features of metabolic networks among different bacteria? These are questions that we hope to address in future experiments.

3.4 MATERIAL AND METHODS

Bacteria Strains: *E. coli* MG1655 and JH1

Culture Media: M9 minimal medium (m/v %): 0.7% Na_2HPO_4, 0.03% KH_2PO_4, 0.05% NaCl, 0.1% NH_4Cl, 10^{-3}M $MgSO_4$ and 10^{-4}M $CaCl_2$. 0.4% glucose was used as carbon source unless otherwise indicated. 0.1% Casamino acid was added except the experiments in Fig. 3.5 and 3.6, where specific amino acid was used as indicated.

Procedures: Bacteria were firstly grown in the specified M9 medium overnight to get adapted to the culturing condiiton. The saturated overnight culture was then diluted 100-fold in fresh media, and started a mid-log growth to reach O.D. $= 0.4$ ($\lambda = 600\,nm$). Cells were centrifuged down, washed, and resuspended in fresh media. Concentration was adjusted to O.D. $= 0.01 - 0.03$ ($\lambda = 600\,nm$). Aliquots ($100\,\mu$m each) were pipetted into a 96-well microplate, which was kept at 37°C in a microplate reader (Tecan, infinite M200)

Table 3.1: Casamino Acids Composition

Lysine	Arginine	Isoleucine	Tyrosine	Alanine	Methionine
3.7%	1.4%	2.7%	3.1%	2.4%	1.7%
Histidine	Proline	Glycine	Glutamine	Serine	Leucine
0.7%	4.1%	1.0%	14.2%	9.0%	3.5%
Valine	Phenylalanine	Threonine	Cystine	Aspartic Acid	Unkown
4.1%	0.7%	2.5%	0.3%	3.7%	41.2%

with continuous shaking. Optical density of each well was measured and recorded every 290 s. For one specific medium composition, usually 12-24 replicates (wells) were used.

4.0 ACROBATIC MOVEMENTS OF MARINE BACTERIUM *VIBRIO AGLINOLYTICUS* UPON FLAGELLAR MOTOR REVERSAL

4.1 INTRODUCTION

When a small animal, such as a cat, is tossed up in the air, it will most likely land with its feet on the ground despite the fact that the cat possesses zero angular momentum initially. A cat is capable of reorienting itself by twisting and bending its body parts to generate rotation. This ability of manipulating body's internal degrees of freedom has been exploited to create stunning movements in ballet dancing, acrobatic performance, and competitive diving. In this chapter, I show that marine bacterium *Vibrio alginolyticus* also exploits the flexibility of its basal body to maneuver in a viscous fluid and to randomize swimming directions with high efficiency.

V. alginolyticus is morphologically a simple cell, consisting of an elliptical cell body and a single left-handed polar flagellum. Viewed from the flagellar tail toward the cell body, the flagellum can rotate in clockwise (CW) or counter clockwise (CCW) direction. The cell swims forward when the flagellum rotates in the CCW direction and backwards when the motor rotates in the CW direction. Despite the motor size being small, diam $\simeq$50 nm, it is remarkably powerful, capable of turning at 1700 r.p.s and pushing the cell body at a speed of $\sim 150\,\mu\mathrm{m}/s$ [80]. Based on these values, the thrust force and torque are calculated to be $F = 0.73\ pN$ and $N = 0.16\ pN \cdot \mu m$ [81]. Despite high motility, *V. alginolyticus* swims at low-Reynolds numbers, $Re \simeq 10^{-4}$. This has important consequences for bacterial chemotaxis because it implies that if the flagellar motor possesses only one degree of freedom, i.e. it rotates either in CCW or CW direction, the bacterial tracks are symmetric under time reversal. The only way the swimmer can alter the swimming direction is by brownian motion.

It typically takes $\tau_R \, (\equiv 4\pi\eta a^3/k_B T) \sim 3\,\mathrm{s}$ given the typical cell size ($a \simeq 1\,\mu\mathrm{m}$) and viscosity ($\eta \simeq 0.01\,\mathrm{cP}$). In strongly fluctuating environments, where hydrodynamic convection is significant, such as in oceans, this long idling time is unproductive and prevents the bacterium from exploring space, limiting its nutrient uptake. Our group found that marine bacterium *V. alginolyticus* is able to break this impasse by incorporating a novel movement in its motility pattern [18]. Specifically, whenever the bacterial flagellar motor switches from CW to CCW rotation, or from backward to forward swimming, the flagellum flicks and deflects the cell body to a random direction. The motility pattern of a marine bacterium thus consists of distinctive features, i.e., a forward (CCW) run is followed by a reversal (CW), and the new run is typically in a direction ∼90 degrees with respect to that of the previous runs. A typical trajectory of wild-type (wt) *V. alginolyticus* is depicted in Fig. 4.1(A), showing the cyclic 3-step (run-reverse-flick) motility pattern. The flick angle definition is given in Fig. 4.1(B).

In Xie et al.'s work in 2011 [18], it was noticed that a cell's ability to flick is correlated with its swimming speed. For instance, in de-energized cells, either by reducing Na^+ ions in a motility medium or by oxygen depletion, the bacteria abolished the flicking step. Likewise, increasing the viscosity of the medium had the same effect. However, the physical mechanism that caused the bacterial flagellum to flick was not known until Son et al. took an interest in the problem and studied the phenomenon systematically using fast-speed video imaging microscopy [19]. They found that the flick does not occur at the same time the motor reverses from CW to CCW rotation but is delayed by $\sim 10\,\mathrm{ms}$. Such a delay was explained by the investigators as the elastic relaxation of the hook that undergoes the transition from a taut to a relaxed form and becomes taut again as the motor reverses. Since the elastic modulus of the hook is not linear, assuming its smallest value when it is relaxes, a kink or buckle can develop under the combined actions of twist and compression. The end result is that the cell body is being pushed at an angle relative to the cell-body axis, steering the cell body into a new random direction. Interestingly, this off-axis movement (or a flick) is very brief, lasting for 50-60 ms before the flagellum realigns with the cell-body axis and normal swimming resumes. It was proposed that the realignment is a result of stiffening of the hook when it is overwound.

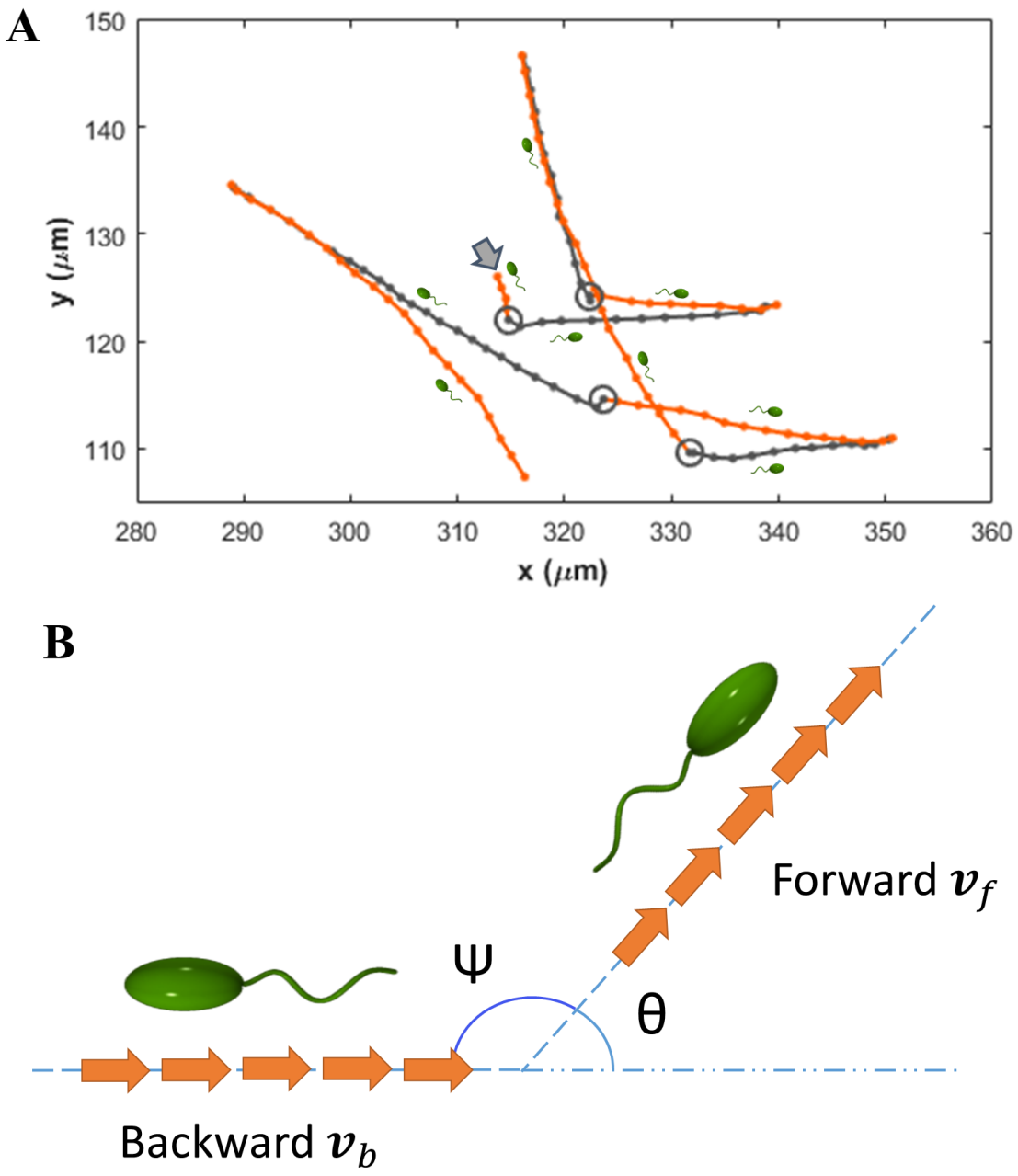

Figure 4.1: A Typical Wild Type *V. alginolyticus* (YM4) Trajectory (A). The black segments indicate forward swimming (CCW) intervals, and orange segments are backward (CW) swimming intervals. An arrow is placed at trajectory starting point. Circles indicate backward-to-forward transitions where flicks take place. The definition of flick angle is given in plot (B), where the orange arrows indicate bacterial swimming directions. The angle between the forward (CCW) and the backward (CW) directions is defined as the flick angle θ, and its complementary angle Ψ is the cell-body reorientation angle.

In this chapter, I report new experimental observations of bacterial directional randomization by flicking, and theoretical analyses of a simple model that mimicks bending and twisting of the flagellum about its base. My analysis suggests that there is a partitioning of motor power to flagellar rotation, which produces thrust, and to bending and twisting, which causes the directional change.

4.2 EXPERIMENTAL OBSERVATIONS

In Fig. 4.2, I show that wild type *Vibrio alginolyticus* has a higher probability to flick in large angles as the cell length $2a$ increases. Specifically, it shows that the flick angle θ shifts towards 180° as the cell size increases with the mean flick angles shifting from 76° to 136°, which are indicated by the vertical orange lines. According to the definition of θ in Fig. 4.1(B), a large flick angle corresponds to a small change in the swimming directions between two consecutive runs, or in other words, large cells are less likely to change swimming directions than their small counterparts. A similar result was also observed by Son et al. [19].

The most interesting phenomenon observed here is that small YM4 cells, with the major-axis $2a < 2.9\,\mu$m, are more likely to flick at $\theta \simeq 30°$ instead of at 90° as reported in Xie's and Son's papers [19, 18] (see Fig. 4.2(A)). This is further illustrated in Fig. 4.3(A), where bacteria shorter than $2.4\,\mu$m have a mean flick angle around 49^o and are most probable to flick at 10°, suggesting that when swimming at high speed, small bacteria tend not to change direction upon motor reversal from CW to CCW direction or from backward to forward swimming. That is the new forward swimming is a continuation of the previous backward swimming. A typical YM4 trajectory with near-0° flick angles is shown in Fig. 4.3(B).

More details are revealed when cases of near-0° flicks are examined under fluorescence microscope. Fig. 4.4 gives one example where bacteria are stained with Nano Orange (Invitrogen) [82]. Consecutive images show that the bacterium flipped its head and tail directions during a flick, and the flagellum kept straight with the cell body at the onset and

at the end of the process.

We also noticed that during the flick the cell body moved side-wise by about $1\,\mu$m, i.e. the width of the cell. Off-hand, it is not clear how a bacterium does such a maneuver.

4.3 A SIMPLE MODEL

4.3.1 Cell-Body Reorientation Theory

Dr. Henry Fu from University of Nevada considered this flick process from a physics point of view (personal communications). He tried to calculate the cell-body reorientation angle, when the path for flagellar off-axis rotation is defined. To simplify the calculation, he assumes that the bacterial cell body is spherical, and the flagellum extends out from the cell center. One can set up a bacterial body-fixed coordinate system, in which bacterial head is always pointing in the negative z direction (see the inset of Fig. 4.5). During forward and backward swimming intervals, the flagellum is coaxial with the cell-body axis, which we specified as $\theta(0) = 0$ and $\phi(0) = 0$, where θ and ϕ are the polar and the azimuthal angles of the flagellum in the body-fixed frame. A flick can be described as the process in which the flagellum rotates about its base, following some specific trajectory $\theta(t)$ and $\phi(t)$, and then after a time T returns to its original position $\theta(T) = 0$ and $\phi(T) = 0$.

For simplicity, it is further assumed that the flagellum is represented by a rigid straight rod of length L, and radius r_0. A point on the flagellum is then given by,

$$\mathbf{r}(t) = s\hat{\mathbf{t}},$$

where s is the distance of that point from the origin, $\hat{\mathbf{t}}$ is a radial unit vector along the flagellum. The unit vectors specify the incremental direction of θ and ϕ are given by $\hat{\mathbf{n}}$, and $\hat{\mathbf{b}}$ (see the inset in Fig. 4.5). For a later convenience, it is also useful to write the

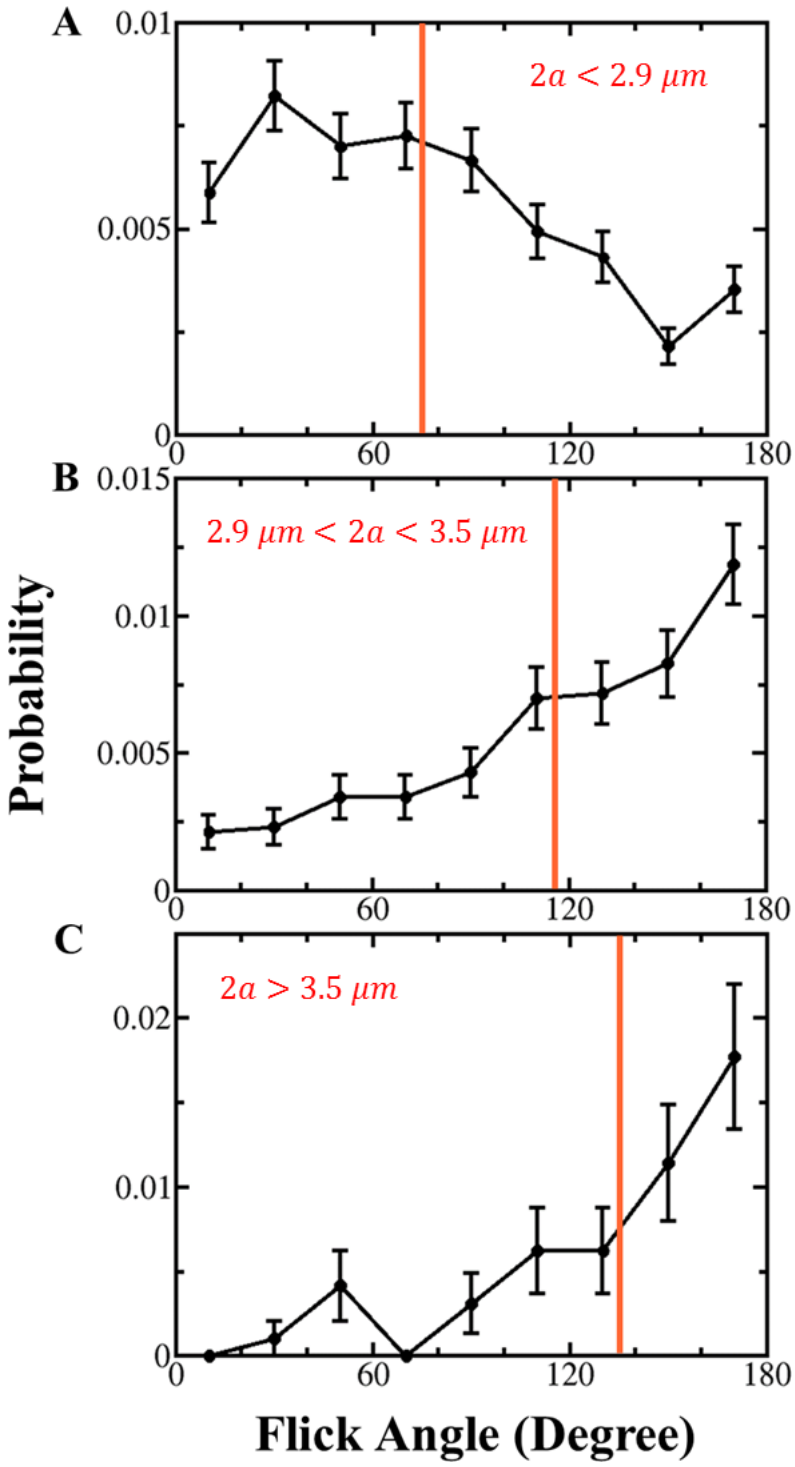

Figure 4.2: YM4 Flick Angle Probability Density Functions (PDF). All bacteria selected here have a speed larger than 50 μm/s. Plot A-C are flick angle PDFs for bacteria with length (0, 2.9) μm, (2.9, 3.5) μm, and (3.5, 6) μm. Each curve includes 578, 278, and 48 flick events respectively. Orange lines indicate the mean flick angles under each condition.

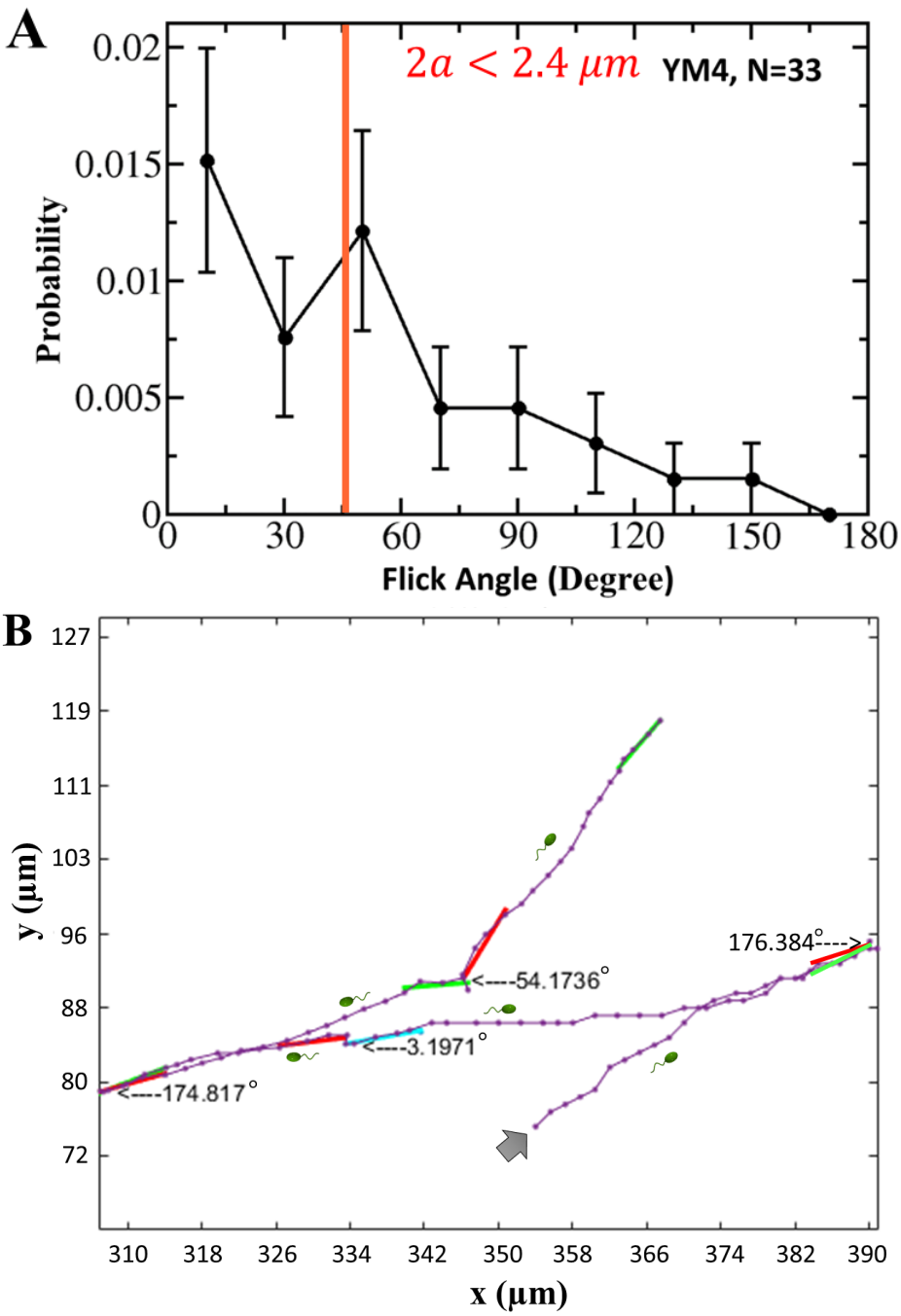

Figure 4.3: Small Bacteria Are Most Likely to Flick with Small Flicking Angles. Plot (A) shows the flick angle probability density function (PDF), where the flick angles are collected from YM4 with the major cell-body axis $2a < 2.4\,\mu$m and speed $v > 50\,\mu$m/s. Plot (B) shows a typical small bacterial trajectory with a near-0° flick. The cell size is $2.61\,\mu$m. The trajectory starting point is marked with a gray arrow. The green (cyan) and red lines are linear fittings of 5 positions before and after transitions.

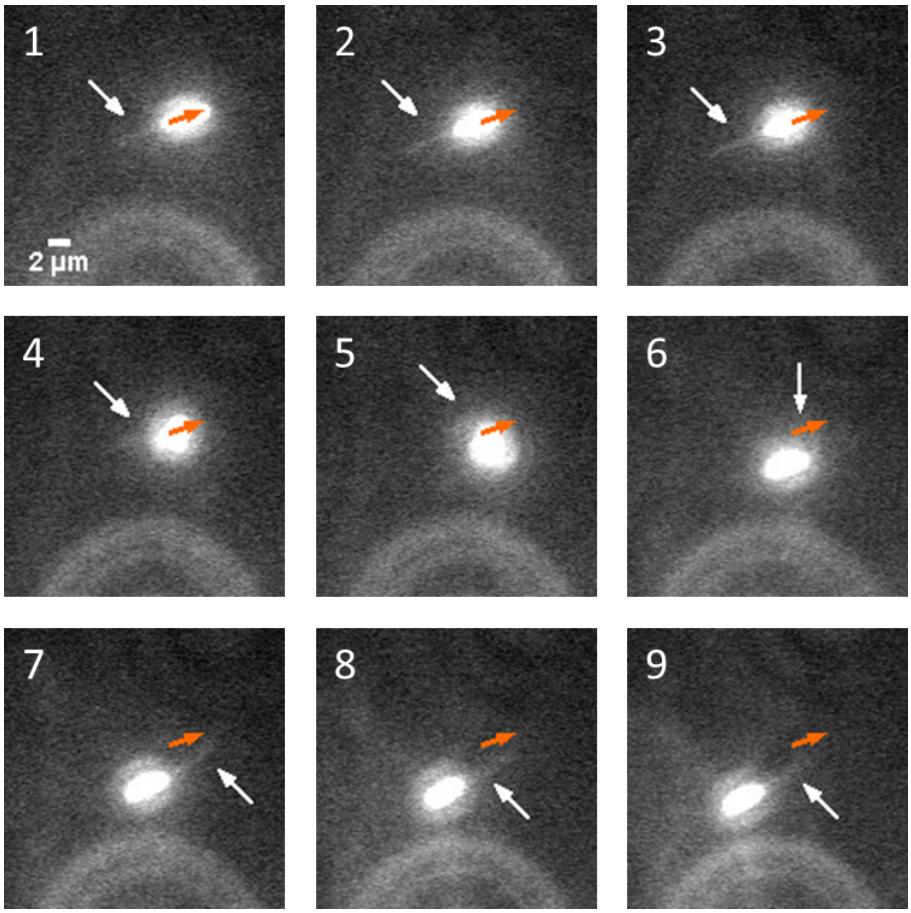

Figure 4.4: Fluorescence Imaging of a Near-0^o Flick. These are consecutive video images with time interval 28 ms. The orange arrow serves as a reference, which stays at the same position in every frame. White arrows indicate where the flagellum is located in each frame. The bacterium swam backward from frame 1 to frame 3, and starts the flick process in frame 4, which continues to frame 6. Afterwards, frame 7 and on-wards, the bacterium swims in the forward direction. During this processes, the cell body flipped its head and tail, namely reoriented by 180^o. The flagellum started and ended in a straight configuration with respect to the cell body axis, although its position relative to the cell body was unclear during the flick, i.e., frame 4 to 6.

transformation matrix $\overleftrightarrow{R}$ between the spherical and the Cartesian coordinate systems,

$$\begin{pmatrix} \hat{\mathbf{t}} \\ \hat{\mathbf{b}} \\ \hat{\mathbf{n}} \end{pmatrix} = \overleftrightarrow{R} \begin{pmatrix} \hat{\mathbf{x}} \\ \hat{\mathbf{y}} \\ \hat{\mathbf{z}} \end{pmatrix} = \begin{pmatrix} \sin\theta\cos\phi & \sin\theta\sin\phi & \cos\theta \\ -\sin\phi & \cos\phi & 0 \\ \cos\theta\cos\phi & \cos\theta\sin\phi & -\sin\theta \end{pmatrix} \begin{pmatrix} \hat{\mathbf{x}} \\ \hat{\mathbf{y}} \\ \hat{\mathbf{z}} \end{pmatrix}, \tag{4.1}$$

and its inverse $\overleftrightarrow{R}^{-1}$,

$$\begin{pmatrix} \hat{\mathbf{x}} \\ \hat{\mathbf{y}} \\ \hat{\mathbf{z}} \end{pmatrix} = \overleftrightarrow{R}^{-1} \begin{pmatrix} \hat{\mathbf{t}} \\ \hat{\mathbf{b}} \\ \hat{\mathbf{n}} \end{pmatrix} = \begin{pmatrix} \sin\theta\cos\theta & -\sin\phi & \cos\theta\cos\phi \\ \sin\theta\sin\phi & \cos\phi & \cos\theta\sin\phi \\ \cos\theta & 0 & -\sin\theta \end{pmatrix} \begin{pmatrix} \hat{\mathbf{t}} \\ \hat{\mathbf{b}} \\ \hat{\mathbf{n}} \end{pmatrix}. \tag{4.2}$$

Supposing in the laboratory frame, the bacterial body has a translational velocity $\mathbf{V}$ and a rotational velocity $\mathbf{\Omega}$, the velocity of a point on the flagellum in the laboratory frame obeys the velocity addition rule,

$$\dot{\mathbf{r}}(s) = \mathbf{V} + \mathbf{\Omega} \times \mathbf{r} + s\dot{\theta}\partial_\theta\hat{\mathbf{t}} + s\dot{\phi}\sin\theta\partial_\phi\hat{\mathbf{t}} = \mathbf{V} + \mathbf{\Omega} \times \mathbf{r} + s\dot{\theta}\hat{\mathbf{n}} + s\dot{\phi}\sin\theta\hat{\mathbf{b}}. \tag{4.3}$$

Its tangential and perpendicular components are given respectively by,

$$\dot{\mathbf{r}}_\parallel = \hat{\mathbf{t}}\hat{\mathbf{t}} \cdot \mathbf{V},$$

$$\dot{\mathbf{r}}_\perp = (I - \hat{\mathbf{t}}\hat{\mathbf{t}}) \cdot \mathbf{V} + s\mathbf{\Omega} \times \hat{\mathbf{t}} + s\dot{\theta}\hat{\mathbf{n}} + s\dot{\phi}\sin\theta\hat{\mathbf{b}}.$$

According to the resistive force theory [83, 84], as the flagellum undulates, the forces corresponding to the normal and tangential motion would be approximately given by the local flagellum velocity times the drag coefficient.

$$\begin{aligned} \mathbf{f} &= \zeta_\parallel\dot{\mathbf{r}} + \zeta_\perp\dot{\mathbf{r}}_\perp \\ &= [\zeta_\parallel\hat{\mathbf{t}}\hat{\mathbf{t}} + \zeta_\perp(\mathbf{I} - \hat{\mathbf{t}}\hat{\mathbf{t}})] \cdot \mathbf{V} + \mathbf{s}\zeta_\perp\left(\mathbf{\Omega} \times \hat{\mathbf{t}} + \dot{\theta}\hat{\mathbf{n}} + \sin\theta\dot{\phi}\hat{\mathbf{b}}\right) \qquad (4.4) \\ \boldsymbol{\tau} &= \mathbf{r} \times \mathbf{f} \\ &= s\zeta_\perp\hat{\mathbf{t}} \times \mathbf{V} + \mathbf{s^2}\zeta_\perp[\hat{\mathbf{t}} \times \left(\mathbf{\Omega} \times \hat{\mathbf{t}}\right) + \dot{\theta}\hat{\mathbf{b}} - \sin\theta\dot{\phi}\hat{\mathbf{n}}]. \qquad (4.5) \end{aligned}$$

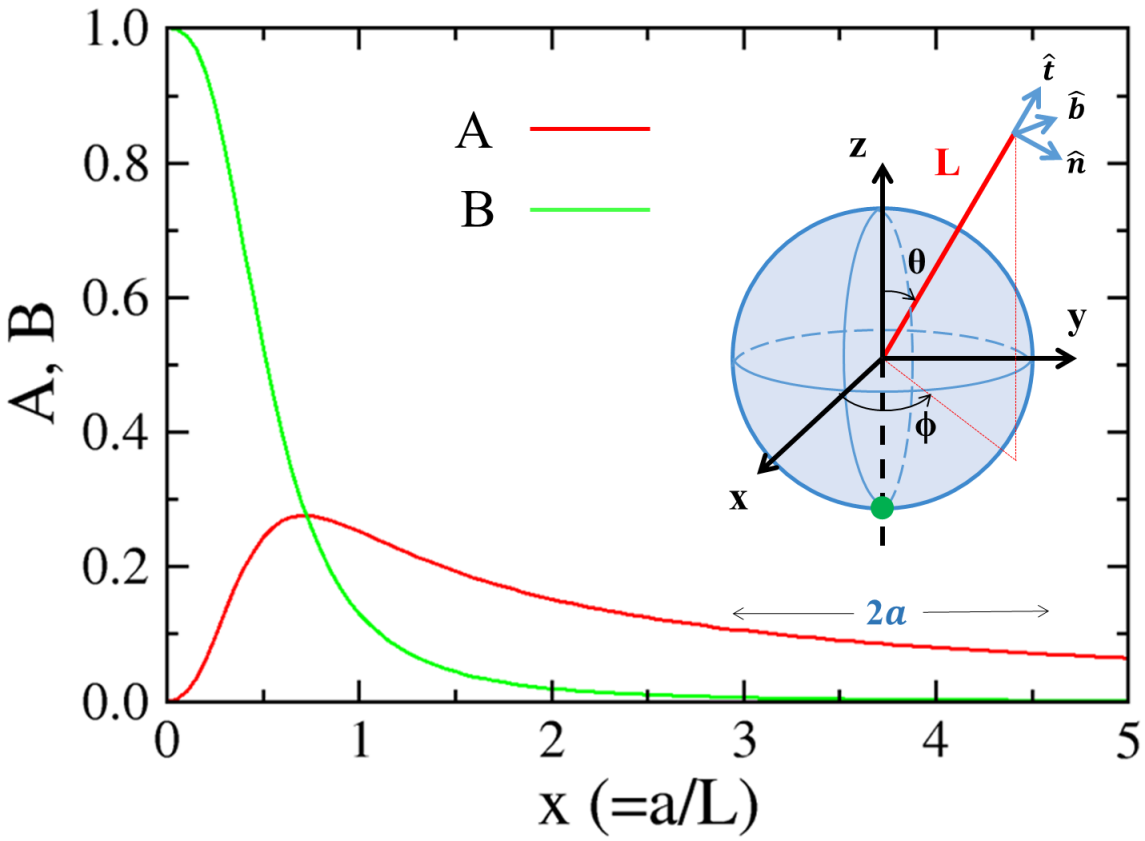

Figure 4.5: A and B Coefficients for Translational and Rotational Motion of the Cell Body. For *V. alginolyticus*, $x \simeq 0.2$ if I calculated it according to an equivalent sphere for the translational motion. This gives $B \simeq 0.92$. The insert is a diagram of body-fixed coordinate system, where the bacterial head is pointing in the negative z-axis direction (the green dot). The deviation of flagellum from the z direction at time t is depicted by the polar angle $\theta(t)$ and azimuthal angle $\phi(t)$ in the body-fixed spherical coordinate system.

where $\zeta_\parallel$ and $\zeta_\perp$ are drag coefficients of the rod in the tangential and normal directions. To make a better approximation, I'll use the resistive coefficients of a helical flagellum instead.

$$\zeta_\perp = 2\zeta_\parallel = \frac{4\pi\mu}{\ln(2\lambda/r_0) - 1/2}$$

where r_0 and pitch λ are radius and pitch of the helical flagellum [84], and μ is the viscosity. The torque $\boldsymbol{\tau}$ is calculated about the cell-body center. Integrating the force and torque density in Eq. (4.4) over the length L, we get the total force and torque acting on the flagellum:

$$\begin{aligned} \mathbf{F}_f &= L[\zeta_\parallel \hat{\mathbf{t}}\hat{\mathbf{t}} + \zeta_\perp(\mathbf{I} - \hat{\mathbf{t}}\hat{\mathbf{t}})] \cdot \mathbf{V} + \tfrac{\mathbf{L^2}}{\mathbf{2}}\zeta_\perp \left(\boldsymbol{\Omega} \times \hat{\mathbf{t}} + \dot{\theta}\hat{\mathbf{n}} + \sin\theta\dot{\phi}\hat{\mathbf{b}}\right), \\ \mathbf{N}_f &= \tfrac{L^2\zeta_\perp}{2}\hat{\mathbf{t}} \times \mathbf{V} + \tfrac{\mathbf{L^3}\zeta_\perp}{\mathbf{3}}\left[\hat{\mathbf{t}} \times \left(\boldsymbol{\Omega} \times \hat{\mathbf{t}}\right) + \dot{\theta}\hat{\mathbf{b}} - \sin\theta\dot{\phi}\hat{\mathbf{n}}\right]. \end{aligned} \tag{4.6}$$

One can also calculate the force and the torque on the cell body, which according to the Stokes' law are given by,

$$\mathbf{F}_b = Z\mathbf{V},$$

$$\mathbf{N}_b = M\boldsymbol{\Omega},$$

where $Z = 6\pi\mu a$ and $M = 8\pi\mu a^3$ being the translational and rotational drag coefficients of a spherical cell body with a radius a. For free-body swimming, there is no net force or torque acting on the bacterium and hence,

$$\mathbf{F} = \mathbf{F}_f + \mathbf{F}_b = 0,$$

$$\mathbf{N} \;=\; \mathbf{N}_f + \mathbf{N}_b = 0.$$

Substituting Eq. (4.6) in the above two equations and resolving them along the $\hat{\mathbf{t}}$, $\hat{\mathbf{n}}$, and $\hat{\mathbf{b}}$ directions in the body-fixed frame, I find

$$\begin{cases} \zeta_{\parallel} L V_t + Z V_t = 0 \\ \zeta_{\perp} L V_n + \frac{1}{2}\zeta_{\perp} L^2 \left(\Omega_b + \dot{\theta}\right) + Z V_n = 0 \\ \zeta_{\perp} L V_b + \frac{1}{2}\zeta_{\perp} L^2 \left(-\Omega_n + \dot{\phi}\sin\theta\right) + Z V_b = 0 \end{cases},$$

$$\begin{cases} M\Omega_t = 0 \\ -\frac{1}{2}\zeta_{\perp} L^2 V_b + \frac{1}{3}\zeta_{\perp} L^3 \left(\Omega_n - \dot{\phi}\sin\theta\right) + M\Omega_n = 0 \\ \frac{1}{2}\zeta_{\perp} L^2 V_n + \frac{1}{3}\zeta_{\perp} L^3 \left(\Omega_b + \dot{\theta}\right) + M\Omega_b = 0 \end{cases}.$$

The above complicated results can be organized in a compact form using the matrix representation,

$$\begin{pmatrix} V_t \\ V_b \\ V_n \end{pmatrix} = -AL \begin{pmatrix} 0 \\ \dot{\phi}\sin\theta \\ \dot{\theta} \end{pmatrix},$$

$$\begin{pmatrix} \Omega_t \\ \Omega_b \\ \Omega_n \end{pmatrix} = B \begin{pmatrix} 0 \\ -\dot{\theta} \\ \dot{\phi}\sin\theta \end{pmatrix}, \tag{4.7}$$

where A and B are constants given by,

$$A = \frac{\frac{6M}{L^2(L\zeta_{\perp}+4Z)}}{1+\frac{12M(L\zeta_{\perp}+Z)}{L^3\zeta_{\perp}(L\zeta_{\perp}+4Z)}}, \tag{4.8}$$

$$B = \frac{1}{1+\frac{12M(L\zeta_{\perp}+Z)}{L^3\zeta_{\perp}(L\zeta_{\perp}+4Z)}}. \tag{4.9}$$

By defining the reduced drag coefficient as $\zeta'_{\perp} = \frac{\zeta_{\perp}}{\pi\mu} = \frac{4}{\ln(2\lambda/r_0)-1/2}$, the A and B coefficients can be expressed by the single parameter $\zeta'_{\perp}$,

$$A = \frac{\frac{48x^3}{24x+\zeta'_{\perp}}}{1+\frac{96x^3(6x+\zeta'_{\perp})}{\zeta'_{\perp}(24x+\zeta'_{\perp})}},\ B = \frac{1}{1+\frac{96x^3(6x+\zeta'_{\perp})}{\zeta'_{\perp}(24x+\zeta'_{\perp})}}, \tag{4.10}$$

where $x = a/L$. For *V. alginolyticus* YM4, our previous experiment [81] found $\lambda \simeq 1.2\,\mu$m and $r_0 \simeq 0.016\,\mu$m, giving $\zeta'_{\perp} \simeq 0.89$.

To gain some intuition about A and B, since they determine the response of the cell-body to a change in the flagellar angular positions, we plot these two coefficients against $x(\equiv a/L)$ in Fig. 4.5. The figure shows that while B is a monotonically decreasing function of x, with $B \simeq 1$ for a very long ($x \ll 1$) flagellum and $B \to 0$ for a very short ($x \gg 1$) flagellum, A is peaked at $a/L \simeq 0.6$. We noticed that the above result is independent of fluid viscosity μ, indicating that the phenomenon is purely geometrical [85]. Eq. (4.11) and (4.12) show that $\mathbf{V}$ and $\mathbf{\Omega}$ are completely specified by angular speed of the flagellum, $\dot{\theta}(t)$ and $\dot{\phi}(t)$, in the body-fixed frame. Canceling out the time derivatives on both sides of equations (4.11) and (4.12), I found that the translational and rotational displacements of the cell body are uniquely specified by a path integral in the (θ,ϕ) space and are independent of their rate of change.

While the relationship between (V, Ω) and ($\dot{\theta}$, $\dot{\phi}$) is very concise using the polar coordinates, the relation is not easy to use when one would like to follow the motion of the cell body in the laboratory frame. In light of this, we write the translational V and rotational Ω velocities in the body-fixed Cartesian coordinates,

$$\begin{pmatrix} V_x \\ V_y \\ V_z \end{pmatrix} = R^{-1} \begin{pmatrix} V_t \\ V_b \\ V_n \end{pmatrix} = -AL \begin{pmatrix} -\sin\phi & \cos\theta\cos\phi \\ \cos\phi & \cos\theta\sin\phi \\ 0 & -\sin\theta \end{pmatrix} \begin{pmatrix} \dot{\phi}\sin\theta \\ \dot{\theta} \end{pmatrix}, \tag{4.11}$$

$$\begin{pmatrix} \Omega_x \\ \Omega_y \\ \Omega_z \end{pmatrix} = R^{-1} \begin{pmatrix} \Omega_t \\ \Omega_b \\ \Omega_n \end{pmatrix} = B \begin{pmatrix} -\sin\phi & \cos\theta\cos\phi \\ \cos\phi & \cos\theta\sin\phi \\ 0 & -\sin\theta \end{pmatrix} \begin{pmatrix} -\dot{\theta} \\ \dot{\phi}\sin\theta \end{pmatrix}. \tag{4.12}$$

This will later be mapped to the laboratory frame. The marine bacterium *V. alginolyticus* swims by a cyclic 3-step, forward-reverse-flick, motility pattern. In the body-fixed frame, therefore, the flagellum has to recover its starting position after a flick, or in other words the path traced out by the flagellum is closed in the body-fixed frame as delineated in the insert of Fig. 4.5. However, this is not true in the laboratory frame (see Fig. 4.6).

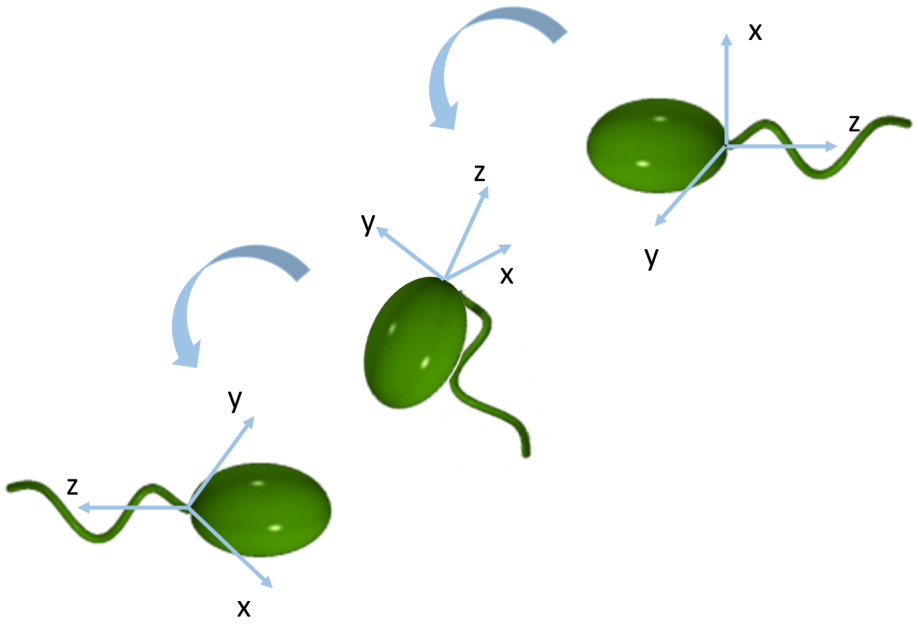

Figure 4.6: Cell Body-Fixed Frame Observed in Laboratory Frame.

4.3.2 Cell-Body Reorientation Angle and Displacement

4.3.2.1 Rotation Matrix Rotation about a fixed axis is often encountered in physics, and in particular when a rotation is about a particular axis, such as about the $\hat{z}$ axis by an angle ψ, the rotation matrix is simple and has the well-known form,

$$R_{\hat{z}}(\psi) = \begin{bmatrix} \cos\psi & -\sin\psi & 0 \\ \sin\psi & \cos\psi & 0 \\ 0 & 0 & 1 \end{bmatrix}. \tag{4.13}$$

Rotation about an arbitrary axis $\hat{u}$ by a finite angle ψ in three dimensional space is less well known but can be derived from an infinitesimal rotation $d\psi$ with the result $d\vec{r} = d\psi\hat{u}\times\vec{r}$ or in the matrix form $d\vec{r} = d\psi G_{\hat{u}}\cdot\vec{r}$, where $\vec{r}$ is the position vector and $G_{\hat{u}}$ is the rotation generator given by,

$$G_{\hat{\mathbf{u}}} = \begin{bmatrix} 0 & -u_z & u_y \\ u_z & 0 & -u_x \\ -u_y & u_x & 0 \end{bmatrix}. \tag{4.14}$$

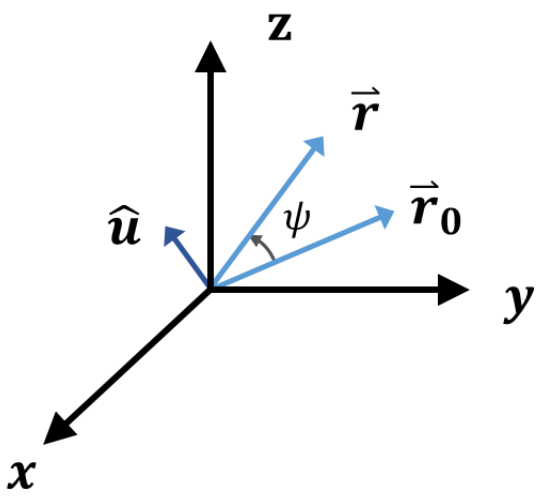

Figure 4.7: Rotation of a Position Vector $\vec{r}_0$. A position vector $\vec{r}_0$ is rotated about the fixed axis $\hat{u}$ by an angle ψ. The resulting position vector is $\vec{r}$. Mathematically, such an operation is expressed as $\vec{r} = R_{\hat{u}}(\psi) \cdot \vec{r}_0$, where $R_{\hat{u}}(\psi)$ is given by Eq. (4.15).

By integration, one finds $\vec{r} = \exp(\psi G_{\hat{u}}) \cdot \vec{r}_0$, which yields the definition for the rotation matrix $R_{\hat{u}}(\psi) = \exp(\psi G_{\hat{u}})$, where $\vec{r}_0$ is the initial position vector. Fig. 4.7 depicts the effect of the rotation matrix $R_{\hat{u}}(\psi)$ on $\vec{r}_0$. Using the properties of the generator, $G^3_{\hat{u}} = -G_{\hat{u}}$ and $G^4_{\hat{u}} = -G^2_{\hat{u}}$, it follows,

$$R_{\hat{\mathbf{u}}}(\psi) = e^{\psi G_{\hat{\mathbf{u}}}} = I + \sin\psi \cdot G_{\hat{\mathbf{u}}} + (1 - \cos\psi) \cdot G^2_{\hat{\mathbf{u}}}. \tag{4.15}$$

An physical vector $\overrightarrow{\mathbf{A}} = (A_x, A_y, A_z)$ transforms in the same way as the position vectors and hence,

$$\begin{pmatrix} A_x \\ A_y \\ A_z \end{pmatrix} = R_{\hat{\mathbf{u}}}(\psi) \begin{pmatrix} A_{x0} \\ A_{y0} \\ A_{z0} \end{pmatrix}. \tag{4.16}$$

Moreover, rotation is a unitary transformation, and transpose of $R_{\hat{\mathbf{u}}}(\psi)$ is equivalent to the

reverse operation, i.e.,

$$\left(R_{\hat{\mathbf{u}}}\left(\psi\right)\right)^{T} = \left(R_{\hat{\mathbf{u}}}\left(\psi\right)\right)^{-1} = R_{\hat{\mathbf{u}}}\left(-\psi\right). \tag{4.17}$$

Despite the fact that $R_{\hat{u}}(\psi)$ describes a finite rotation about $\hat{u}$, it will be used for small-angle rotations as well because we found that Eq. (4.15) converges much faster than its truncated form, $R_{\hat{u}}(\psi) \simeq I + \sin\psi \cdot G_{\hat{u}}$ when ψ is small.

4.3.2.2 Rotation Matrix for a Coordinate System

Fig. 4.8 shows that the body fixed coordinate system $Oxyz$ can be generated by rotating the laboratory frame coordinate system $O_0x_0y_0z_0$ around a unit vector $\hat{\mathbf{u}}$ by an angle α. I want to know how to express $\hat{\mathbf{x}}$, $\hat{\mathbf{y}}$, $\hat{\mathbf{z}}$ in terms of $\hat{\mathbf{x}}_0$, $\hat{\mathbf{y}}_0$, $\hat{\mathbf{z}}_0$.

According to Eq. (4.16), the coordinates of $\hat{\mathbf{x}}$ in $O_0x_0y_0z_0$ is

$$\begin{pmatrix} x_1 \\ x_2 \\ x_3 \end{pmatrix} = R_{\hat{\mathbf{u}}}\left(\alpha\right) \begin{pmatrix} 1 \\ 0 \\ 0 \end{pmatrix}.$$

It is getting the first column of matrix $R_{\hat{\mathbf{u}}}\left(\alpha\right)$. As a result, I can write

$$\hat{\mathbf{x}} = \left[R_{\hat{\mathbf{u}}}\left(\alpha\right)\right]_{11}\hat{\mathbf{x}}_0 + \left[R_{\hat{\mathbf{u}}}\left(\alpha\right)\right]_{21}\hat{\mathbf{y}}_0 + \left[R_{\hat{\mathbf{u}}}\left(\alpha\right)\right]_{31}\hat{\mathbf{z}}_0. \tag{4.18}$$

Similarly for $\hat{\mathbf{y}}'$ and $\hat{\mathbf{z}}'$, I have

$$\begin{pmatrix} y_1 \\ y_2 \\ y_3 \end{pmatrix} = R_{\hat{\mathbf{u}}}\left(\alpha\right) \begin{pmatrix} 0 \\ 1 \\ 0 \end{pmatrix}, \quad \text{and} \quad \begin{pmatrix} z_1 \\ z_2 \\ z_3 \end{pmatrix} = R_{\hat{\mathbf{u}}}\left(\alpha\right) \begin{pmatrix} 0 \\ 0 \\ 1 \end{pmatrix}.$$

And

$$\hat{\mathbf{y}} = \left[R_{\hat{\mathbf{u}}}\left(\alpha\right)\right]_{12}\hat{\mathbf{x}}_0 + \left[R_{\hat{\mathbf{u}}}\left(\alpha\right)\right]_{22}\hat{\mathbf{y}}_0 + \left[R_{\hat{\mathbf{u}}}\left(\alpha\right)\right]_{32}\hat{\mathbf{z}}_0 \tag{4.19}$$

$$\hat{\mathbf{z}} = \left[R_{\hat{\mathbf{u}}}\left(\alpha\right)\right]_{13}\hat{\mathbf{x}}_0 + \left[R_{\hat{\mathbf{u}}}\left(\alpha\right)\right]_{23}\hat{\mathbf{y}}_0 + \left[R_{\hat{\mathbf{u}}}\left(\alpha\right)\right]_{33}\hat{\mathbf{z}}_0 \tag{4.20}$$

If I define a product between a 3×3 matrix M and a set of axial unit vectors $\left(\hat{\mathbf{x}}, \hat{\mathbf{y}}, \hat{\mathbf{z}}\right)^{\mathrm{T}}$ as

$$M\begin{pmatrix}\hat{\mathbf{x}}\\ \hat{\mathbf{y}}\\ \hat{\mathbf{z}}\end{pmatrix}=\begin{pmatrix}M_{11}\hat{\mathbf{x}}+M_{12}\hat{\mathbf{y}}+M_{13}\hat{\mathbf{z}}\\ M_{21}\hat{\mathbf{x}}+M_{22}\hat{\mathbf{y}}+M_{23}\hat{\mathbf{z}}\\ M_{31}\hat{\mathbf{x}}+M_{32}\hat{\mathbf{y}}+M_{33}\hat{\mathbf{z}}\end{pmatrix},$$

then Eq. (4.18), (4.19) and (4.20) are equivalent to

$$\begin{pmatrix}\hat{\mathbf{x}}\\ \hat{\mathbf{y}}\\ \hat{\mathbf{z}}\end{pmatrix}=\left[R_{\hat{\mathbf{u}}}(\alpha)\right]^{T}\begin{pmatrix}\hat{\mathbf{x}}_0\\ \hat{\mathbf{y}}_0\\ \hat{\mathbf{z}}_0\end{pmatrix}=R_{\hat{\mathbf{u}}}(-\alpha)\begin{pmatrix}\hat{\mathbf{x}}_0\\ \hat{\mathbf{y}}_0\\ \hat{\mathbf{z}}_0\end{pmatrix}. \tag{4.21}$$

Eq. (4.21) shows how the axial vectors of a body-fixed coordinate system $Oxyz$ are expressed in terms of the axial vectors of the laboratory frame coordinate system $O_0x_0y_0z_0$, when $Oxyz$ is generated by rotating $O_0x_0y_0z_0$ around a unit vector $\hat{\mathbf{u}}$ by an angle α.

In addition, I want to know how the coordinates of a position vector $\overrightarrow{\mathbf{r}}$ transform between the two coordinate systems. As shown in Fig. 4.8, $\overrightarrow{\mathbf{r}}$ can be expressed in either the laboratory frame, $O_0x_0y_0z_0$, with the components $(r_{x_0},\, r_{y_0},\, r_{z_0})$, or in the body-fixed frame, $Oxyz$, with the components $(r_x,\, r_y,\, r_z)$. When generating $Oxyz$, if $\overrightarrow{\mathbf{r}}$ also rotates around $\hat{\mathbf{u}}$ by an angle α, then vector $\overrightarrow{\mathbf{r}}'$ is generated. $\overrightarrow{\mathbf{r}}'$ is expressed in $Oxyz$ with components $\left(r'_x,\, r'_y,\, r'_z\right)$. By the definition of $\overrightarrow{\mathbf{r}}'$, we know that

$$\begin{pmatrix}r_{x_0}\\ r_{y_0}\\ r_{z_0}\end{pmatrix}=\begin{pmatrix}r'_x\\ r'_y\\ r'_z\end{pmatrix}.$$

According to Eq. (4.16),

$$\begin{pmatrix}r'_x\\ r'_y\\ r'_z\end{pmatrix}=R_{\hat{\mathbf{u}}}(\alpha)\begin{pmatrix}r_x\\ r_y\\ r_z\end{pmatrix}.$$

Consequently,

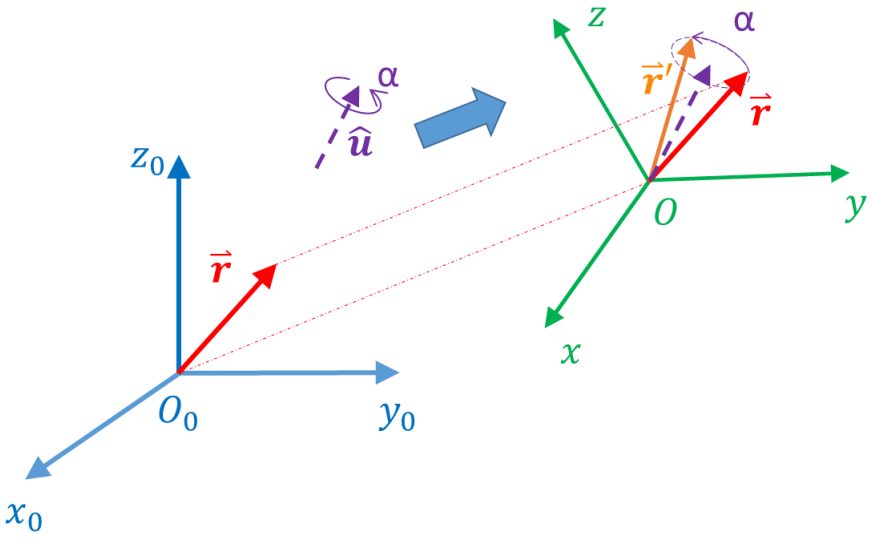

Figure 4.8: Coordinates Transformation between Two Frames. The plot shows that frame $Oxyz$, and vector $\mathbf{r}'$ is generated by rotating frame $O_0x_0y_0z_0$ and vector $\mathbf{r}$ around axis $\hat{\mathbf{u}}$ by an angle α.

$$\begin{pmatrix} r_{x_0} \\ r_{y_0} \\ r_{z_0} \end{pmatrix} = R_{\hat{\mathbf{u}}}(\alpha) \begin{pmatrix} r_x \\ r_y \\ r_z \end{pmatrix},$$

or

$$\begin{pmatrix} r_x \\ r_y \\ r_z \end{pmatrix} = R_{\hat{\mathbf{u}}}(-\alpha) \begin{pmatrix} r_{x_0} \\ r_{y_0} \\ r_{z_0} \end{pmatrix}. \tag{4.22}$$

Eq. (4.22) relates the coordinates of a position vector in the new frame $Oxyz$ to its coordinates in the old frame $O_0x_0y_0z_0$, and Eq. (4.21) expresses axial vectors of frame $Oxyz$ in terms of those in frame $O_0x_0y_0z_0$.

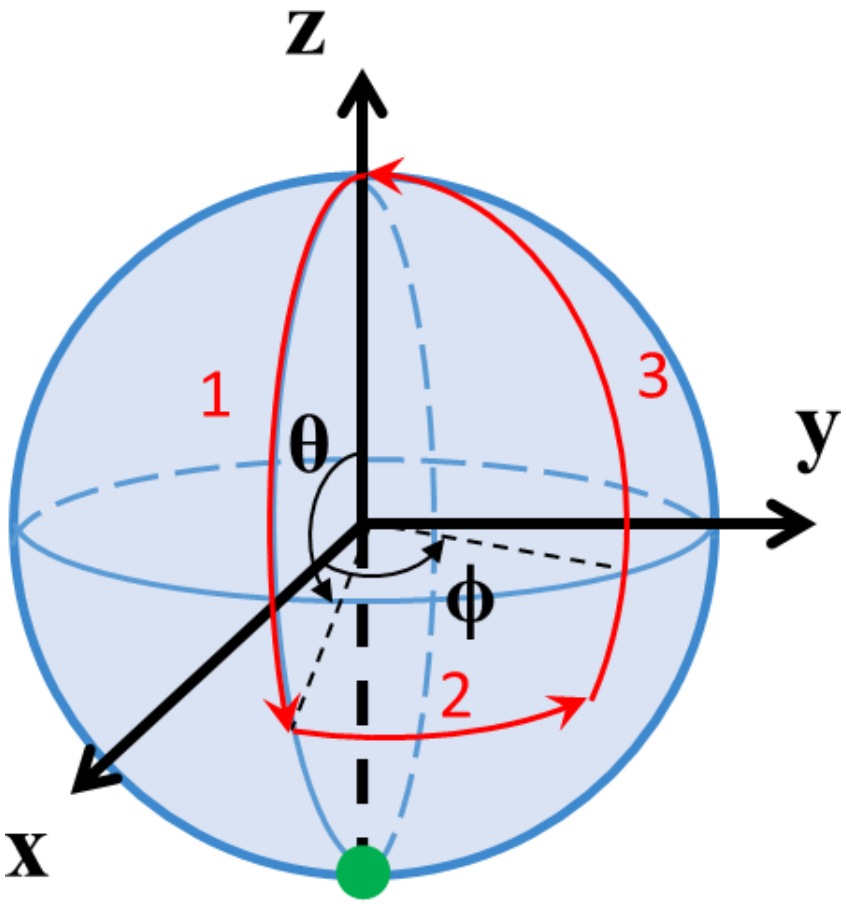

Figure 4.9: Flagellum Flick Path Σ Observed in the Body-Fixed Frame.

4.3.3 Angular and Translational Displacements of the Cell Body

The above derivation shows that the motion of the cell body is a function of the angular displacement of the flagellum. For bacterial motion to be cyclic, the flagellum must recover its origin position after a flick. Hence, the motion of the flagellum can be characterized by a closed path Σ on an unisphere with θ and ϕ being the independent variables. There are uncountable numbers of possibilities for Σ, but for a simple analysis we assume that the flagellum follows the path as illustrated in Fig. 4.9. This path consists of three segments: (i) $\phi = 0$ and θ goes from 0 to θ_0; (ii) $\theta = \theta_0$ and ϕ goes from 0 to ϕ_0; and (iii) $\phi = \phi_0$ and θ goes from θ_0 to 0.

Canceling out dt on both sides of equations for the translational and rotational velocities, i.e., Eq.(4.11) and (4.12) respectively, the linear and angular displacements of the cell body are given in terms of θ and ϕ,

$$\begin{pmatrix} dx \\ dy \\ dz \end{pmatrix} = -AL \begin{pmatrix} -\sin\phi & \cos\theta\cos\phi \\ \cos\phi & \cos\theta\sin\phi \\ 0 & -\sin\theta \end{pmatrix} \begin{pmatrix} \sin\theta d\phi \\ d\theta \end{pmatrix}, \tag{4.23}$$

$$\begin{pmatrix} d\Psi_x \\ d\Psi_y \\ d\Psi_z \end{pmatrix} = B \begin{pmatrix} \sin\phi & \cos\theta\cos\phi \\ -\cos\phi & \cos\theta\sin\phi \\ 0 & -\sin\theta \end{pmatrix} \begin{pmatrix} d\theta \\ \sin\theta d\phi \end{pmatrix}, \tag{4.24}$$

and can be integrated. Eq.(4.24) indicates that the rotation is about an instantaneous rotation axis $d\vec{\Psi}$, which is characterized by the unit vector $\hat{\mathbf{u}}$,

$$\hat{\mathbf{u}} = \frac{1}{d\Psi} \begin{pmatrix} d\Psi_x \\ d\Psi_y \\ d\Psi_z \end{pmatrix},$$

with $d\Psi = \sqrt{d\Psi_x^2 + d\Psi_y^2 + d\Psi_z^2}$. Eqs.(4.23) and (4.24) represent displacements expressed in terms of coordinates in the body-fixed frame. This frame of reference is moving and thus does not reflect the displacements of the cell body relative to the laboratory frame, which is what we are interested. It is thus necessary to transform the displacements from the

body-fixed frame to the laboratory frame. The complication of the problem is the fact that the rotation axis $\hat{\mathbf{u}}$ keeps changing along the path Σ.

To solve the problem, I divide flagellar off-axis rotation path into n small segments. Each segment is small enough such that the final results, after the summation, is independent of n. For the i$^{\text{th}}$ segment, by integrating Eq. (4.23) and (4.24), I get the translational displacement $\Delta\mathbf{s}_i = \int_{i-1}^{i}(dx,\, dy,\, dz) = (\Delta x_i,\, \Delta y_i,\, \Delta z_i)$ and rotational displacement $\Delta\Psi_i = \int_{i-1}^{i}(d\Psi_x,\, d\Psi_y,\, d\Psi_z) = (\Delta\Psi_{i,x},\, \Delta\Psi_{i,y},\, \Delta\Psi_{i,z})$ in the body-fixed frame. These segmental integrations are path-dependent and will be individually transformed to the laboratory frames before the summation is performed.

4.3.3.1 The Path Integral Now let's use the prescribed flagellar path Σ to calculate the cell body displacements in the body-fixed frame according to Eq.(4.23) and (4.24):

(i) $\theta : 0 \to \theta_0$, $\phi = 0$. Dividing this segment into n sections with equal intervals, $\Delta\theta = \frac{\theta_0}{n}$. The contribution due to the i$^{\text{th}}$ section is given by,

$$\begin{cases} \Delta x_i = -AL\int_{(i-1)\Delta\theta}^{i\Delta\theta}\cos\theta d\theta, \\ \Delta y_i = 0, \\ \Delta z_i = AL\int_{(i-1)\Delta\theta}^{i\Delta\theta}\sin\theta d\theta, \end{cases}$$

and

$$\begin{cases} \Delta\Psi_x = 0, \\ \Delta\Psi_y = -B\Delta\theta, \\ \Delta\Psi_z = 0. \end{cases}$$

(ii) $\theta = \theta_0$, $\phi : 0 \to \phi_0$. Dividing this segment into n sections with equal intervals, $\Delta\phi = \frac{\phi_0}{n}$. The contribution due to the i$^{\text{th}}$ section is given by,

$$\begin{cases} \Delta x_i = AL\sin\theta_0 \int_{(i-1)\triangle\phi}^{i\triangle\phi} \sin\phi d\phi, \\ \Delta y_i = AL\sin\theta_0 \int_{(i-1)\triangle\phi}^{i\triangle\phi} \cos\phi d\phi, \\ \Delta z_i = 0, \end{cases}$$

and

$$\begin{cases} \Delta\Psi_x = B\sin\theta_0\cos\theta_0 \int_{(i-1)\Delta\phi}^{i\Delta\phi} \cos\phi d\phi, \\ \Delta\Psi_y = B\sin\theta_0\cos\theta_0 \int_{(i-1)\Delta\phi}^{i\Delta\phi} \sin\phi d\phi, \\ \Delta\Psi_z = -B\sin^2\theta_0\Delta\phi. \end{cases}$$

(iii) $\theta : \theta_0 \to 0$, $\phi = \phi_0$. Divide this segment into n sections with equal intervals, $\Delta\theta = \frac{\theta_0}{n}$. The contribution due to the i$^{\text{th}}$ section is given by,

$$\begin{cases} \Delta x_i = -AL\cos\phi_0 \int_{(n-i+1)\Delta\theta}^{(n-i)\Delta\theta} \cos\theta d\theta, \\ \Delta y_i = -AL\sin\phi_0 \int_{(n-i+1)\Delta\theta}^{(n-i)\Delta\theta} \cos\theta d\theta, \\ \Delta z_i = AL \int_{(n-i+1)\Delta\theta}^{(n-i)\Delta\theta} \sin\theta d\theta, \end{cases}$$

and

$$\begin{cases} \Delta\Psi_x = -B\sin\phi_0\Delta\theta, \\ \Delta\Psi_y = B\cos\phi_0\Delta\theta, \\ \Delta\Psi_z = 0. \end{cases}$$

We note that by the above chosen path Σ, the axis of rotation $\hat{\mathbf{u}}$ is constant for (i) and (iii) but not for (ii). Such simplification is absent if an arbitrary path is used.

4.3.3.2 Transition to the Laboratory Frame

According to Eq. 4.21, for each small segment, the base vectors in the "current" body-fixed frame are related to that of the laboratory frame by a rotation matrix. Let's call it matrix M. Then the translational displacement $(\Delta x_i, \Delta y_i, \Delta z_i)$ of each small segment is transformed back into the laboratory frame by the transpose of matrix M according to Eq.(4.22).

The i^{th} frame is connected to the $(\mathrm{i}-1)^{\mathrm{th}}$ frame by a rotation matrix $R_i = R_{\hat{\mathbf{u}}_i}(-\Delta\Psi_i)$, and is related to the laboratory frame by a rotation matrix $M_i = R_i \cdots R_2 R_1$. We find the iteration relation,

$$\begin{pmatrix} \hat{\mathbf{x}}'_i \\ \hat{\mathbf{y}}'_i \\ \hat{\mathbf{z}}'_i \end{pmatrix} = M_i \begin{pmatrix} \hat{\mathbf{x}} \\ \hat{\mathbf{y}} \\ \hat{\mathbf{z}} \end{pmatrix}, \quad \Delta\mathbf{s}_{i0} = \begin{pmatrix} \Delta x_{i0} \\ \Delta y_{i0} \\ \Delta z_{i0} \end{pmatrix} = (M_i)^{\mathrm{T}} \begin{pmatrix} \Delta x_i \\ \Delta y_i \\ \Delta z_i \end{pmatrix} \tag{4.25}$$

with the initial condition,

$$\begin{pmatrix} \hat{\mathbf{x}}'_0 \\ \hat{\mathbf{y}}'_0 \\ \hat{\mathbf{z}}'_0 \end{pmatrix} = \begin{pmatrix} \hat{\mathbf{x}} \\ \hat{\mathbf{y}} \\ \hat{\mathbf{z}} \end{pmatrix}, \quad \Delta\mathbf{s}_{10} = \begin{pmatrix} \Delta x_{10} \\ \Delta y_{10} \\ \Delta z_{10} \end{pmatrix} = \begin{pmatrix} \Delta x_1 \\ \Delta y_1 \\ \Delta z_1 \end{pmatrix},$$

since the first frame overlaps with laboratory frame.

After calculating all $3n$ segments, the translational displacements were added up to give the net displacement $\mathbf{s}$,

$$\mathbf{s} = \sum_{i=1}^{3n} \Delta\mathbf{s}_{i0}.$$

For the angular displacement, since the cell head is always pointing toward negative z-direction, the net rotational displacement is the angle Ψ between $-\hat{\mathbf{z}}$ at the beginning and the end of a flick. According to Eq. (4.25), $\hat{\mathbf{z}}'_{3n} = [M_{3n}]_{31}\,\hat{\mathbf{x}} + [M_{3n}]_{32}\,\hat{\mathbf{y}} + [M_{3n}]_{33}\,\hat{\mathbf{z}}$, i.e., $\Psi = \arccos(\hat{\mathbf{z}}'_{3n} \cdot \hat{\mathbf{z}}) = \arccos([M_{3n}]_{33})$.

4.3.4 Comparisons of the Simple Model with the Experimental Data

A Matlab function was written to implement the above calculation. Specifically the program calculates the cell body reorientation angle Ψ as a function of $x = a/L$ (the cell body to flagellar length ratio), as well as of the flagellar path parameters θ_0 and ϕ_0. In the calculation we assumed that $L = 3.7\,\mu m$ is constant, which represents the mean value measured for *V. alginolyticus* [81].

Fig. 4.10 shows a typical set of reorientation angles $\Psi(x)$ and displacements $s(x)$ for $\theta_0 = \frac{2\pi}{3}$ and $\phi_0 = 2\pi$. The $\Psi(x)$ curve (blue) reaches a maximum angle of 140^o for $x = 0.26$,

and $\Psi(x)$ decreases to 0 for both large and small x. The displacement curve (orange) $s(x)$ looks very different; it starts from zero for $x \simeq 0$, increases to form two peaks as x increases, and finally slowly decreases for larger x values.

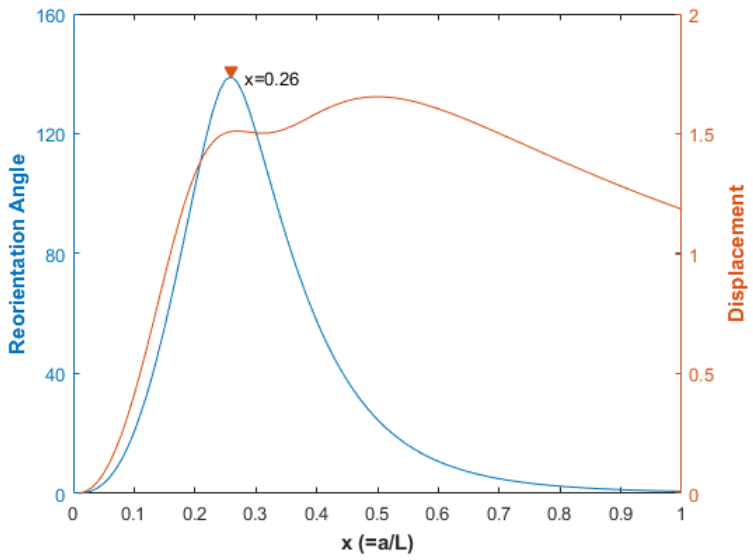

Figure 4.10: Cell-body reorientation angle $\Psi(x)$ (the blue curve) and displacement $s(x)$ (the orange curve) are plotted as a function of x for $\theta_0 = \frac{2\pi}{3}$ and $\phi_0 = 2\pi$. The inverted triangle indicates the peak position of Ψ, which is comparable to what we observed in the experiment (see below).

Fig. 4.11 displays how the angle $\Psi(x)$ changes for different values of θ_0 and ϕ_0, where x is fixed at 0.26. It is interesting that it is possible to make the reorientation angle Ψ reach $\sim 180^o$, which corresponds to a 0^o-flick; note that according to the definition of the angles in Fig. 4.1B, a 0^o flick angle corresponds to a 180^o cell body reorientation.

Thousands of wild-type *Vibrio alginolyticus* trajectories were video taped, and flick angles were recognized and calculated with a Matlab script (developed by myself). These flick angles were binned according to the cell-body size. Mean flick angles as a function of x are plotted in Fig. 4.13(A) as red circles with error bars. Cell body displacement is defined as the positional change from the frame with minimum speed at the flick and the following two frames, which is shown in Fig. 4.12. According to Xie (2011) [86] and Son (2013) [19], the

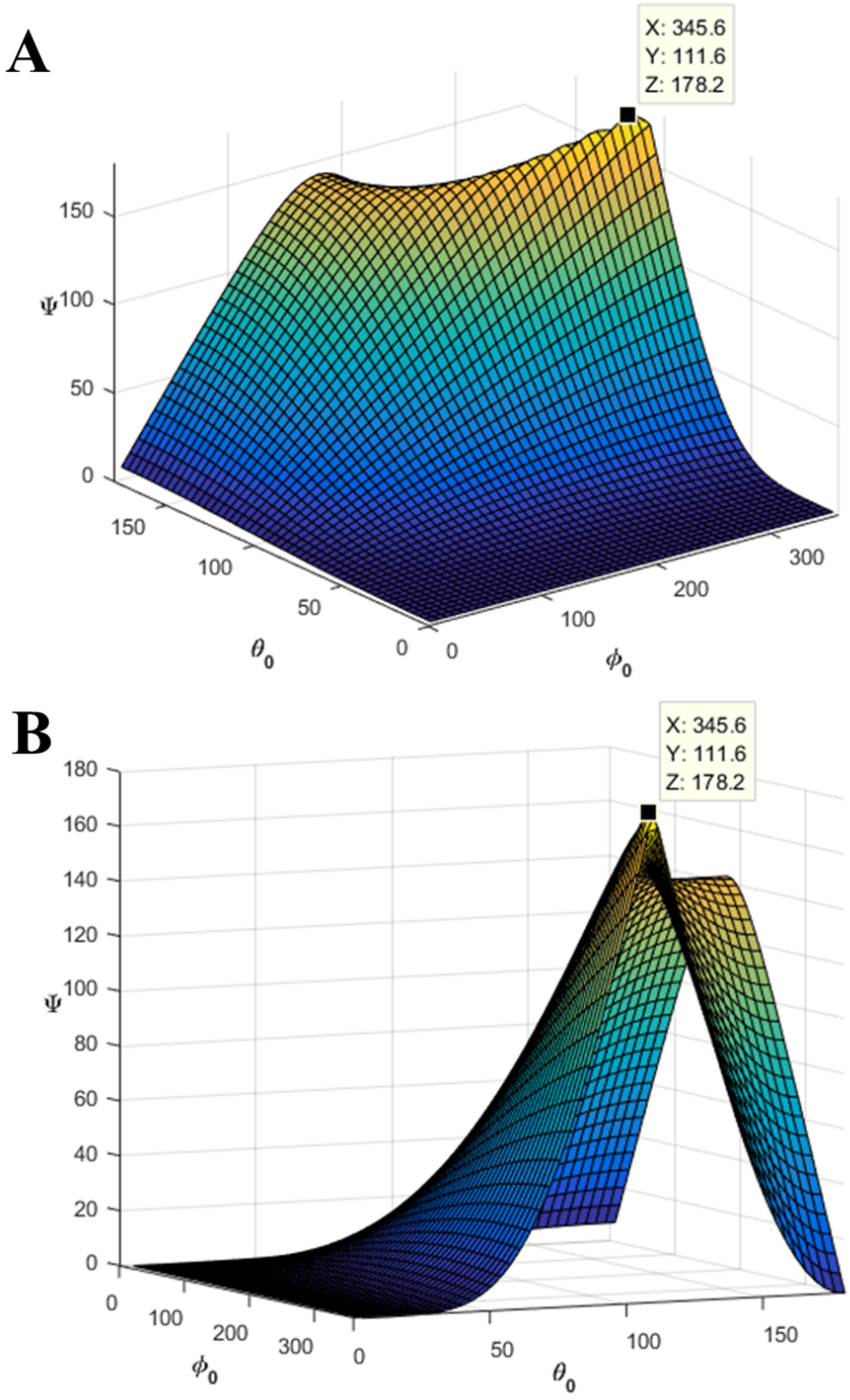

Figure 4.11: Cell-body reorientation angle as a function of θ_0 and ϕ_0. Here, $x = 0.26$ was used for the computation. Each graph has a marker showing the location of the maximum Ψ, where (X,Y,Z) corresponds to (θ, ϕ Ψ).

flick lasts for $\sim 60\,\text{ms}$, which corresponds to ~ 2 frames in my videos at 36 fps.

Using the model developed in this section, I got the best fit by eyeballing for the cell body reorientation angle data when $\theta_0 = 0.64\pi$ and $\phi_0 = 2.3\pi$ as shown in Fig. 4.13(A). However with the same set of parameters, this simple model doesn't provide a similarly good fit for the displacement data (as shown in Fig. 4.13(B), blue curve). Actually none of the $s\,(x)$ curves in Fig. 4.13(B) has the sharp decay as seen in the displacement data.

As a result, we concluded that this model is over-simplified and doesn't capture some important features of the flick process. We need a better model to describe this problem. Two approximations were made at the beginning of this model: 1) the cell body is spherical instead of being in a rod shape; 2) the flagellum is hinged at cell center rather than at cell pole. I think the second approximation has a larger impact on this problem, since it makes a non-symmetric configuration symmetrical. In the next section, I'm going to move the flagellum back to the cell pole, and develop an OFF-CENTER MODEL based on the discussions in this section.

4.4 A MORE REALISTIC MODEL (OFF-CENTER MODEL)

4.4.1 Mathematical Formulation of the Problem

Now let's make the model somewhat more realistic. In the above model, there are three simplifying features: (i) the flagellum is located at the cell center; (ii) the flagellum is a rigid straight rod instead of a helix; and (iii) the flagellum does not rotate about its own axis but pivoting about its base. We believe that (ii) is not very crucial to the kinetics of flicking and can be readily fixed even though the mathematical expression is not pretty, and (iii) is important but its mathematical treatment is too complicated to deal with in this thesis. Thus, in this chapter we will tackle issue (i) by moving the flagellum to the pole of the cell body as delineated in Fig. 4.14, and keep the cell body in a rigid spherical shape. The mathematical formulation of the resistive force acting on the flagellum is the same as before, but we need to take into account the differences in the translational and rotational velocities

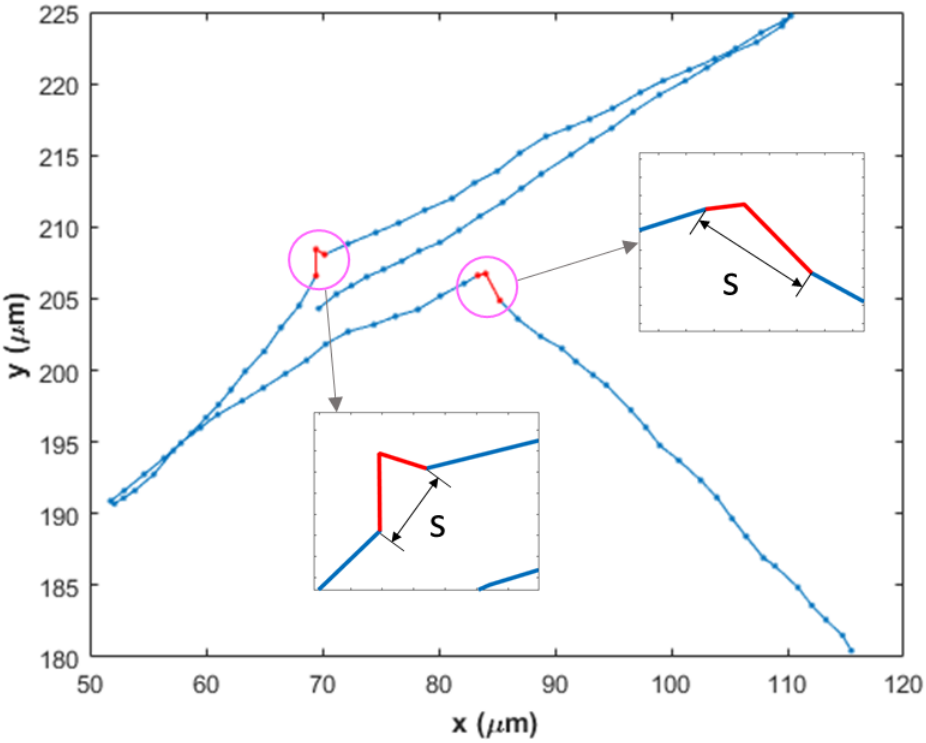

Figure 4.12: Cell Body Displacement in Flicks. Red segments indicate two successive frames where flicks take place.

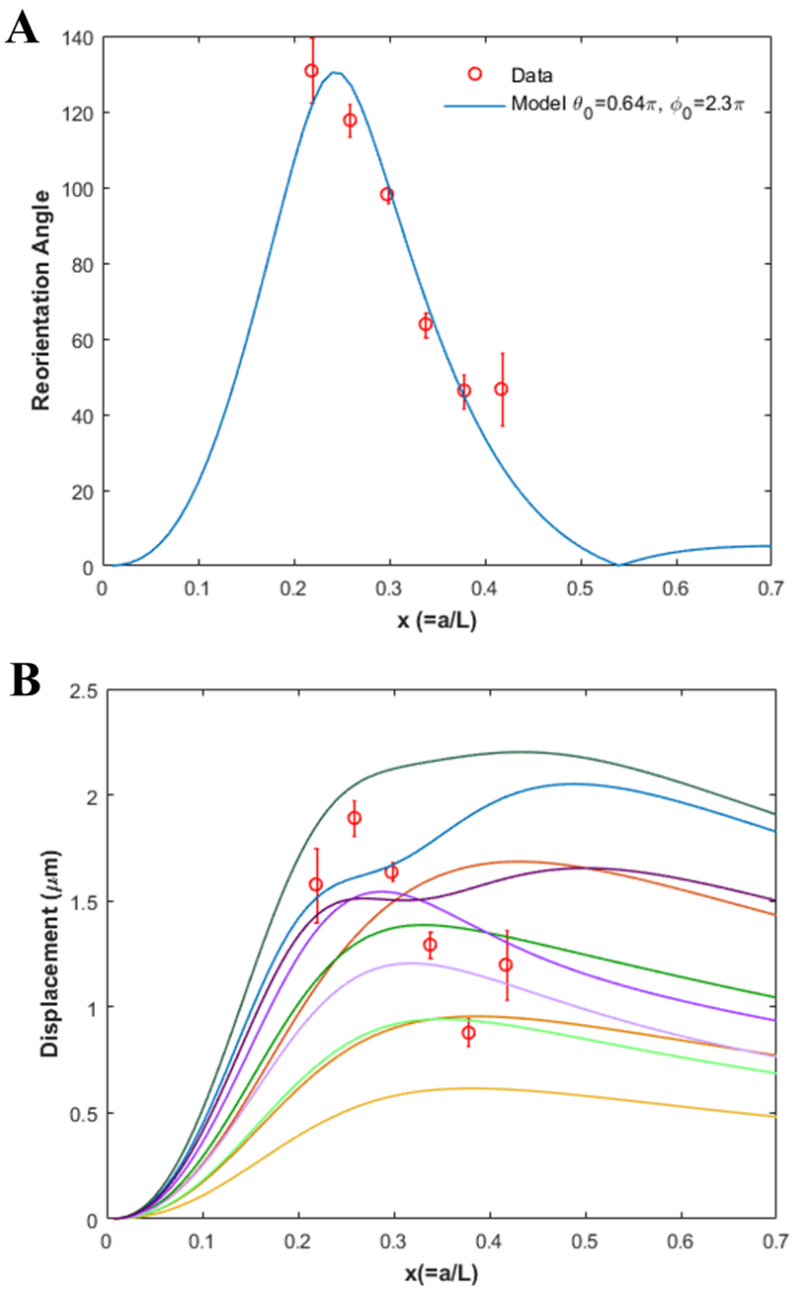

Figure 4.13: Experimental Reorientation Angle data (red circles with error bars) with a best fit $\Psi(x)$ curve (blue curve, $\theta_0 = 0.64\pi$, $\phi_0 = 2.3\pi$) from the model (A). Displacement data (red circles with error bars) and displacement $s(x)$ curves with different sets of θ_0, and ϕ_0 angles (B). The curves are divided into three groups: yellow ($\theta_0 = \frac{\pi}{3}$), green ($\theta_0 = \frac{\pi}{2}$), and purple ($\theta_0 = \frac{2\pi}{3}$). Within each group, a darker curve has a larger ϕ_0 value from the set $\phi_0 = \frac{\pi}{2}$, π, and 2π. The blue curve has the same parameter set with the one in (A), being $\theta_0 = 0.64\pi$, and $\phi_0 = 2.3\pi$

at the cell center $\mathbf{V}_c$ and $\mathbf{\Omega}_c$ and at the pole $\mathbf{V}_o$ and $\mathbf{\Omega}_o$.

Following the same procedure in section 4.3.1 and according to the resistive force theory [83], we find the total force $\mathbf{F}_f$ and the torque $\mathbf{N}_f$ on the flagellum is given by,

$$\mathbf{F}_f = L[\zeta_{\parallel}\hat{\mathbf{t}}\hat{\mathbf{t}} + \zeta_{\perp}(\mathbf{I} - \hat{\mathbf{t}}\hat{\mathbf{t}})] \cdot \mathbf{V_o} + \frac{\mathbf{L^2}}{\mathbf{2}}\zeta_{\perp}\left[\mathbf{\Omega_o} \times \hat{\mathbf{t}} + \dot{\theta}\hat{\mathbf{n}} + \sin\theta\dot{\phi}\hat{\mathbf{b}}\right],$$

$$\mathbf{N}_f = \frac{L^2\zeta_{\perp}}{2}\hat{\mathbf{t}} \times \mathbf{V_o} + \frac{\mathbf{L^3}\zeta_{\perp}}{\mathbf{3}}\left[\hat{\mathbf{t}} \times \left(\mathbf{\Omega_o} \times \hat{\mathbf{t}}\right) + \dot{\theta}\hat{\mathbf{b}} - \sin\theta\dot{\phi}\hat{\mathbf{n}}\right].$$

However, the force and toque on the cell body are changed due to the shift of the flagellar base.

$$\mathbf{F_b} = \overleftrightarrow{\sigma} \cdot \mathbf{dA},$$

$$\mathbf{N_b} = \mathbf{r}' \times \overleftrightarrow{\sigma} \cdot \mathbf{dA},$$

where $\mathbf{r}' = \mathbf{R} + \mathbf{r} = -R\hat{\mathbf{z}} + \mathbf{r}$ and $d\mathbf{A}$ is the surface element on the spherical cell body. $\overleftrightarrow{\sigma}$ is the viscous stress tensor acting on the cell and can be decomposed into two parts, $\overleftrightarrow{\sigma} = \overleftrightarrow{\sigma}_T + \overleftrightarrow{\sigma}_R$, where $\overleftrightarrow{\sigma}_T$ is a viscous stress tensor due to the translational motion with a velocity $\mathbf{V_C}$ at the cell center and $\overleftrightarrow{\sigma}_R$ is a stress tensor from the rotational motion about the cell center with the rotational velocity $\mathbf{\Omega_C} = \mathbf{\Omega_o}$. Since $\overleftrightarrow{\sigma}_R$ is symmetric about the cell center, the force acting on the cell body due to rotation is zero, $\overleftrightarrow{\sigma}_R d\mathbf{A} = \mathbf{0}$. Using the Stoke's law, therefore,

$$\mathbf{F}_b = \overleftrightarrow{\sigma} d\mathbf{A} = \overleftrightarrow{\sigma}_T d\mathbf{A} + \overleftrightarrow{\sigma}_R d\mathbf{A} = \overleftrightarrow{\sigma}_T d\mathbf{A} = Z\mathbf{V}_C,$$

where $Z = 6\pi\eta a$ is the viscous drag coefficient for a sphere of radius a, $\eta = 0.01\,\mathrm{g}\cdot\mathrm{cm}^{-1}\cdot\mathrm{s}^{-1}$ is the viscosity of the media, which I used the viscosity of water. Additionally, since $\overleftrightarrow{\sigma}_T$ is axial-symmetric about the cell translational direction, $\oiint \mathbf{r} \times \overleftrightarrow{\sigma}_T \cdot d\mathbf{A} = 0$. This allows us to write,

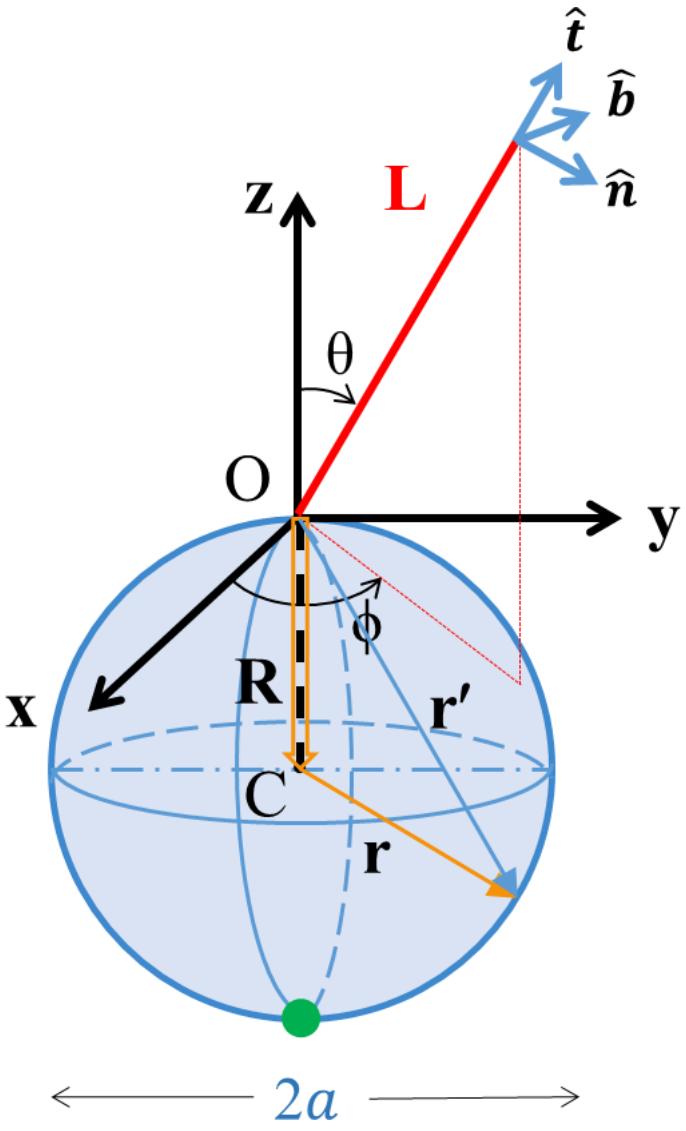

Figure 4.14: Cell Body Geometry of the Improved Model. Unlike the previous model, now the flagellum is moved to the cell pole. The base of the flagellum is at the origin of the cell body-fixed coordinates. Again, the cell body is in a spherical shape, and the cell head (a green dot) is pointing in the negative z direction. The movement of the flagellum is specified by polar and azimuthal angles$(\theta(t), \phi(t))$ as before. The position of a point on cell surface relative to the joint point O is given by $\mathbf{r}' = \mathbf{R} + \mathbf{r}$, where $\mathbf{R}$ is a constant vector that connects the origin O and cell center C as shown. $\mathbf{r}$ is a position vector of that point on the cell surface relative to the cell center C.

$$
\begin{aligned}
\mathbf{N}_b &= \mathbf{r}' \times \overleftrightarrow{\sigma}\mathbf{dA} = \mathbf{R} \times (\overleftrightarrow{\sigma}_{\mathbf{T}} + \overleftrightarrow{\sigma}_{\mathbf{R}})\,\mathbf{dA} + \mathbf{r} \times (\overleftrightarrow{\sigma}_{\mathbf{T}} + \overleftrightarrow{\sigma}_{\mathbf{R}})\,\mathbf{dA} \\
&= \mathbf{R} \times \overleftrightarrow{\sigma}_T d\mathbf{A} + \mathbf{r} \times \overleftrightarrow{\sigma}_R d\mathbf{A} \\
&= \mathbf{R} \times Z\mathbf{V}_C + M\boldsymbol{\Omega}_C.
\end{aligned}
$$

The condition of free-body swimming demands, $\mathbf{F}_f + \mathbf{F}_b = 0$, and $\mathbf{N}_f + \mathbf{N}_b = 0$, which correspond to,

$$
\begin{aligned}
L\left(\zeta_{\parallel} - \zeta_{\perp}\right)\left(\mathbf{V}_o \cdot \hat{\mathbf{t}}\right)\hat{\mathbf{t}} + \left(L\zeta_{\perp} + Z\right)\mathbf{V}_o + \tfrac{L^2}{2}\zeta_{\perp}\Big[\boldsymbol{\Omega}_o \times \hat{\mathbf{t}} + \dot{\theta}\hat{\mathbf{n}} \\
+ \sin\theta\dot{\phi}\hat{\mathbf{b}}\Big] + Z\boldsymbol{\Omega}_o \times \mathbf{R} = 0,
\end{aligned}
\tag{4.26}
$$

$$
\begin{aligned}
\tfrac{L^2\zeta_{\perp}}{2}\hat{\mathbf{t}} \times \mathbf{V}_o + \tfrac{L^3\zeta_{\perp}}{3}\left[\hat{\mathbf{t}} \times \left(\boldsymbol{\Omega}_o \times \hat{\mathbf{t}}\right) + \dot{\theta}\hat{\mathbf{b}} - \sin\theta\dot{\phi}\hat{\mathbf{n}}\right] + \mathbf{R} \times Z\mathbf{V}_o \\
+ Z\mathbf{R} \times (\boldsymbol{\Omega}_o \times \mathbf{R}) + M\boldsymbol{\Omega}_o = 0
\end{aligned}
\tag{4.27}
$$

where $\mathbf{V}_C$ is related to $\mathbf{V}_o$ by $\mathbf{V}_C = \mathbf{V}_o + \boldsymbol{\Omega}_o \times \mathbf{R}$.

$\mathbf{V}_o$, $\boldsymbol{\Omega}_o$ and $\mathbf{V}_C$ can be solved explicitly as functions of $\dot{\theta}$ and $\dot{\phi}$. Appendix F shows the full calculation.

4.4.2 Curve Fitting

This modified (flagellar off-center) model was implemented using the same algorithm developed in section 4.3.3, except here the translational and rotational velocities, Eqs. (4.23) and (4.24), should be replaced by that given in Eqs. (F.7) and (F.8). The segmental integrations in section 4.3.3.1 should be modified accordingly. A Matlab script was written to calculate the displacement s and reorientation angle Ψ given the bacterial cell body-flagellum ratio x, and the flagellar path specified by (θ_0, ϕ_0). I found the best fit for experimental data, Ψ and s vs. x, to be $\theta_0 = 113.4^o$, and $\phi_0 = 378^o$, which is shown in Fig. 4.15. Here $\Psi(x)$ is a good fit, and $s(x)$ captures the feature of sharp decrease when x is large. The slight mismatch between the displacement data and fitting curve could result from the propulsion of flagellum, rotation about its own axis, which is ignored in the current model. Bacterial propulsion during a flick can drive the cell body forward by an additional distance and may account for the discrepancy see in Fig. 4.15(B).

Each point in Fig. 4.15(A) or (B) represents the mean reorientation angle and the mean displacement for a bacterial population of a fixed cell-body size. In priori, one does not expect that bacteria of different sizes follow the same path characterized by the two parameters θ_0 and ϕ_0 or for that matter follow the simple path prescribed. The mere fact that all data acquired can be fit using a single set of parameters (θ_0, ϕ_0) is very interesting, suggesting that bacteria of all different sizes or $x = a/L$ may use a similar tactic to change directions.

How do we know that a bacterial flagellum can indeed carry out such a maneuver during a flick? By studying tethered wt *V. aglinolyticus*, we observed that bacterial flagellum is quite flexible and moves about in a fashion similar to what is described in the theory. Since in the experiment the cell body is fixed on the glass surface, the ϕ degree of freedom is fixed, but θ is free to change and can be observed. Fig. 4.16 displays a sequence of video frames showing the waving of the flagellum of a bacterium about its base. The rate of the video is 36 fps. The action is slower than we observed in a flick during free swimming, but the angular variation seen in this video indicates that the bacterium can maneuver its flagellum and make the bending θ as large as 120°, which is similar to the best fitted result.

It may be useful to compare the theoretical results for $\Psi(\theta_0, \phi_0)$ calculated based the modified model with the simple model proposed by Dr. Fu (personal communications). Fig. 4.11 and Fig. 4.17 show that both models can reach a similar reorientation angle, however for the off-center case, large reorientation angles are met at a larger θ_0 angles, 133° vs. 115°. But ϕ_0 for the off-center model is smaller, 295° vs. 345°. As we will show below, the energy expenditure for a flick is about the same for the two models.

4.5 ENERGY DISSIPATION

In order to know whether the flagellar motor of *V. alginolyticus* is capable of powering up the flick motion, I calculated the energy dissipation rate based on translational and rotational motions of the cell body and the flagellum.

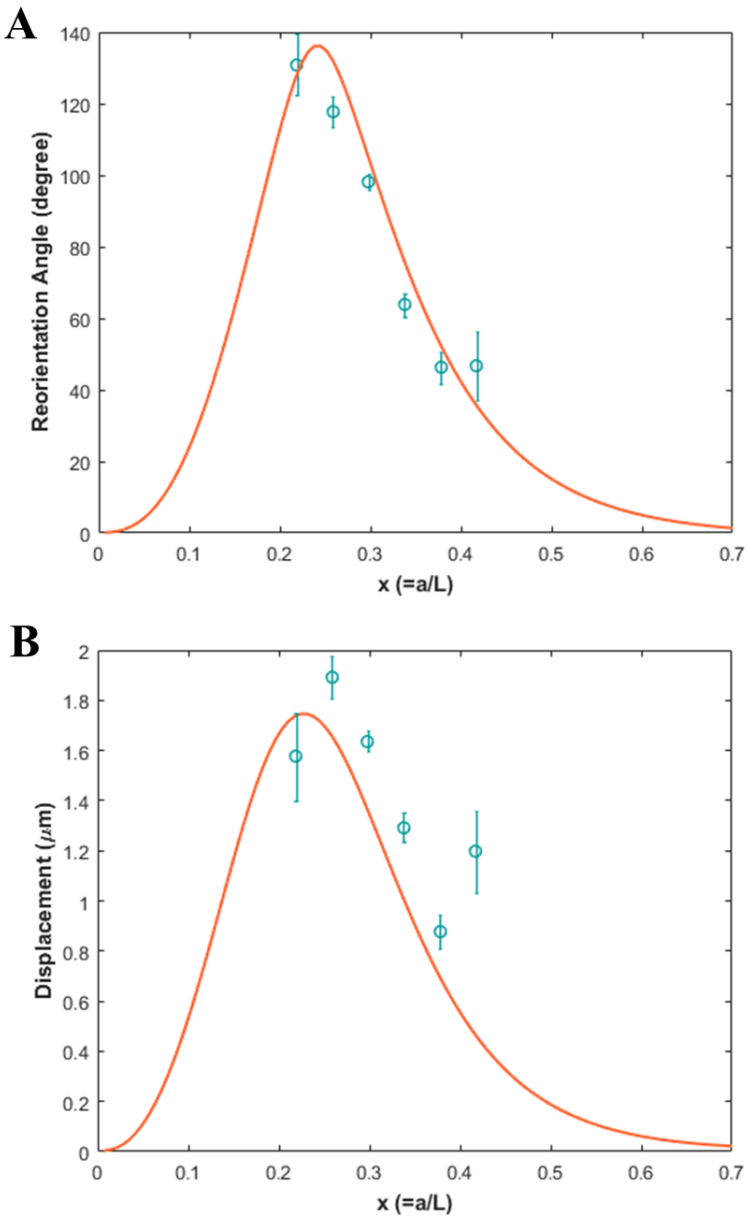

Figure 4.15: Cell-Body Reorientation Angle $\Psi(x)$ (A) and Displacement $s(x)$ (B) for Wild Type YM4 and Fitting with the Improved Model. Experimental data are shown as blue circles along with error bars (standard deviation of the mean). The orange curves are the fitting curves according to Eqs. (F.7) and (F.8), where $\theta_0 = 113.4^{\circ}$ and $\phi_0 = 378^{\circ}$ are used.

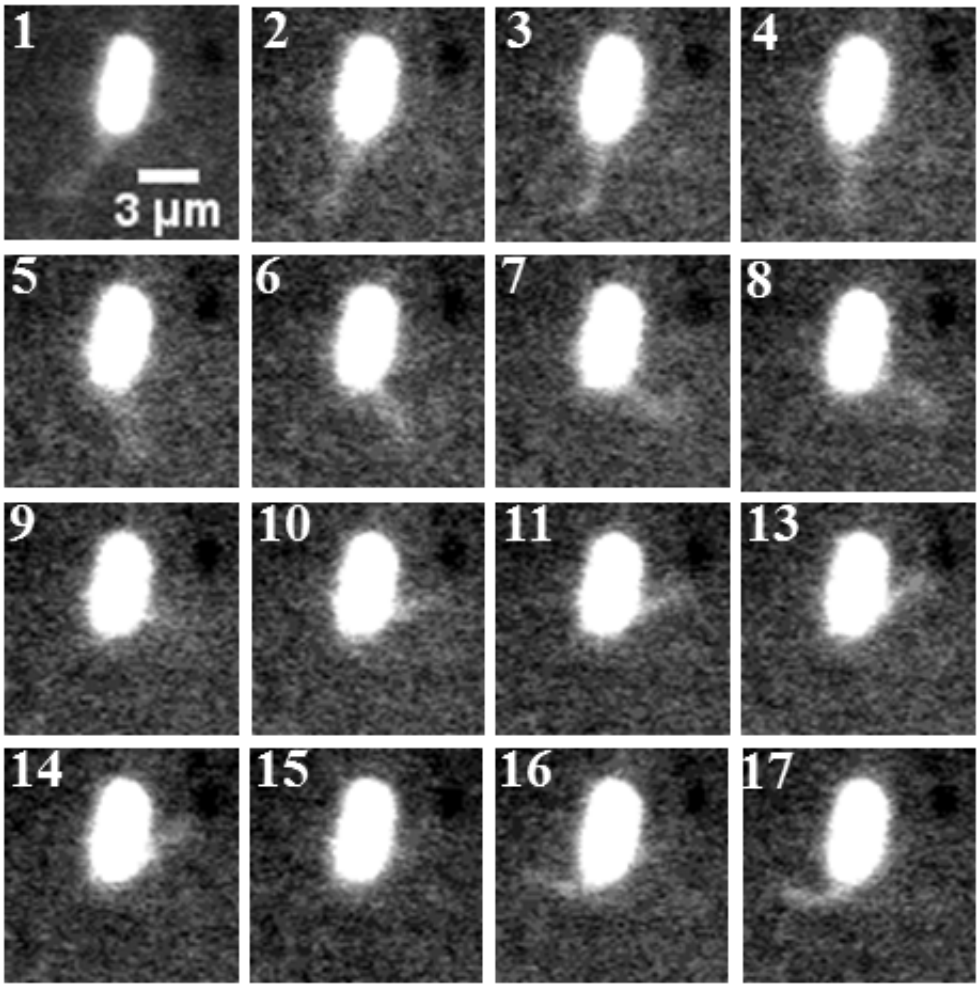

Figure 4.16: Near Surface Flagellum Rotations. The bacterium is tethered to the glass substrate using poly-L-lysine (see MM). The time interval between the frames is 28 ms. The flagellum waves about its base and can bend as much as 120°, which is close to the best fit with $\theta_0 \simeq 113°$.

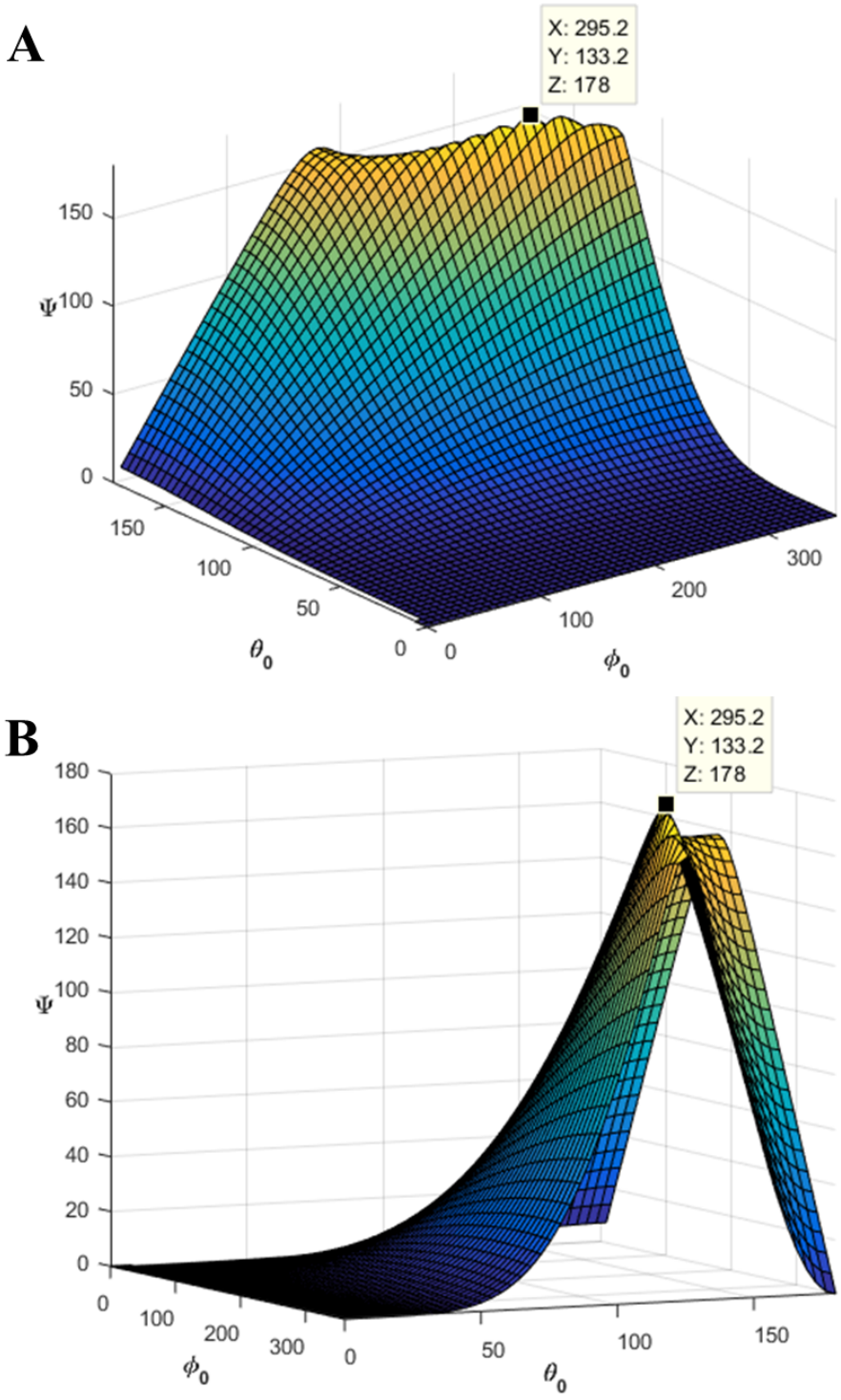

Figure 4.17: Cell-Body Reorientation Angle Ψ as a Function of Flagellar Path Parameters θ_0 and ϕ_0. The calculation is carried out for $x = 0.26$. Each graph has a marker indicating the maximum reorientation angle in the graph, where (X, Y, Z) corresponds to (ϕ_0, θ_0, Ψ) in degrees.

4.5.1 Calculation Based on the Simple Model

For the simple model described in section 4.3.1, the cell body energy dissipation rate is

$$P_b = \mathbf{F} \cdot \mathbf{V} + \mathbf{N} \cdot \mathbf{\Omega} = Z\mathbf{V}^2 + M\mathbf{\Omega}^2. \tag{4.28}$$

Substituting $\mathbf{V}$ and $\mathbf{\Omega}$ using Eqs. (4.11) and (4.12), I obtained

$$P_b = \left(ZA^2L^2 + MB^2\right)\left(\dot{\theta}^2 + \dot{\phi}^2 \sin^2\theta\right).$$

The flagellar energy dissipation rate is

$$P_f = \int_0^L ds \mathbf{f}\left(s\right) \cdot \dot{\mathbf{r}}\left(s\right), \tag{4.29}$$

where $\mathbf{f}$ is the force per unit length on the flagellum, which is given by Eq. (4.4), and flagellar velocity $\dot{\mathbf{r}}$ is given by Eq. (4.3).

Following the definitions in Eq. (4.3) and (4.4), a segment of the flagellum at location s has a linear velocity $\mathbf{v}_f \equiv s\mathbf{v}_{fo} \equiv s\left(\mathbf{\Omega} \times \hat{\mathbf{t}} + \dot{\theta}\hat{\mathbf{n}} + \sin\theta\dot{\phi}\hat{\mathbf{b}}\right)$. It is clear that $\mathbf{v}_f \cdot \mathbf{V}_t = 0$. The energy dissipation rate per unit length P_f in Eq. (4.29) is then given by,

$$\begin{aligned} P_f &= \int_0^L ds \left\{\left[\zeta_\parallel \hat{\mathbf{t}}\hat{\mathbf{t}} + \zeta_\perp(\mathbf{I} - \hat{\mathbf{t}}\hat{\mathbf{t}})\right] \cdot \mathbf{V} + \zeta_\perp \mathbf{v}_f\right\} \cdot (\mathbf{V} + \mathbf{v}_f) \\ &= \int_0^L ds \left[\zeta_\parallel \mathbf{V}_t^2 + \zeta_\perp \mathbf{V}_\perp^2 + \zeta_\perp \mathbf{v}_f \cdot (\mathbf{V}_\perp + \mathbf{V}) + \zeta_\perp \mathbf{v}_f^2\right] \\ &= \left(\zeta_\parallel \mathbf{V}_t^2 + \zeta_\perp \mathbf{V}_\perp^2\right) L + L^2 \zeta_\perp \mathbf{v}_{fo} \cdot \mathbf{V}_\perp + \frac{1}{3} L^3 \zeta_\perp \mathbf{v}_{fo}^2 \end{aligned} \tag{4.30}$$

Substituting Eqs. (4.11) and (4.12) in the above equations, I found

$$\begin{aligned} P_f &= \zeta_\perp L^3 \left[A^2 - (1-B)\,A + \frac{1}{3}(1-B)^2\right]\left(\dot{\theta}^2 + \dot{\phi}^2 \sin\theta\right) \\ &\equiv \zeta_\perp L^3 C \left(\dot{\theta}^2 + \dot{\phi}^2 \sin\theta\right), \end{aligned}$$

where $C = A^2 - (1-B)\,A + \frac{1}{3}\,(1-B)^2$. This yields the total energy dissipation rate for the cell body and the flagellum,

$$P = P_f + P_b = \left(MB^2 + \zeta_\perp L^3 C + ZA^2L^2\right)\left(\dot{\theta}^2 + \dot{\phi}^2 \sin^2\theta\right).$$

Assuming $\dot{\theta} = \dot{\phi} = \omega_0$ to be constant, the total energy dissipated along the path Σ is given by,

$$W = \left(ZA^2L^2 + MB^2 + \zeta_\perp L^3 C\right)\left(2\theta_0 + \sin^2\theta_0\phi_0\right)\omega_0.$$

Suppose flagellum finish a $2\theta_0+\phi_0 \sim 3.3\pi$ angular flick in 60 ms, i.e. $\omega_0 \sim 170\,\mathrm{rad}\cdot\mathrm{s}^{-1}$. Using $x = 0.3$, $a = 1.1\times10^{-4}\,cm$, $L = 3.7\times10^{-4}\,cm$, $\eta_\perp = \frac{4\pi\mu}{ln\left(\frac{2\lambda}{a_0}\right)-\frac{1}{2}} \approx 2.69\times10^{-2}\,g\cdot cm^{-1}\cdot s^{-1}$, $A \approx 0.08$, $B \approx 0.50$, $M \approx 8\pi\mu a^3 \approx 3.35\times10^{-13}\,g\cdot cm^2\cdot s^{-1}$, $Z = 6\pi\mu a \approx 2.07\times10^{-5}\,g\cdot s^{-1}$, and $C = A^2 - (1-B)\,A + \frac{1}{3}\,(1-B)^2 \approx 0.05$, I found that total energy consumption during flick process is around 10^{-11}-$10^{-12}\,erg$.

4.5.2 Calculation Based on the Off-Center Model

When the flagellum is at the cell pole, the energy dissipation rates for the cell body and for the flagellum are similar to the previous case given by Eqs. (4.28) and (4.29). The only difference here is that the velocities at the center of the cell and at the base of the flagellum are different. Denoting the translational and angular velocities of the cell-body center to be $\mathbf{V}_c$ and $\mathbf{\Omega}_c$ and that at the flagellar base to be $\mathbf{V}_\mathrm{o}$ and $\mathbf{\Omega}_\mathrm{o}$, the power dissipation by the cell body and by the flagellum are given respectively by,

$$\begin{aligned} P_b &= \mathbf{F}_b\cdot\mathbf{V}_c + \mathbf{N}_b\cdot\mathbf{\Omega}_c \\ &= Z\mathbf{V}_c^2 + \left(\mathbf{R}\times Z\mathbf{V}_c + M\mathbf{\Omega}_o\right)\mathbf{\Omega}_o \\ &= ZV_c^2 + Za\left(V_{cy}\Omega_{ox} - V_{cx}\Omega_{oy}\right) + M\Omega_o^2, \end{aligned}$$

$$P_f = \left(\zeta_\parallel \mathbf{V}_{ot}^2 + \zeta_\perp \mathbf{V}_{o\perp}^2\right)L + L^2\zeta_\perp \mathbf{v}_{fo}\cdot\mathbf{V}_{o\perp} + \frac{1}{3}L^3\zeta_\perp \mathbf{v}_{fo}^2.$$

In Fig. 4.18, the total energy dissipation $P = P_b + P_f$ in a flick following the path $\theta_0 = \frac{2}{3}\pi$ and $\phi_0 = 2\pi$ are plotted for both models. First of all we notice that numerical differences in P calculated by the two models are very small, much less than a factor of two for instance. We also notice that bacteria with a larger cell body to flagellum length ratios ($x \simeq 1$) consume more energy in a flick than those cells with a smaller cell body to flagellum length ratios ($x \ll 1$). For a cell with an unusually large cell body but a short flagellum, say $x \simeq 0.7$, the energy dissipation is about 6×10^{-10} erg. The energy dissipation is significantly reduced for a small x, indicating the importance of the flagellar length in effective flicking. Suppose a bacterium completes a flick in 60 ms, then the energy consumption power is estimated to be 1×10^{-15} W. According to the works of Sowa et. al [87], each force-generating subunit in *Vibrio alginolyticus* flagellar motor is estimated to produce at least 1.0×10^6 pN $\cdot$ nm/s, and one motor is estimated to have $5 \sim 8$ subunits. This yields $5 - 8 \times 10^{-15}$ W per motor, which is just about sufficient to drive the flick, suggesting that flagellar motor spends a significant amount of power to support flagellar off-axis rotation during a flick.

4.6 DISCUSSION

4.6.1 Bacteria of Large a/L Ratios Cannot Reorient with Large Angles

Fig. 4.19 shows a set of $\Psi\ (\theta_0,\ \phi_0)$ surfaces for different x values. We observed that within the model, the maximum angle, $\Psi \sim 180^o$, can be reached for $x = 0.24 - 0.26$, which corresponds to small bacteria of size $2a = 2xL = 1.78 - 1.92\,\mu$m. For increasing x, say $x = 0.45$, the peak angle Ψ decreases to 77^o. This means that the ability of bacteria to reorient decreases with its body size but increases with the flagellum length. Our calculation shows that a bacterium with $x > 0.42$ is unable to reorient with $\Psi > 90^o$ no matter what path Σ the flagellum follows. It is also manifested in Fig. 4.15(A), where the reorientation angle decrease as x increases.

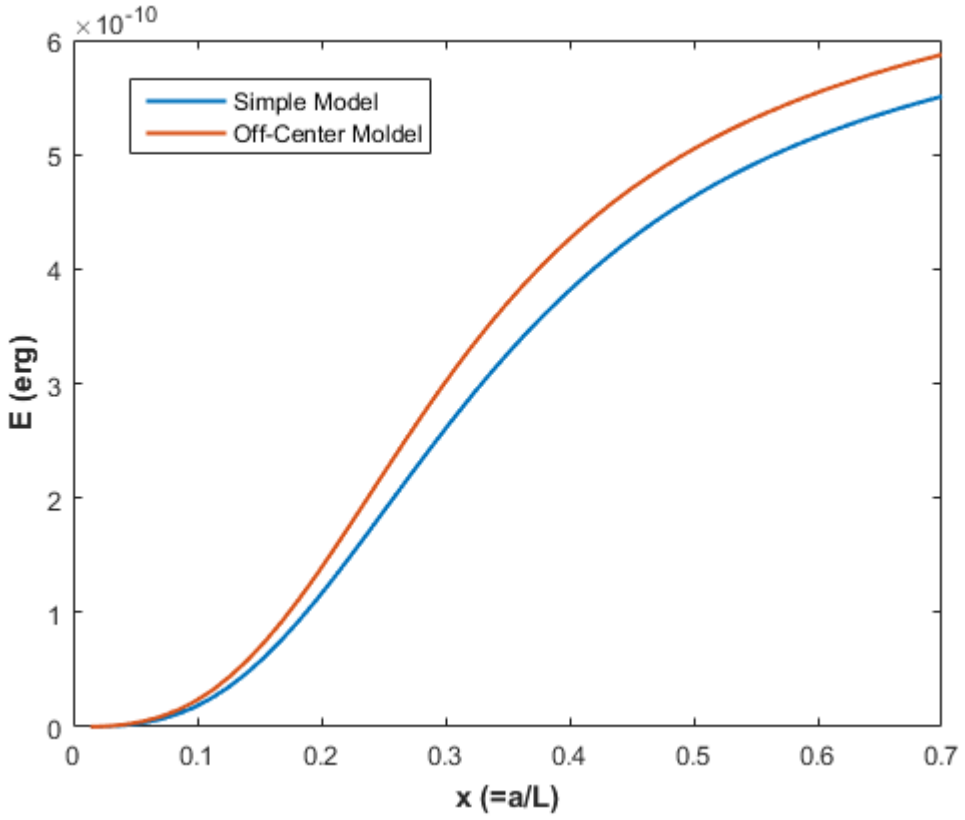

Figure 4.18: Energy Consumption Curve. The blue curve is for the simple model and the red curve is for the modified model. The following parameters are used in the calculation: $\theta_0 = \frac{2\pi}{3}$ and $\phi_0 = 2\pi$.

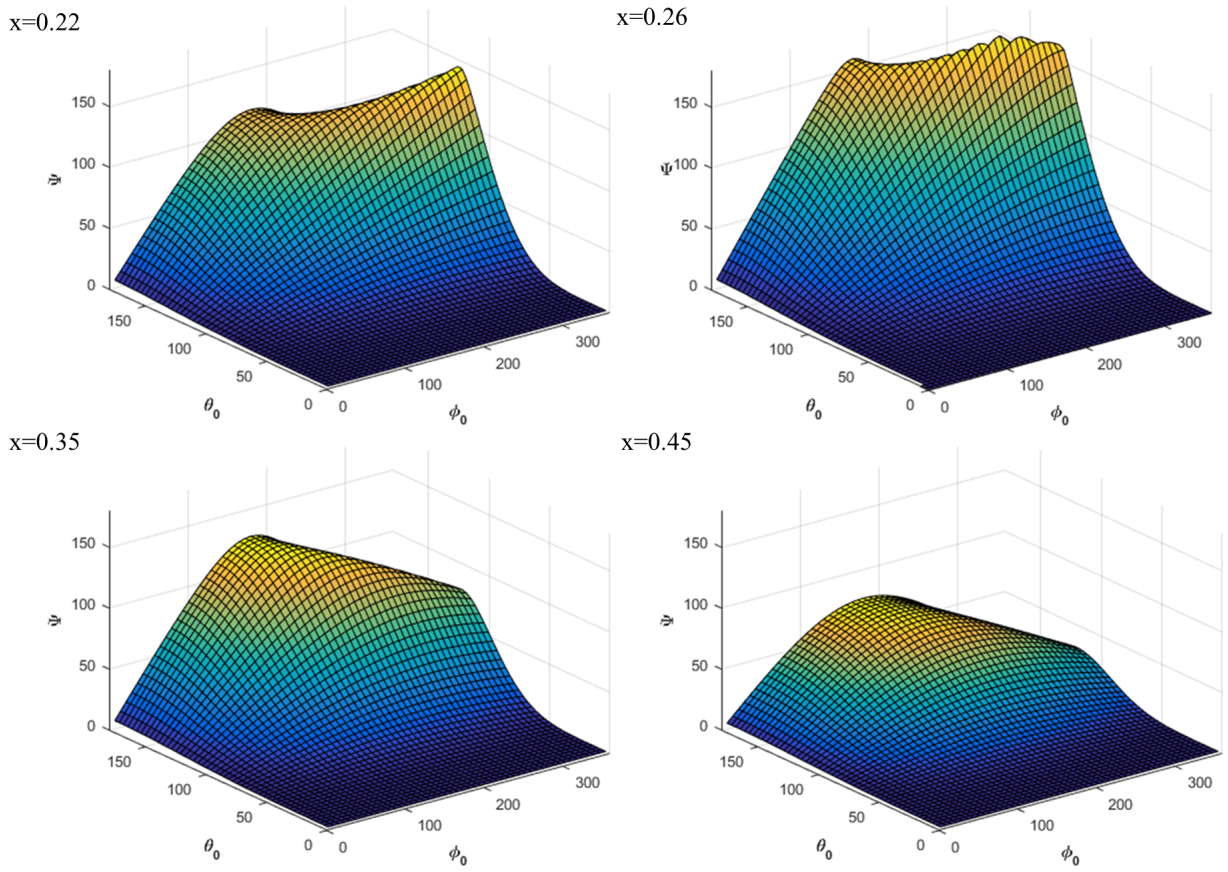

Figure 4.19: The Height of $\Psi(\theta_0, \phi_0)$ Surfaces Decrease with Increasing x.

4.7 CONCLUSION

In this chapter, I described a movement in *Vibrio alginolyticus*, in which bacterial cell body reorients by a π angle during a flick process. The flagellar off-axis rotation model introduced by Prof. Fu can predict cell body reorientation angles Ψ if the cell body and flagellum length ratio $x = a/L$, and the flagellar rotation path $\Sigma(\theta_0, \phi_0)$ is known. This model verified that small cells with size ratio x around $2.4 - 2.6$ are able to complete a $\Psi \approx \pi$ flick, and a cell's ability to reorient in large angles decreases with its size. Unexpectedly, the model fitting with experimental data suggests that cells in different size ranges more or less follow a similar flagellar rotation path, which is defined in Fig. 4.9 with parameters $\theta_0 \sim 113^o$ and $\phi_0 \sim 378^o$. This maneuver is feasible according to an observation in tethered cells, the flagella of which can easily finish a 120^o rotation in the polar direction. The power required to finish this movement is of the same order of magnitude as the flagellar motor output, suggesting that flagellar motors are able to power the flick process, but its capability to drive the cell body may decrease accordingly.

4.8 MATERIAL AND METHODS

Vibrio alginolyticus YM4 were firstly grown overnight in LBS (10 g/L Trypton, 5 g/L Yeast Extract, and 3.5 g/L NaCl). The overnight culture regrows in minimal medium (0.3 M NaCl, 10 mM KCl, 2mM K_2HPO_4, 0.01 mM $FeSO_4$, 15 mM $(NH_4)_2SO_4$, 5 mM $MgSO_4$, 1% [wt/vol] glycerol, and 50 mM Tris-HCl pH=7.5) after a 100 fold dilution, and was harvested when $O.D._{600}$ reaches 0.3. The harvested cells were washed twice in TMN medium(50 mM Tris-HCl pH=7.5, 5 mM $MgCl_2$, 5 mM glucose, 300 mM NaCl), and pipetted into a 1 mm thick chamber for microscopic observations.

For the fluorescence observations described in Fig. 4.4 and Fig. 4.16, bacteria were incubated in TMN buffer with 10% (v/v) NanoOrange (Invitrogen) for 15 min, before the washing step. In the tethered-cell experiment shown in Fig. 4.16, the stained and washed bacterial culture was spread on a poly-L-lysine coated coverslip before proceeding with microscopic

video recordings.

Video images were recorded by a Hamamatsu camera at 36 fps on Nikon TE300 microscope. All the trajectories were collected by ImageJ Mosaic module. A Matlab script was used to detect direction switching events (reverse and flick) and calculate the flick angles.

5.0 INTRACELLULAR CONCENTRATION OF CHEMOTAXIS REGULATOR CHEY AFFECTS THE STIFFNESS OF THE POLAR FLAGELLAR MOTOR OF *VIBRIO ALGINOLYTICUS*

5.1 INTRODUCTION

As described in Chapter 4, the cyclic 3-step (run-reverse-flick) motility pattern of *Vibrio alginolyticus* consists of distinctive features, forward (CCW) run is followed by a reversal (CW), and the new run is typically in a direction ∼90 degrees with respect to that of the previous runs (see Fig. 4.1(A)). In the course of investigating chemotactic behaviors of *cheY* deletion mutants of *V. alginolyticus* (LX1), we found that the ability of the mutant to randomize its swimming direction is noticeably compromised when the intracellular concentration of the regulator protein CheY ([CheY]) is high. The measurements showed that the flick angle decreases in an incremental fashion as [CheY] increases, suggesting that this randomization step may be internally regulated by the cell. We also performed measurements using *cheZ* deletion mutant (LX2) for which all CheY proteins in a cell are expected to be phosphorylated. In this mutant, the flick is suppressed relative to the wild-type cells, suggesting that perhaps it is not [CheY] per se but its phosphorylated form CheY − p that exerts an influence on the flicking behavior. While the details of how binding of CheY-p to the motor switching complex affects flicking is unclear at the moment, the general picture is that the motor complex as a whole becomes more stiff as [CheY − p] increases. It remains an intriguing possibility that the flexibility of the flagellar basal body in marine bacterium *V. alginolyticus* is subject to remodeling according to the environment. A rigid basal body allows the cell to execute the run-reverse motility pattern while a "loose" basal body allows the cell to flick upon resuming a forward run. Such plasticity may help the bacterium to

adapt to different environments, enhancing its fitness.

5.2 RESULTS

5.2.1 The Flicking Angle Distribution Depends on CheY Expression Levels

Our experiment was carried out using a *cheY* deletion mutant of YM4. The mutant is supplemented with a plasmid, pMMBYV, expressing CheY and YFP (Venus) from a lac promotor. The regulator gene *cheY* was subcloned from the chromosome of YM4, and its expression level is controlled by the inducer IPTG. In Material and Method (MM), we showed that Venus copy number in the cells follows closely the copy number of CheY despite the fact that different ribosome binding sites were used for *cheY* and *yfp*.

The regulator CheY protein conveys a chemical signal from the methyl-accepting chemotactic protein (MCP) clusters to the flagellar motor. In *E. coli*, CheY is phosphorylated by MCPs and the modified form, CheY-p, binds to the motor switch, the C-ring, enforcing the CW state. As a result, a higher-than-normal level of CheY-p causes the motor to run more frequently in the CW direction, increasing the CW bias or more tumbling. In the extreme case of very high [CheY-p], the motor run exclusively in the CW direction, the cell is in a perpetual state of tumbling. Marine bacterium *V. alginolyticus* can swim in both forward and backward directions with motor rotating in the CCW and CW directions, respectively. We recently found that the bacterium can also perform chemotaxis in both swimming directions as both swimming intervals are extended by an impulsive chemoattractant stimulation [88]. For this to be feasible it requires that the response of the motor to CheY-p binding is different in *V. alginolyticus* than in *E. coli*. Indeed it was observed that when [CheY] is elevated, and so is [CheY − p], the polar flagellar motor alters between CCW (forward) and CW (backward) directions more frequently. In other words it is the switching frequency rather than CW bias that is modulated by [CheY-p] in this bacterium. The dependence of motor switching frequency on [CheY] is delineated in Fig. 5.1. The altered regulation scheme observed in the polar flagellar motor illustrates the plasticity by which a microor-

ganism exploits to improve its fitness in a habitat.

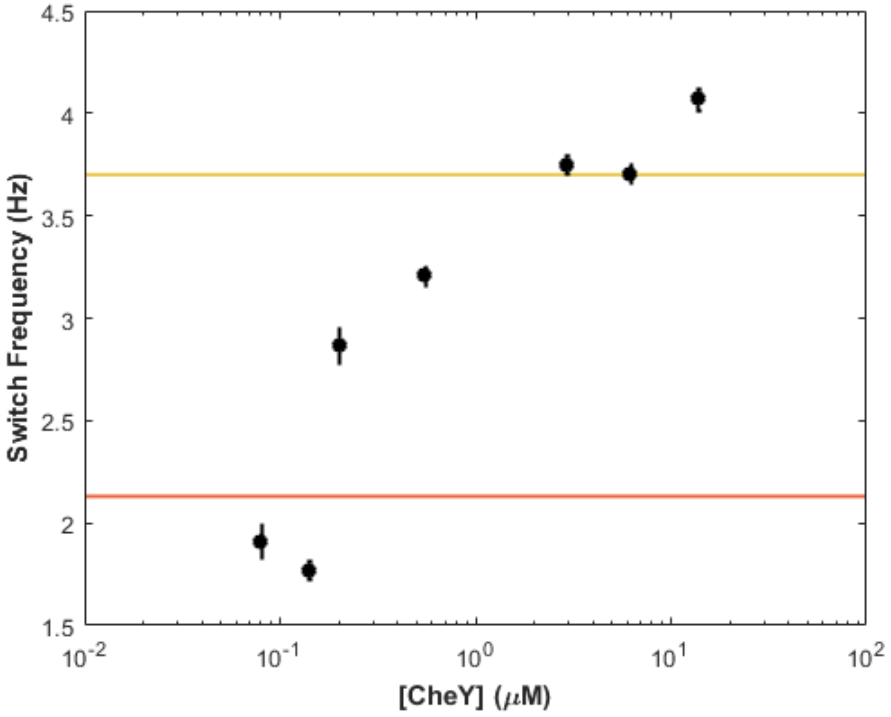

Figure 5.1: Motor Switching Frequency of *Vibrio alginolyticus* Increases with Intracellular [CheY]. Error bars are the standard error of the mean (SEM). A *cheY* mutant of YM4 carrying a *cheY* plasmid (pMMBYV) was induced to different [CheY] levels, and the motor switching rate was measured based on bacterial trajectories (see MM for experimental details). The red and yellow lines indicate switch frequencies of wt YM4 and LX2 (Δ*cheZ*).

Bacterial motility patterns for different [CheY] were studied in the motility buffer (TMN) under an inverted Nikon microscope (TE300). In the absence of IPTG, YM4 swim exclusively forward, and motor reversals were only observed when *cheY* gene was induced, even at a very low level. As displayed in Fig. 5.2, for induction with 0.3 μM IPTG, which corresponds to the optimal induction as judged by its motor reversal frequency being close to what is observed in wt cells (see Fig. 5.7). The bacteria swim by the cyclic 3-step (run-reverse-flick) motility patterns as shown in panel (A). However, for induction with 100 μM of IPTG, most of bacteria swim by cyclic 2-step (run-reverse) motility patterns as shown in panel (B). A very noticeable change in the motility pattern was observed when the IPTG induction level

was above a certain value, $\sim 10\,\mu$M. At this induction level, intracellular CheY concentration is [CheY] $\simeq 2.9\,\mu$M, which is ~ 50 times greater than the steady state concentration in wt *V. alginolyticus* (unpublished data) and is comparable to the CheY concentrations in *E. coli*, which has many motors [89].

Motivated by Son et al.'s work, we reasoned that since buckling instability is strongly affected by the length L of the hook, perhaps CheY over-expression may affect the length L and reduces the cell's ability to flick. Although it has not been reported to our knowledge, such a scenario cannot be ruled out based on the genetic analysis of *V. parahaemolyticus*, a close cousin of *V. alginolyticus*, by Kim and McCarter [90]. Their study showed that the major set of chemotaxis genes (*cheYZARW*) is organized on the same regulon of the structural genes (*fliM*, *fliN*, *fliG*, etc.), the assembly genes (*fliHIJOPQR*, and the flagellar genes *(flhBA*) of the polar flagellar system. Since the export apparatus is located inside the C-ring, consisting of FliM, FliN. and FliG, and since FliM/FliN interact with CheY, overexpression of CheY may affect the transport of FlgE, the component of the hook, in the early stage of assembly, rendering the cell unable to flick. To see whether this is the case we purified the bacterial basal body (see MM) and examined them using transmission electron microscopy [91]. Fig. 5.3 shows the histograms of the hook length L for YM4 and $\Delta cheY$ mutant LX1 that has been maximally induced, [IPTG] $= 100\,\mu$M. Based on ~ 200 basal bodies examined, we found that the average hook length and diameter for YM4 to be $\bar{L} = 97 \pm 11\,$nm and $\bar{D} = 20 \pm 3\,$nm, and the corresponding quantities for the mutant to be $\bar{L} = 92 \pm 11\,$nm and $\bar{D} = 20 \pm 2\,$nm. The small shift in the hook length is well within the statistical uncertainty of our measurements and likely not the cause that leads to the changes in the motility patterns delineated in Fig. 5.2.

For a quantitative characterization of direction randomization, many bacterial tracks were collected for each IPTG induction level and their flick angles θ were measured (see flick angle definition in Chapter 4, Fig. 4.1). Since the ability of a cell to flick depends on its speed and size [86, 19], only those cells that swim at high speed, $v_{sm} \geq 50\,\mu$m/s, and with a small cell-body length, $2a \leq 3\,\mu$m, were used for analysis. Fig. 5.4 displays probability density functions of θ for different induction levels, [IPTG] $= 0$, 0.3, 1, 3, 10, 30, and $100\,\mu$M. The bacterial swim speed v_{sm} and the cell size $2a$ histograms are shown in Appendix H. It is

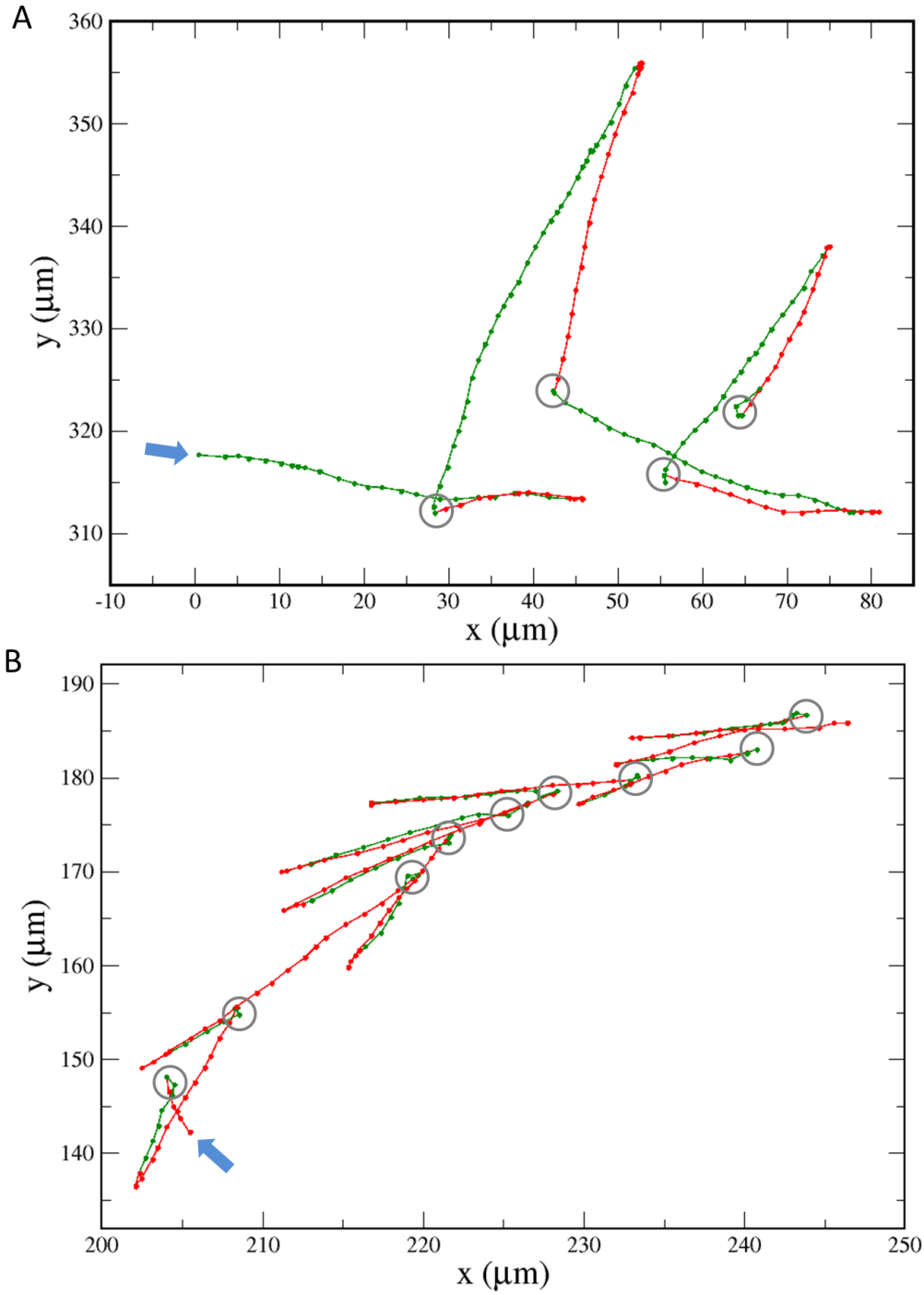

Figure 5.2: Swimming Trajectories of Strain LX1 Induced with 0.3 μM (A) and 100 μM (B) IPTG. At a low induction level, the trajectory is very similar to those seen in wild type *V. alginolyticus*. The forward and backward intervals are labeled in green and red respectively. The flicking processes, which happen at backward to forward swimming transitions, are labeled with gray circles. Blue arrow shows where each trajectory starts.

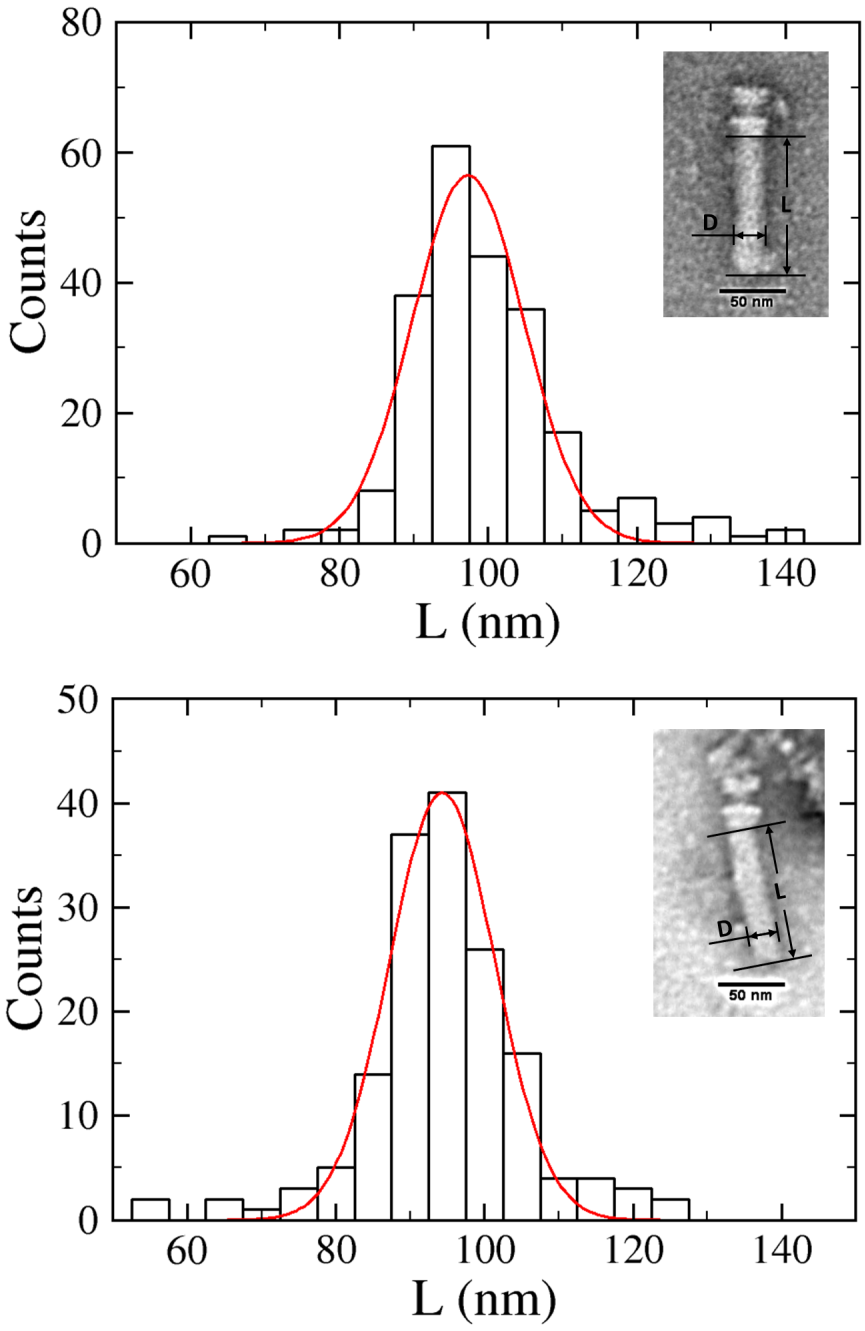

Figure 5.3: Hook Length Measurements. The hook length histograms for wt YM4 and LX1 ($\Delta cheY$, pMMBYV) are displayed in (A) and (B), respectively. The mutant carries the plasmid pMMBYV and the CheY expression was induced by 100 μM of IPTG. The inserts show the basal body structure for the two strains, where hook length L and diameter D are delineated.

seen that at low induction levels (see Fig. 5.4(C-E)), $P(\theta)$ is nearly identical to that of wt cells (see Fig. 5.4(A)) and is peaked at $50^o \sim 100^o$. However, the distribution becomes more and more skewed towards the large angles, $\theta \simeq \pi$, as the induction level increases (see Fig. 5.4F-I). Observations under the microscope showed that increasing number of cells lost their ability to flick, i.e., some never flick and other flick less frequently as [IPTG] is increased.

A convenient means to characterize these distribution functions is to plot the first few moments as delineated in Fig. 5.5. Here I found that as [CheY] increases, the mean flicking angle $\bar{\theta}$ increases in a logarithmic fashion (A), while the second moment, $\overline{(\theta-\bar{\theta})^2}$ slightly increases at low [CheY] and then levels off at high concentrations (B). The (a)symmetry of the distributions is characterized by skewness, a normalized third moment $\frac{\overline{(\theta-\bar{\theta})^3}}{\sigma^3}$. The skewness in our measurement is positive (biased towards small flicking angles $\theta \to 0$) for low [CheY] and negative (biased towards large flicking angles $\theta \to \pi$) for high [CheY]. This is delineated in Fig. 5.5(C). Finally, the normalized fourth moment $\frac{\overline{(\theta-\bar{\theta})^4}}{\sigma^4}$ or the Kurtosis is a measurement of whether or not a distribution is heavy-tailed relative to a normal distribution. Normal distribution has a Kurtosis of 3 whereas my flick angle distributions yields $\frac{\overline{(\theta-\bar{\theta})^4}}{\sigma^4} \simeq 2.1$, suggesting that most flick angles are centered around $\bar{\theta}$ with a lighter tail compared to the normal distribution.

5.2.2 The Δ*cheZ* Mutant Has the Same Flicking Angle Distribution as CheY Overexpression

Using the same bacterial conjugation technique, we also created a *cheZ* deletion mutant (LX2) that switches back and forth between CCW and CW rotations at a high rate. Based on its motor switching rate, we found that the pool size of CheY-p is comparable to when CheY is overexpressed at [CheY] $\simeq 2.7\,\mu$M (see Fig. 5.1). Fig. 5.4(B) displays the flicking angle PDF for this mutant strain, showing significant similarity with those in Fig. 5.4F and G when [CheY] is $3-20$ fold of that in wt YM4 ($\sim 0.14\,\mu$M). The mean and skewness of LX2 are $\bar{\theta} = 99^o \pm 46^o$, and $\frac{\overline{(\theta-\bar{\theta})^3}}{\sigma^3} = -0.05 \pm 0.22$ as shown in Fig. 5.5(A) and (C). The slight skewness in Δ*cheZ* mutant is quite different from that observed in wt YM4 and comparable to $3\,\mu$M IPTG induction as shown in Fig. 5.4F.

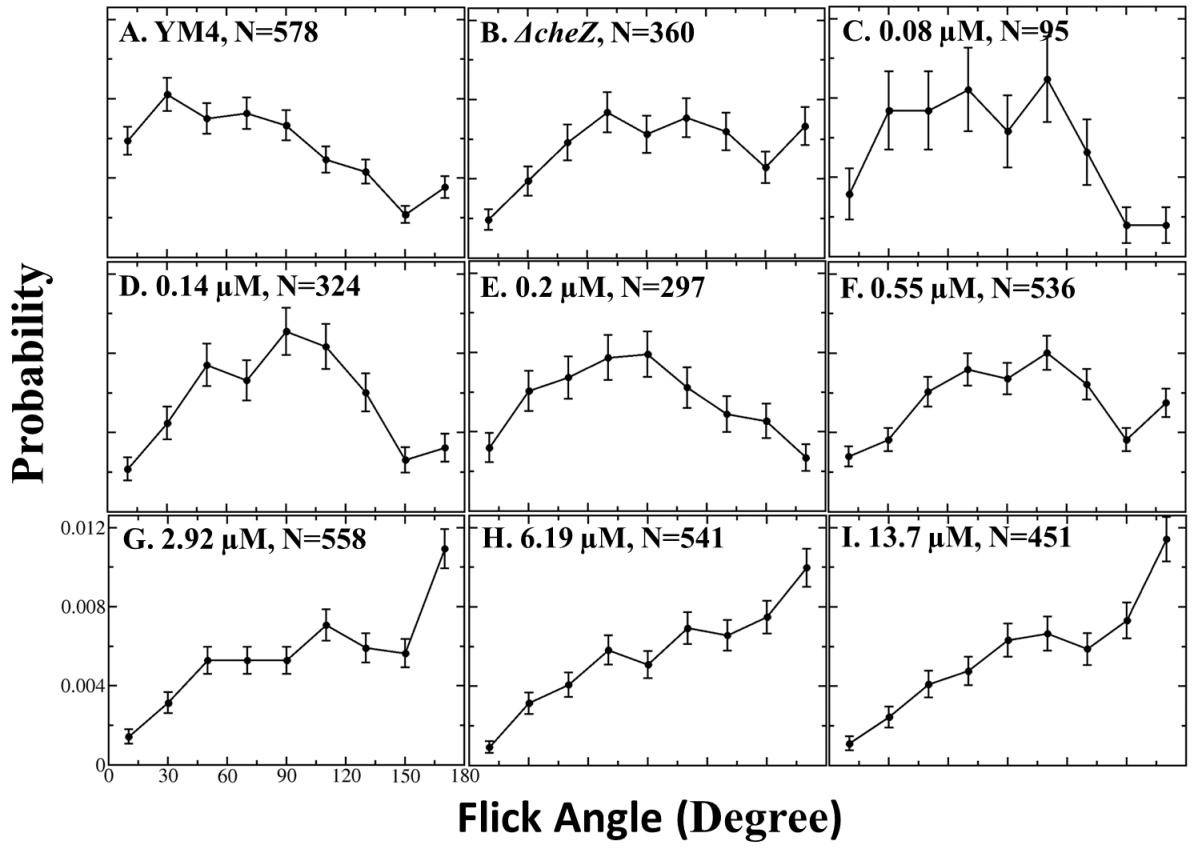

Figure 5.4: Flicking Angle PDFs of YM4 (A), LX2 (Δ*cheZ*) (B), and LX1 (Δ*cheY*, *pMMBYV*) (C - I) with varying concentrations of CheY. The CheY was induced in LX1 by 0, 0.3, 3, 10, 30, and 100 μM of IPTG. The population size (N) is labeled in each plot.

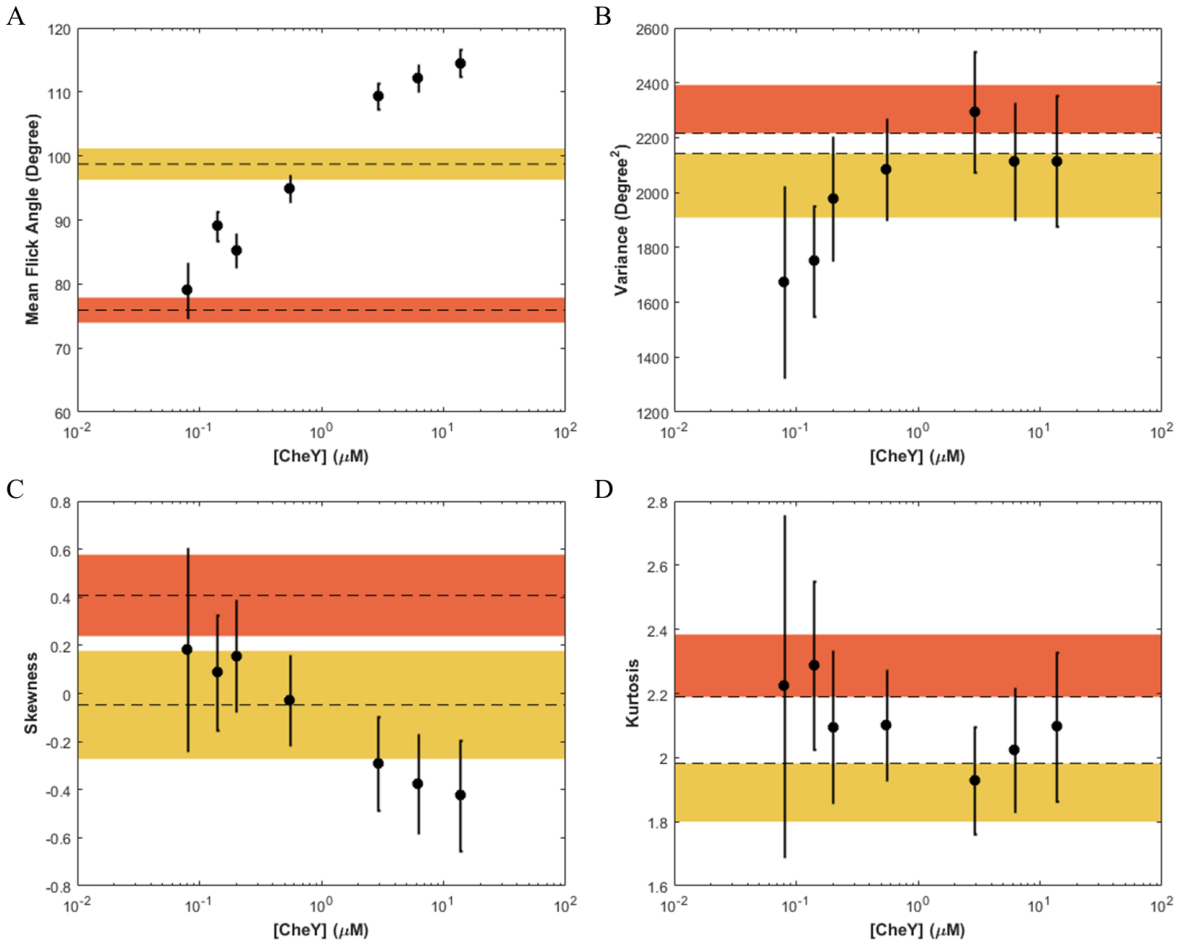

Figure 5.5: Moments of Flicking Angle Distributions. The mean flick angle (A), variance (B), skewness (C), or kurtosis (D) of flick angle distributions in Fig. 5.4 are plotted against the corresponding CheY concentrations. Error bars are standard errors of the mean. Data from wt YM4 and its Δ*cheZ* mutant LX2 are plotted in dashed lines. The orange and yellow bands represent for their uncertainties. Only one side of the error bounds in plot (B) and (D) are shown, since YM4 and LX2 data overlap in these two plots.

We considered the observation of Δ*cheZ* mutant LX2 to be significance. In the hook length measurement reported above, even though one can rule out the possibility that hook length is unaffected by over-expression of CheY, but one cannot rule out other anomalies in the motor and flagellar assembly. The observation in Fig. 5.4(B) for LX2 suggests that CheY overexpression per se is not the cause for the bacterium to lose its flicking ability but rather it is the elevated [CheY-p] that is responsible for the phenotype. So, binding of the protein to the motor is importatnt.

5.3 MODEL FITTING

Using flagellar off-axis rotation model developed in the previous chapter, the polar and azimuthal angles (θ_0, ϕ_0) of flagellar path Σ (shown in Fig. 4.9 in Chapter 4) are extracted from LX1 cell-body reorientation angle data (see Fig. 5.6). The polar angles θ_0 decrease continuously with the increased [IPTG], while the azimuthal angle ϕ_0 increases slightly. Overall, the surface area enclosed in the path Σ decreases with [IPTG]. As discussed in section 5.2.2, IPTG elevates [CheY-p], suggesting that flagellar swiping amplitude during a flick decreases with increased CheY-P concentration.

5.4 CONCLUSION

Taking together all of our observations, an inescapable conclusion is that the ability for *V. alginolyticus* to flick cannot depend solely on the mechanical properties of the flagellar hook. Since only CheY-p can bind to the motor complex and since it is unlikely that increasing a few or several CheY-p on the ring would change the elastic property of the motor complex, we posit that the motor itself undergoes remodeling for different amount of CheY-p binding. The idea that flagellar motor undergoes remodeling is not totally new, and has been observed for different motor components [92, 93, 94]. The general consensus is that some of the motor components may be worn over time and need to be replaced by new ones from time to

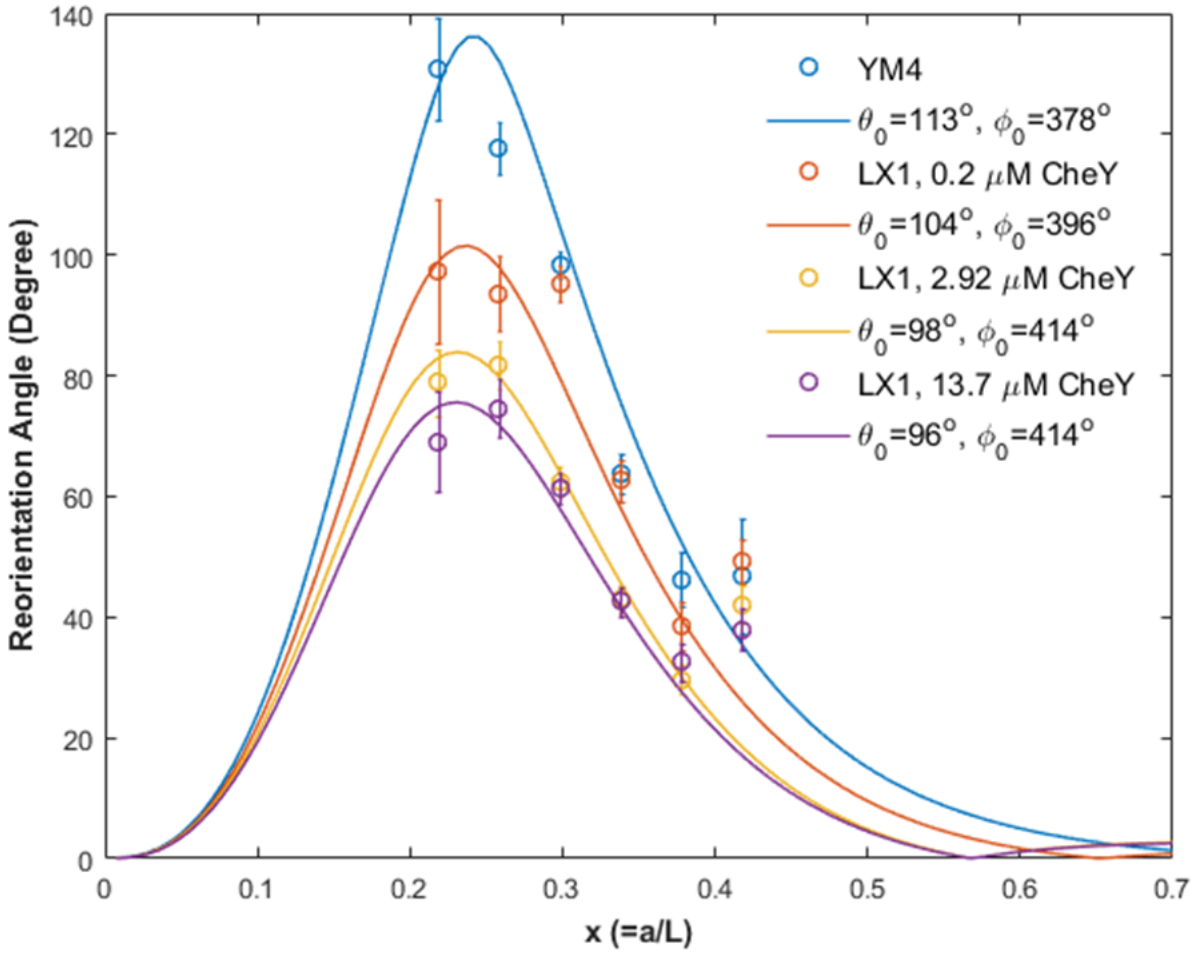

Figure 5.6: Model Fitting for LX1 Flick Angles. Open circles are data for cell-body reorientation angles $\Psi(x)$ of LX1 induced with varying concentrations of IPTG. Error bars are standard error of the mean. The curves represent the best fits according to the model.

time. A more novel idea is that remodeling is a means of adaptation. Yuan et al. observed that the number of FliM on the c-ring is not constant but adjusts itself according to the intracellular CheY-P concentration; e.g. adding strong attractant, which decreases [CheY-p], the number of FliM changes from 34 to 42 [95]. The remodeling or adaptation time for the motor complex is about a minute or so, much longer than the typical chemotaxis response time, which is only a few seconds. This adaptation mechanism, which takes place at the output of the chemotaxis signaling pathway, also enables cells, which have very different intracellular [CheY-p] to perform chemotaxis over a very narrow operating range [95].

Although we do not know how the polar flagellar motor remodels when [CheY-p] changes inside a cell, it is reasonable to assume that such remodeling alters the elastic moduli of the motor complex, and which in turn modulates the flicking probability as seen in our experiment. We note that polar flagellar motor of *V. alginolyticus* appears to be a more elaborated assembly of components than the *E. coli* counterparts. It contains all the essential parts of *E. coli*'s motor with some important additions. For instance, apart from PomA and PomB, which are equivalents to the stator components MotA and MotB in *E. coli*, *V. alginolyticus* also possesses additional stator components MotX and MotY. *V. alginolyticus* also possesses an H-ring which surrounds the L-P ring, and a T-ring which serves as a docking station for the MotX/MotY complex. The current consensus is that these additional features are for structural re-enforcement since the polar flagellar motor rotates at a much faster speed than *E. coli* cells. However, their functionality in relation to the the flicking phenomenon remains to be investigated.

While it is unclear about the biological implication of why *V. alginolyticus* reduces its flicking probability in proportion to the intracellular [CheY-p], cases can be made to show that such behavior can be advantageous under certain conditions. Suppose that the bacteria are localized near a nutrient distribution, which may be spatially extended, such as striations created by turbulent fluid flows, or spatially localized like a point source in a quiescent fluid. The small spatial extent requires the cells to switch the swimming direction more frequently. Cell localization can be significantly enhanced, if the flicking probability is low. This leads us to speculate that flicking is mostly helpful when a cell is in the search mode, when individual swimming intervals are long. But once the cell becomes localized, an elevated

CheY-P gradually causes the cell to abolish its flick motion and become more localized.

5.5 MATERIALS AND METHODS

5.5.1 Bacterial Cultures

All measurements conducted herein used the *V. alginolyticus* strain YM4 and its *cheY* and *cheZ* deletion mutants created by a conjugation technique (unpublished material). The cheY is complemented on a plasmid pMMBYV and the expression level is controlled by IPTG. Downstream of *cheY* is a reporter gene *venus* that allows [CheY] to be measured quantitatively at different [IPTG].

The bacteria were grown in the minimal medium (0.3 M NaCl, 10 mM KCl, 2mM K_2HPO_4, 0.01 mM $FeSO_4$, 15 mM $(NH_4)_2SO_4$, 5 mM $MgSO_4$, 1% [wt/vol] glycerol, and 50 mM Tris-HCl pH=7.5) supplemented with 25 μg/ml chloramphenicol. The growth was taking place at 30 ^{o}C and shaken vigorously at 200 rpm. For CheY induction, the cells were grown to $OD_{600} = 0.1$ and varying amount of IPTG were added to the growth medium, and further incubated for 3 hrs. The OD_{600} at this point is ~ 0.2. The cells were washed using the motility buffer TMN (50 mM Tris-HCl pH=7.5, 5 mM $MgCl_2$, 5 mM glucose, 300 mM NaCl) once and resuspended in TMN for at lest 30 min before measurements.

5.5.2 Mutagenesis Using Bacteiral Conjugation

Using a bacterial conjugation technique, we created a *cheY* deletion mutant of YM4 that swims exclusively in the forward direction when grow in a liquid medium, TMN buffer. We restored the function of CheY by introducing a plasmid, pMMBYV, into the mutant. The regulator gene *cheY* was subcloned from the chromosome of YM4, and its expression level is controlled by the inducer IPTG concentratoin. Directly behind cheY is a yellow fluorescent protein (*yfp*) gene, known as venus, which transcribes along with cheY but has its own ribonsome binding site. latter allows the expression level of YM4 to be characterized.

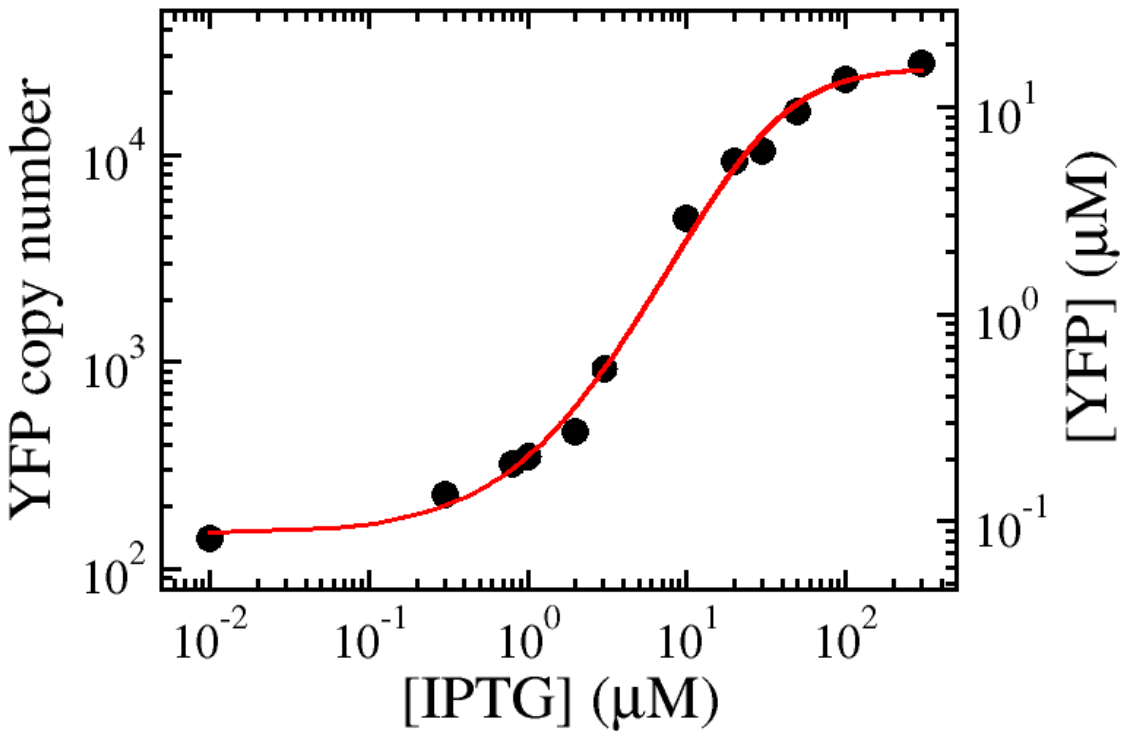

Figure 5.7: Intracellular CheY Concentration Calibration Curve. The sigmoidal curve represents CheY copy number or intracellular concentration [CheY] as a function of [IPTG]. Here the average volume of YM4, based on our measurements, is $2.82\,\mu\text{m}^3$.

5.5.3 Polar Flagellar Basal Body Purification

Vibrio alginolyticus hook purification were adapted from a protocol in Hosogi (2011) [17]. YM4 and LX1 ($\Delta cheZ$, pMMBYV) were grown with shaking overnight in VC medium (0.5% [wt/vol] tryptone, 0.5% [wt/vol] yeast extract, 0.2% [wt/vol] Glucose, 3% [wt/vol] NaCl, 0.4% [wt/vol] K_2HPO_4) and VC supplemented with 25 μg/ml chloramphenicol respectively at 30^oC. Cells were re-innoculated in 500 ml minimal medium (0.3 M NaCl, 10 mM KCl, 2mM K_2HPO_4, 0.01 mM $FeSO_4$, 15 mM $(NH_4)_2SO_4$, 5 mM $MgSO_4$, 1% [wt/vol] glycerol, and 50 mM Tris-HCl pH=7.5) with a 1:100 dilution, and grew at 30°C to $O.D._{600}$ = 0.45. Cells were harvested by centrifuging at 2000 × g for 15 min. The pellets were resuspended in 100 ml sucrose solution (0.5 M sucrose, 50 mM Tris–HCl at pH 8.0) at 4^oC, and turned into spheroplastic shape by adding EDTA pH=8.0 and lysozyme to a final concentration of 2 mM and 0.1 mg/ml respectively and incubated at 37^oC for 10 min. The spheroplasts were lysed by adding Triton X-100 to a final concentration of 1%. To reduce lysate viscosity, DNase and $MgSO_4$ were added to final concentrations of 0.1 mg/ml, and 10 mM, and incubated in 37°C for10 min. After the viscosity of the solution decreases, EDTA was added to a final concentration of 10 mM. Cell debris and unlysed cells were removed by centrifugation at 10, 000 × g for 20 min. Polyethylene glycol 6000 and NaCl, were added to the lysate to final concentrations of 2% and 100 mM, respectively. The samples were then incubated at 4 °C for 60 min, and centrifuged at 1, 000 × g for 15 min to get rid of cell debris. The supernatant was further centrifuged at 100, 000 × g for 30 min, and the pellet was resuspended in TET buffer (10 mM Tris–HCl at pH 8.0, 5 mM EDTA, 0.1% (w/v) Triton X-100). To remove cell debris, the supernatant was centrifuged at 1, 000 × g for 15 min. Then, the supernatant was centrifuged at 100, 000 × g for 30 min, and the pellet was resuspended in 400 μl TET buffer. To dissove flagellin, the sample was diluted 30 fold in Glysine-HCl (pH=3.3) containing 0.1% Triton X-100, and was incubated with shaking at room temperature for 1 hr. After that, it was centrifuged at 150, 000 × g for 30 min at 4°C, and the pellet was suspended in250 μL TET buffer. Finally, the sample was centrifuged at 10, 000 × g for 5 min, and the hook-basal body complex is in the supernatant collected.

5.5.4 Calibration of CheY Concentrations Using Single Molecular Fluorescence

See Appendix D, for the fluorescence intensity calibration of a single Venus protein.

After the brightness of each chimeric protein is established, we next measured the average brightness of YM4 induced by different [IPTG]. This yields the final calibration curve that is displayed in Fig. 5.7. The curve is sigmoid when plotted in a log-log plot with the steepest slope occurring at $[\mathrm{CheY}]_0 \simeq 0.3\,\mu\mathrm{M}$, which corresponds to the physiological concentration of CheY as judged by the frequency of motor reversals. Thus over the span of the induction levels, $10^{-2} \leq [\mathrm{IPTG}] < 10^{3}\,\mu\mathrm{M}$, [CheY] varies by nearly two orders of magnitude, from ˜130 copies to ˜13000 copies.

5.5.5 Recording and Analyzing Bacterial Trajectories

Bacterial swimming were imaged using Nikon TE-300 inverted microscope in the phase contrast mode and recorded in 36 fps on the Hamamatsu camera. A medium magnification lens, 20× and NA=0.45, was used. Individual bacterial trajectories were constructed using ImageJ with the plugin module Mosaic. Detailed information, such as the cell size, the swimming speed, and the flicking angle, can be deduced for each cell by post processing using a Matlab program. Some typical bacterial tracks are displayed in Fig. 5.2.

APPENDIX A

STRAIN TABLE

Table A1: Bacteria Strains used in the thesis.

Strain	Genotype
MG1655	*F-*, *λ-*, *rph-1*
LE392	*F-*, *Δ(codB-lacI)3*, *glnX44(AS)*, *galK2(Oc)*, *galT22*, *λ⁻*, *tyrT58(AS)*, *metB1*, *hsdR514*, *trpR55*
JH1	Derived from LE392, *lamB::venus*
SX4	Derived from BW25993, *lacZ::tsr-venus [33]*
YM4	Derived from 138-2 , Pof^+, laf^-[96]
LX1	Derived from YM4, Δ*cheY*, pMMBYV
LX2	Derived from YM4, Δ*cheZ*
LX3	Derived from YM4, Δ*cheY*, pfMMBYV

APPENDIX B

THE CONSTRUCTION OF STRAIN JH1

Competent Cell Preparation: Using the method described in Detsenko et al. (2000) [34], plasmid pKD46 was transformed into LE392 to confer the λ-red recombination competency. The transformant was grown in 50 ml SOB or LB rich media with ampicillin (50 μg/ml) and L-arabinose at 30°C to $OD_{600} \approx 0.6$. These induced midlog cells were made electrocompetent by washing three times with ice-cold 10% glycerol, and concentrated ¿100 fold in the last step.

Insert Amplification: *venus* gene was inserted into plasmid pKD13 on the 5' end of a curable kan^R gene. Two $\sim$ 75 bp primers (P1 and P2 as shown below) were used to amplify the *venus-*cm^R region. Each of the primers has a 50 bp chromosome homologous fragment on the 5' end. The PCR product was treated with *Dpn*I and gel purified.

P1: GTTGGTTGCCGAATGCGGCGTAAACGCCTTATCCGGCCCAGGTTTTGCT AGTGTAGGCTGGAGCTGCTTC

P2: TGGACCTTCGGTGCCCAGATGGAAATCTGGTGGTAA ATTAAAGAGGAGA TAGAATGAGTAAAGGAGAAGAACT

Electroporation: $10 - 100$ ng of the purified insert DNA was mixed with 50 μl LE392 (pKD46) competent cells, transferred to a *E. coli* Pulser cuvette with 0.2 cm electrode gap, and incubated on ice for $\sim$ 30 min. The electroporation was done on BioRad MicroPulser. Immediately after the shock, 1 ml of 37°C SOC medium was added into the cuvette. The culture was then transferred into a tube, and incubated at 37°C for 1 hr with sufficient aeration.

Selection: After 1 hr incubation, half of the culture was spreaded on a LB agar plate for chloramphenicol resistence selection at 37°C. If colonies show up in the next $15 - 20$ hr, they are picked, and incubated in LB medium without antibiotic at 37°C. They are colony purified at 37°C and tested ampicillin sensitivity to test for the loss of plasmid pKD46. If it was not lost, they are colony purified at 43°C and tested again.

To eliminate antibiotic resistance gene, plasmid pCP20 is transformed into the selected mutant, and selected for ampicillin resistance at 30°C. Since pCP20 is temperature sensitive, the selected colonies were purified once nonselectively at 43°C, and then tested for loss of all antibiotic resistance.

APPENDIX C

LIVE CELL IMAGING

The Venus or CheY copy number in Chapter 2 and Chapter 5 was measured as described below.

The harvested midlog bacteria were washed twice in 0.85% NaCl solution, and then tethered onto Poly-L-Lysine coated coverslips. The coverslip was assembled into a chamber, and then observed under a fluorescence microscope as described in Appendix D.

As shown in Fig. C1, for each field of view, a phase contrast image (A) was taken to set the cell boundaries, and a fluorescence image (B) were taken to collect its fluorescence. To eliminate dead cells as described in Chapter 2, an additional image in the red channel was taken to screen out dead cells labeled by propidium iodide. A phase contrast-fluorescence overlay picture is shown in (D).

Firstly, cell contours were identified in image (A), out of which cells with connected boundaries were excluded. Then the pixel intensities in image (B) enclosed in cell contours were averaged, and converted into Venus copy numbers per pixel using a converted single Venus intensity from Appendix D. This value reflects the protein concentration inside a cell in Chapter 2 and it is independent of cell size.

The mean pixel protein copy number times mean area generates the protein copy number inside a cell. This value will be used in Appendix G.

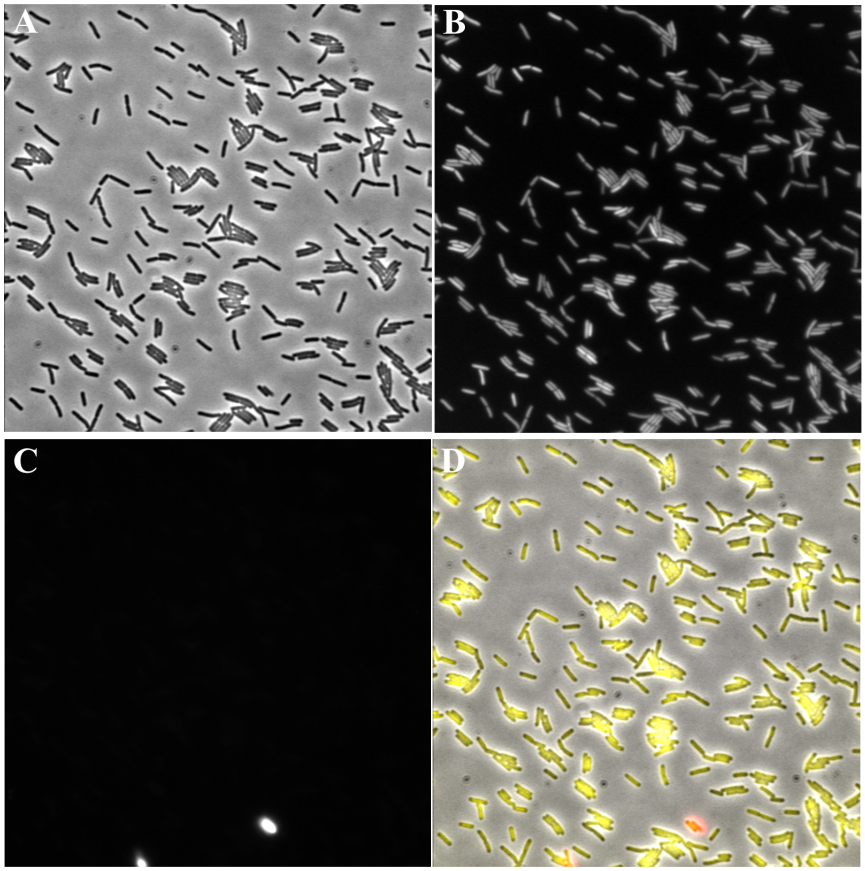

Figure C1: Live Imaging of Fluorescent Cells. (A) the phase contrast image, (B) the fluorescence image in the yellow channel ($\lambda_{ex} = 500 \pm 20\,\text{nm}$, $\lambda_{em} = 545 \pm 20\,\text{nm}$), (C) the fluorescence image in the red channel (a propidium iodide test), and (D) image overlay.

APPENDIX D

VENUS FLUORESCENCE CALIBRATION

Strain SX4 (gift from Prof. Sunney Xie [33]), which has a single copy of chimeric gene *tsr-venus* incorporated on the *E. coli* chromosome replacing the native *lacZ* gene, was used to calibrate single venus brightness.

After overnight in M9 (4% glucose) medium at 37°C, cells were reinoculated into fresh (1:100 dilution) M9 (glucose) medium, and harvested at $\text{O.D.}_{600} = 0.2$. The harvested cells were washed twice in 0.85% NaCl solution, spread on a 18× 18 mm poly-L-lysine (Sigma) coated coverslip, incubated for 15 min, and then assembled into a chamber for microscopic observation. The measurements were carried out using an inverted Nikon (TE350) microscope equipped with a back-thinned charge intensified CCD camera (Hamamatsu C9100). The light source is a 75W mercury arc lamp, and fluorescent cube consists of the excitation filter $\lambda_{ex} = 500 \pm 20\,\text{nm}$, the emission filter $\lambda_{em} = 545 \pm 20\,\text{nm}$, and a dichroic mirror (Q515lp, Chroma). An oil immersion lens, 100× and NA=1.35, was used for imaging. To ensure consistency between different runs, a small number of fluorescent beads, diam= $2.5\,\mu\text{m}$, was used as standard. Photobleaching videos were taken at 2 fps.

Fluorescent puncta were manually detected as 3×3 pixel matrices. After background subtraction, pixel intensity were summed up, and plotted as a function of time as shown in Fig. D1. Most of times they decrease in a stepwise fashion. An abrupt fluorescence jump in the curve is considered to be a bleaching event of a single Venus protein. Over 50 bleaching events were measured, yielding an averaged step size (single venus fluorescence intensity) to be 500 ± 20 A.U.

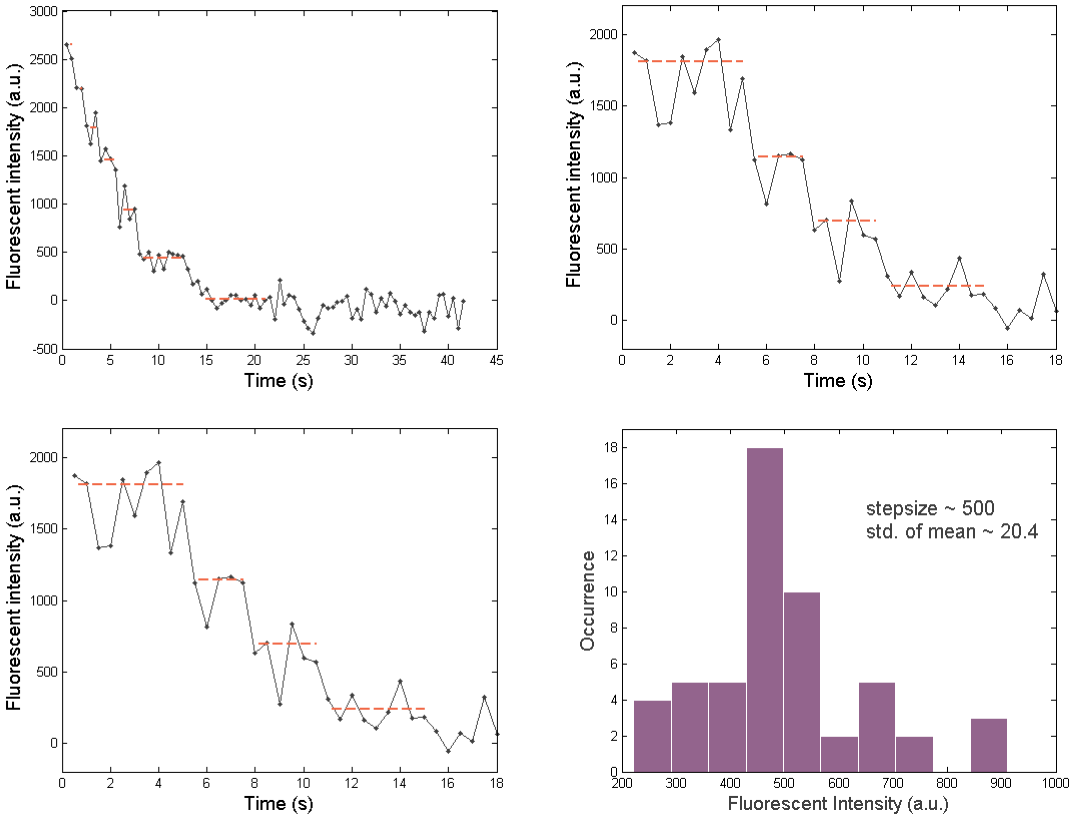

Figure D1: Tsr-Venus Cluster Stepwise Fluorescence Decay Curves.

APPENDIX E

POSITIVE REGULATION LOOP IN MALTOSE REGULON

Maltose regulon involves 10 genes on 5 operons, out of which four (*malP*, *malQ*, *malZ*, and *malS*) encode enzymes for maltodextrin metabolism, five (*malK, malF, malG, malE,* and *lamB*) encode for transport proteins, and another gene *malM* encodes a periplasmic protein MalM with unspecific functions (see Fig. E4). All the *mal* operons are activated by MalT protein, the expression of which is controlled by catabolite activator protein (CAP) and a repressor Mlc.

When glucose is available (as shown in Fig. E1), catabolite repression keeps cAMP concentration low and CAP are mostly inactive inside the cell, which inhibits *mal* , *lac*, *ara* operons, inluding gene *malT*; Mlc, on the other hand, is sequestrated by enzyme IICB during glucose transport through the PTS pathway, which relieves the repression on *malT* operon. It's unclear whether there is any residual expression of MalT under this condition.

When there's no maltodextrin transport (as shown in Fig. E2), MalT can be sequested by MalK on the maltodextrin ABC transport pathway, or alternatively interact with negative effectors MalY or Aes. Maltotriose and ATP inducers MalT from its resting (inactive) form to an active form. Maltotriose could be generated from glycogen degradation which requires MalP or synthesis from maltose by MalQ. Active MalT self-associates into polydisperse homopolymers. An increase in active MalT concentration enhances the expression of *mal* genes, which translate into maltose transport proteins (LamB and MalEFGK), and maltotriose synthesis enzymes (MalPQ). Those proteins further enhance the fraction of active MalT protein, forming a positive feedback loop.

The nonlinearity comes from the cooperative binding of MalT homopolymers on the MalT boxes.

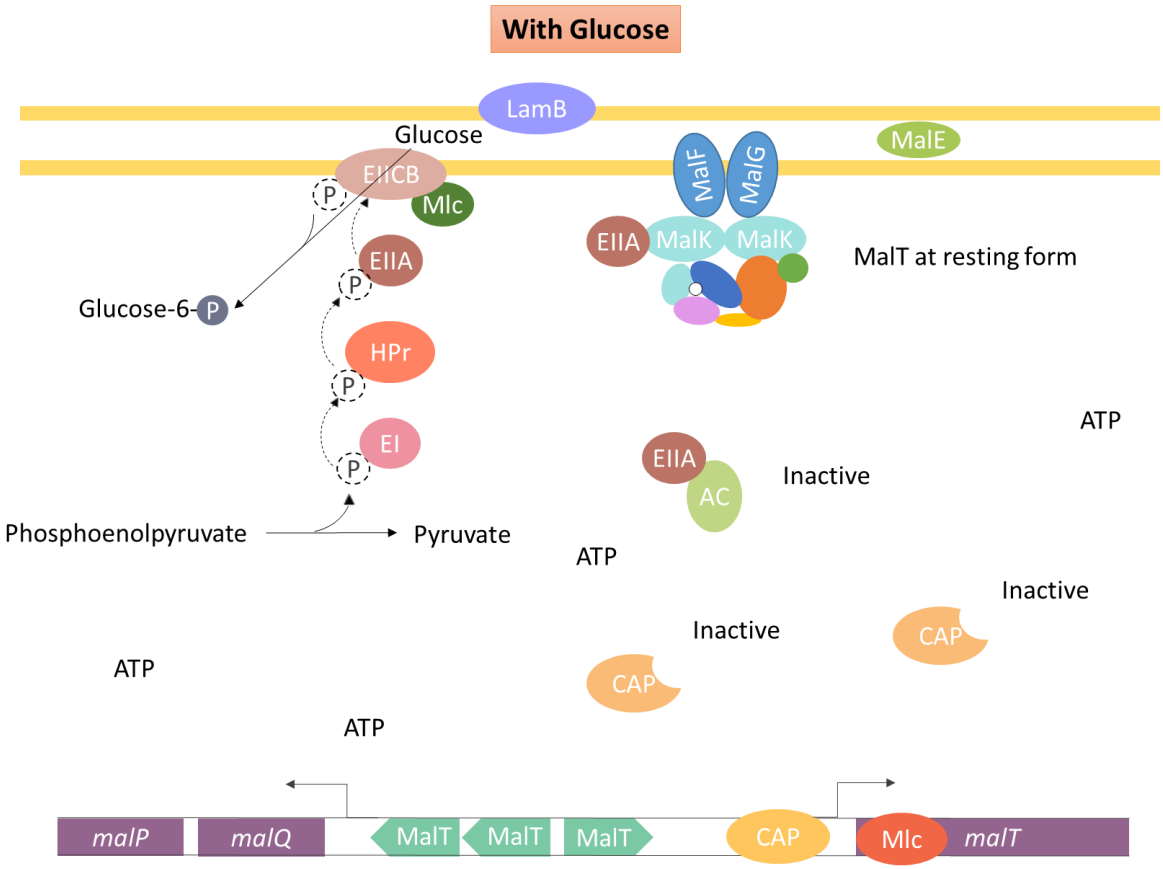

Figure E1: The Response of Maltose Regulon in the Presence of Glucose. When glucose is available, it is transported into the cell and turned into glucose-6-phosphate through the Phosphotransfferase system (PTS). However most enzymes in this system remains in an unphosphorylated form. Mlc, a negative regulator of *malT* is sequestered by unphosphorylated enzyme II CB. Enzyme II A deactivates adenylyl cyclase, and keeps intracellular cAMP concentration low. As a result of this, most catablite activation proteins (CAP) remain inactive, and genes involved in lactose and maltose transportation of metabolism are repressed (metabolite repression).

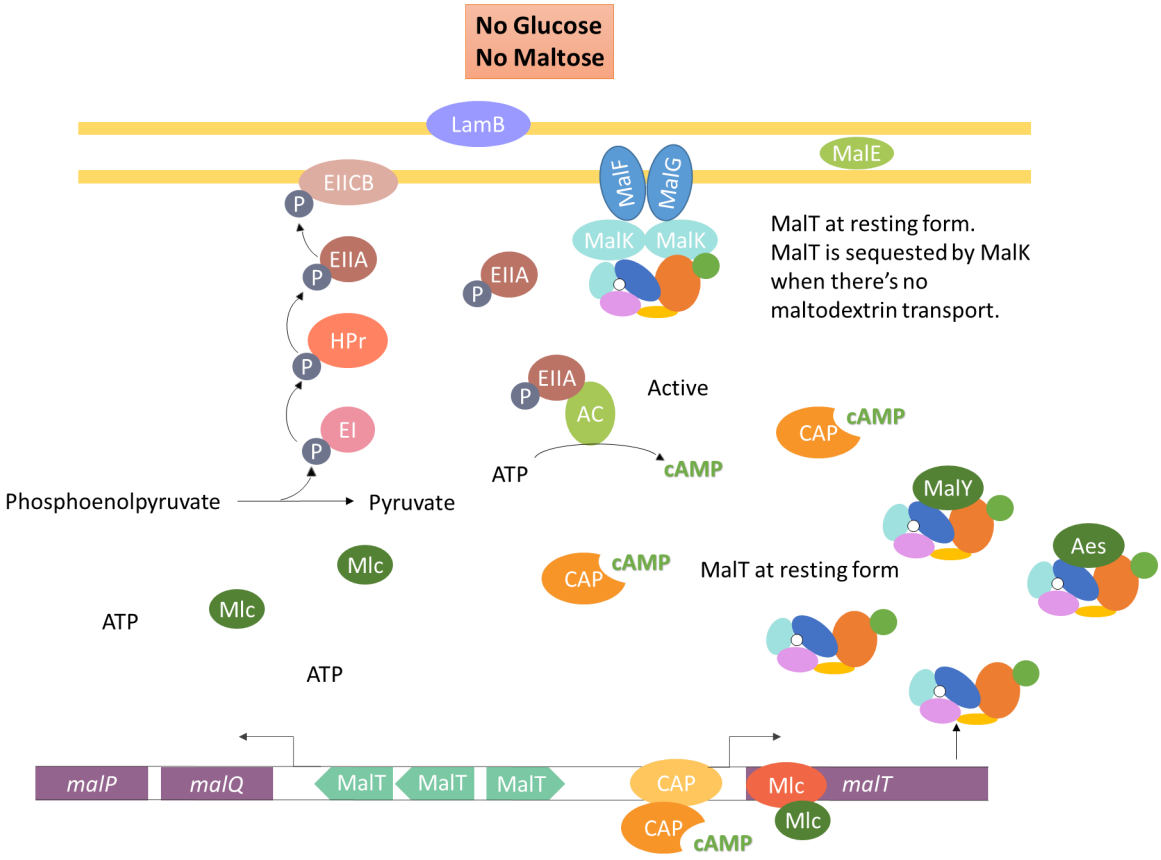

Figure E2: Response of Maltose Regulon in the Absence of Glucose and Maltose. In the absence of glucose, cAMP is produced by phosphorylated enzyme IIA and Adenylyl cyclase. It binds to *malT* promoter region and initiates the production of MalT. In the mean while, Mlc is released from enzyme IICB, and binds to the starting part of *malT* coding gene, which to some degree, represses the synthesis of MalT. In the absence of maltotriose, MalT is at a resting form, and could be sequested by maltodextrin transporter MalK, or interact with negative effectors MalY and AeS.

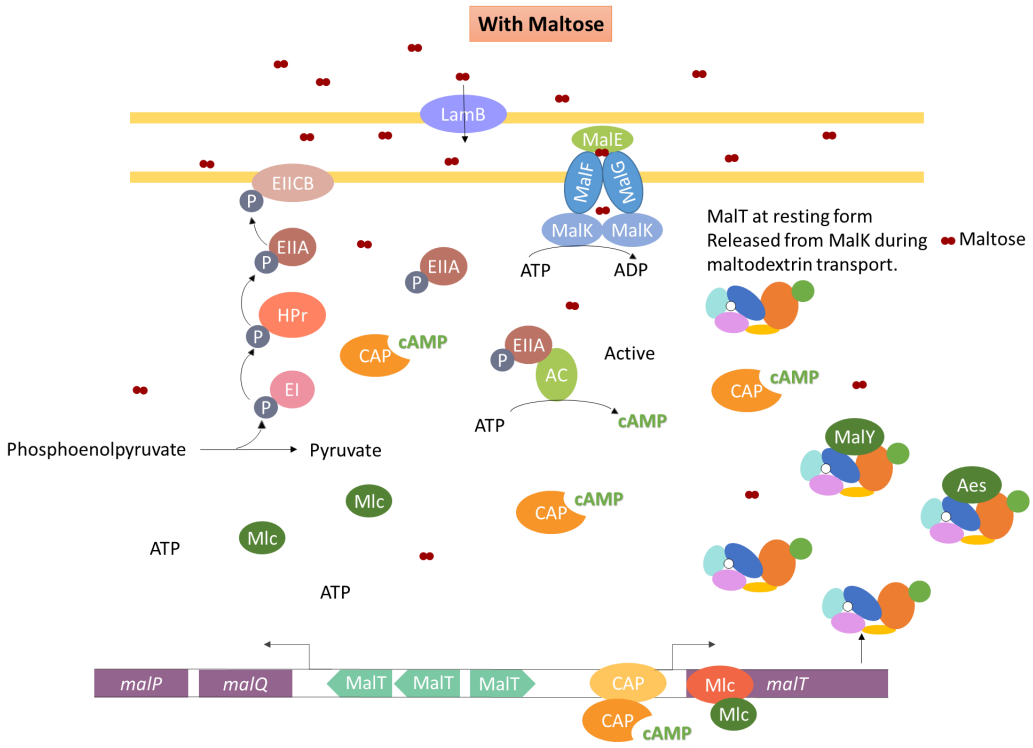

Figure E3: Reponse of Maltose Regulon in the Presence of Maltose. When maltose firstly becomes available, it gets into the cell through a small amount of LamB and MalEFGK2 ABC transport complexes on cell outer and inner membranes. MalT is released from MalK while still remains in a resting form. Maltotriose and ATP are required to activate MalT.

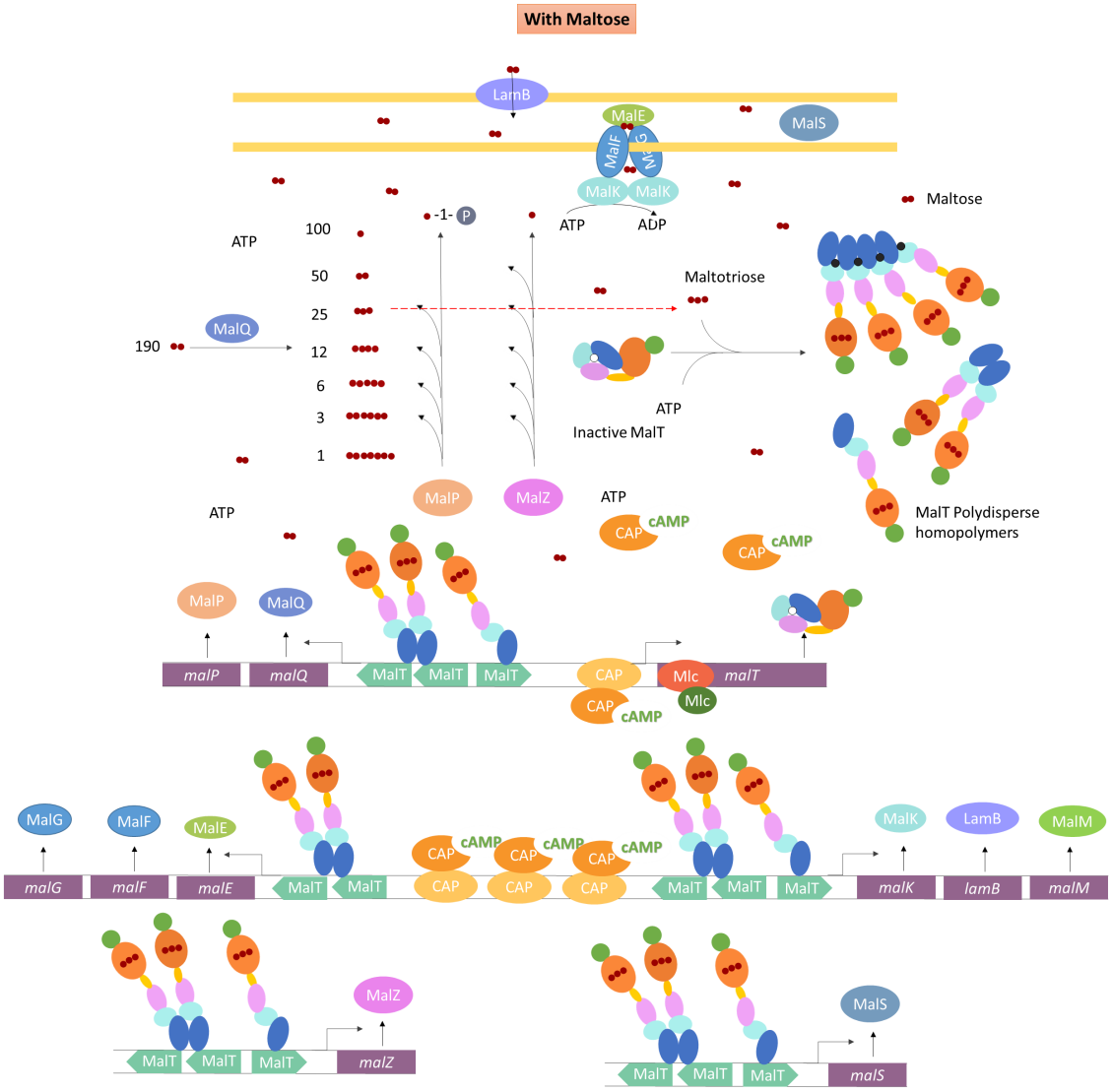

Figure E4: MalT Positive Regulation Loop. As the intracellular maltose concentration increases, with some residue level of MalPQZ, maltose is turned into maltotriose and other forms of maltodextrins. MalT monomers are activated by maltotriose and ATP, and self-associate into polydisperse homopolymers, which bind to the MalT boxes (cyan arrows), and activate all the genes on the maltose regulon. The production of maltose transport (LamB, MalEFGK) and metabolic (MalPQZ) proteins further increases the concentration of maltotriose and active MalT proteins, forming a positive feedback loop.

APPENDIX F

TRANSLATIONAL AND ROTATIONAL VELOCITIES CALCULATIONS

Multiplying both sides of Eq. (4.26) by $\hat{\mathbf{t}}$, we find,

$$\mathbf{V}_o \cdot \hat{\mathbf{t}} = -\frac{Z\left(\boldsymbol{\Omega}_o \times \mathbf{R}\right) \cdot \hat{\mathbf{t}}}{L\zeta_{\parallel} + Z}.$$

Substituting it back into Eq. (4.26), it yields,

$$\begin{aligned}\mathbf{V}_o = \tfrac{1}{L\zeta_{\perp}+Z} \Bigg[& \tfrac{L\left(\zeta_{\parallel}-\zeta_{\perp}\right)}{L\zeta_{\parallel}+Z} Z\left(\boldsymbol{\Omega}_o \times \mathbf{R}\right) \cdot \hat{\mathbf{t}}\hat{\mathbf{t}} - Z\boldsymbol{\Omega}_o \times \mathbf{R} \\ & -\tfrac{1}{2}L^2\zeta_{\perp}\left(\boldsymbol{\Omega}_o \times \hat{\mathbf{t}} + \dot{\theta}\hat{\mathbf{n}} + \sin\theta\dot{\phi}\hat{\mathbf{b}}\right)\Bigg].\end{aligned} \tag{F.1}$$

In the above equation, velocity at O is expressed in terms of its angular velocity Ω_o. Substituting Eq. (F.1) into Eq. (4.27) decouples Ω_o from $\mathbf{V_o}$, and we find,

$$\begin{aligned} -\tfrac{1}{2}L^2\zeta_{\perp}\tfrac{ZR}{L\zeta_{\perp}+Z}\Big[-\hat{\mathbf{t}} \times \left(\boldsymbol{\Omega}_o \times \hat{\mathbf{z}}\right) - \hat{\mathbf{z}} \times \left(\boldsymbol{\Omega}_o \times \hat{\mathbf{t}}\right) - \dot{\theta}\hat{\mathbf{z}} \times \hat{\mathbf{n}} - \sin\theta\dot{\phi}\hat{\mathbf{z}} \times \hat{\mathbf{b}}\Big] \\ + \left[\tfrac{1}{3}L^3\zeta_{\perp} - \left(\tfrac{1}{2}L^2\zeta_{\perp}\right)^2 \tfrac{1}{L\zeta_{\perp}+Z}\right]\left[\dot{\theta}\hat{\mathbf{b}} - \sin\theta\dot{\phi}\hat{\mathbf{n}} + \hat{\mathbf{t}} \times \left(\boldsymbol{\Omega}_o \times \hat{\mathbf{t}}\right)\right] \\ + \left(ZR\right)^2 \tfrac{L\left(\zeta_{\parallel}-\zeta_{\perp}\right)}{\left(L\zeta_{\parallel}+Z\right)\left(L\zeta_{\perp}+Z\right)}\left[\left(\boldsymbol{\Omega}_o \times \hat{\mathbf{z}}\right) \cdot \hat{\mathbf{t}}\right]\left(\hat{\mathbf{z}} \times \hat{\mathbf{t}}\right) \\ -\tfrac{\left(ZR\right)^2}{\left(L\zeta_{\perp}+Z\right)}\hat{\mathbf{z}} \times \left(\boldsymbol{\Omega}_o \times \hat{\mathbf{z}}\right) + ZR^2\hat{\mathbf{z}} \times \left(\boldsymbol{\Omega}_o \times \hat{\mathbf{z}}\right) + M\boldsymbol{\Omega}_o = 0. \end{aligned}$$

To put it into a dimensionless form, I divide each side by $\frac{1}{3}L^3\zeta_{\perp}$ with the result,

$$
\begin{aligned}
-BZ'R'\left[-\hat{\mathbf{t}}\times(\boldsymbol{\Omega}_o\times\hat{\mathbf{z}})-\hat{\mathbf{z}}\times\left(\boldsymbol{\Omega}_o\times\hat{\mathbf{t}}\right)-\dot{\theta}\hat{\mathbf{z}}\times\hat{\mathbf{n}}-\sin\theta\dot{\phi}\hat{\mathbf{z}}\times\hat{\mathbf{b}}\right]\\
+(1-B)\left[\dot{\theta}\hat{\mathbf{b}}-\sin\theta\dot{\phi}\hat{\mathbf{n}}+\hat{\mathbf{t}}\times\left(\boldsymbol{\Omega}_o\times\hat{\mathbf{t}}\right)\right]\\
+AZ'^2R'^2\left(\boldsymbol{\Omega}_o\times\hat{\mathbf{z}}\right)\cdot\hat{\mathbf{t}}\left(\hat{\mathbf{z}}\times\hat{\mathbf{t}}\right)\\
-BZ'^2R'^2\hat{\mathbf{z}}\times(\boldsymbol{\Omega}_o\times\hat{\mathbf{z}})+\mathbf{M}'\boldsymbol{\Omega}_o=0,
\end{aligned}
\tag{F.2}
$$

where the dimensionless quantities are redefined as,

$$
\begin{aligned}
\gamma=\tfrac{\zeta_\parallel}{\zeta_\perp}=0.5,\quad \zeta'_\perp=\tfrac{\zeta_\perp}{\pi\eta},\quad R'=\tfrac{R}{L}=x,\\
Z'=\tfrac{Z}{\frac{1}{2}L\zeta_\perp}=\tfrac{12x}{\zeta'_\perp},\quad A=\tfrac{3(\gamma-1)}{(Z'+2)(Z'+2\gamma)},\quad B=\tfrac{3}{2(Z'+2)}\\
\text{and}\quad \mathbf{M}'=(M'_0,\,M'_0,\,M'_z)=\tfrac{\pi\eta R^3}{\frac{1}{3}L^3\zeta_\perp}(14,\,14,\,8)=\tfrac{3x^3}{\zeta'_\perp}(14,\,14,\,8)\,.
\end{aligned}
\tag{F.3}
$$

Rewriting Eq. (F.2) into a matrix form in the body-fixed coordinate system $Oxyz$, we find,

$$
X\begin{pmatrix}\Omega_{ox}\\ \Omega_{oy}\\ \Omega_{oz}\end{pmatrix}=Y\begin{pmatrix}\dot{\theta}\\ \dot{\phi}\sin\theta\end{pmatrix},
\tag{F.4}
$$

$$
\text{where}\quad Y=\begin{pmatrix}BZ'R'n_y-(1-B)\,\phi_x & BZ'R'\phi_y+(1-B)\,n_x\\ -BZ'R'n_x-(1-B)\,\phi_y & -BZ'R'\phi_x+(1-B)\,n_y\\ -(1-B)\,\phi_z & (1-B)\,n_z\end{pmatrix},
$$

$$
\text{and}\quad X=[H,\,J,\,K]\quad\text{with}
$$

$$
H=\begin{pmatrix}M'_x+1-B-BZ'^2R'^2+2BZ'R't_z-(1-B)\,t_x^2+AZ'^2R'^2t_y^2\\ -(1-B)\,t_xt_y-AZ'^2R'^2t_xt_y\\ -BZ'R't_x-(1-B)\,t_xt_z\end{pmatrix},
$$

$$
J=\begin{pmatrix}-(1-B)\,t_xt_y-AZ'^2R'^2t_xt_y\\ M'_y+1-B-BZ'^2R'^2+2BZ'R't_z-(1-B)\,t_y^2+AZ'^2R'^2t_x^2\\ -BZ'R't_y-(1-B)\,t_yt_z\end{pmatrix},
$$

$$\text{and} \quad K = \begin{pmatrix} -BZ'R't_x - (1-B)\, t_x t_z \\ -BZ'R't_y - (1-B)\, t_y t_z \\ (1-B) - (1-B)\, t_z^2 + M'_z \end{pmatrix},$$

where the definitions for unit vectors $\hat{t}$, $\hat{n}$, and $\hat{b}$ can be found in Eq. (4.1), and their are related to the laboratory coordinates by,

$$\begin{pmatrix} \hat{\mathbf{t}} \\ \hat{\mathbf{b}} \\ \hat{\mathbf{n}} \end{pmatrix} = \begin{pmatrix} t_x & t_y & t_z \\ b_x & b_y & b_z \\ n_x & n_y & n_z \end{pmatrix} \begin{pmatrix} \hat{\mathbf{x}} \\ \hat{\mathbf{y}} \\ \hat{\mathbf{z}} \end{pmatrix}.$$

To solve for $\mathbf{\Omega}_o$, I break the coefficient matrix X into 3 matrices with the hope that by diagonalizing each of them, a simpler form will appear. Ω_o can then be solved directly by inverting the simplified coefficient matrix.

$$X = X_1 + X_2 + C,$$

$$\text{where} \quad X_1 = -(1-B) \begin{pmatrix} t_x^2 & t_y t_x & t_z t_x \\ t_x t_y & t_y^2 & t_z t_y \\ t_x t_z & t_y t_z & t_z^2 \end{pmatrix},$$

$$X_2 = \begin{pmatrix} AZ'^2R'^2t_y^2 & -AZ'^2R'^2t_x t_y & -BZ'R't_x \\ -AZ'^2R'^2t_x t_y & AZ'^2R'^2t_x^2 & -BZ'R't_y \\ -BZ'R't_x & -BZ'R't_y & \Delta M' \end{pmatrix},$$

$$\text{with} \quad \Delta M' = M'_z - M'_0 + BZ'^2R'^2 - 2BZ'R't_z$$

$$\text{and} \quad C = \left(M'_0 + 1 - B - BZ'^2R'^2 + 2BZ'R't_z\right) \begin{pmatrix} 1 & 0 & 0 \\ 0 & 1 & 0 \\ 0 & 0 & 1 \end{pmatrix}.$$

Matrix X_1 can be diagonalized by an orthogonal matrix Λ,

$$\Lambda = \begin{pmatrix} n_x & b_x & t_x \\ n_y & b_y & t_y \\ n_z & b_z & t_z \end{pmatrix},$$

$$\Lambda^{-1} X_1 \Lambda = \begin{pmatrix} 0 & 0 & 0 \\ 0 & 0 & 0 \\ 0 & 0 & B-1 \end{pmatrix}.$$

Substituting $\mathbf{\Omega}_o$ in Eq. (F.4) with $\mathbf{\Omega}_o = \Lambda \mathbf{\Omega}'_o$ and multiply both sides by Λ^{-1} on the left, we find,

$$\left[\begin{pmatrix} 0 & 0 & 0 \\ 0 & 0 & 0 \\ 0 & 0 & B-1 \end{pmatrix} + \Lambda^{-1} X_2 \Lambda + C \right] \begin{pmatrix} \Omega'_{ox} \\ \Omega'_{oy} \\ \Omega'_{oz} \end{pmatrix} = \Lambda^{-1} Y \begin{pmatrix} \dot{\theta} \\ \dot{\phi} \sin\theta \end{pmatrix}, \tag{F.5}$$

Where, $\Lambda^{-1} X_2 \Lambda =$

$$\begin{pmatrix} 2BZ'R'n_z^2 t_z + \Delta M' n_z^2 & 0 & 2BZ'R't_z^2 n_z - BZ'R'n_z + \Delta M' t_z n_z \\ 0 & AZ'^2 R'^2 \sin^2\theta & 0 \\ 2BZ'R'n_z t_z^2 - BZ'R'n_z + \Delta M' n_z t_z & 0 & -2BZ'R't_z\left(1-t_z^2\right) + \Delta M t_z^2 \end{pmatrix},$$

To simplify the notation, we define a P matrix as,

$$\begin{aligned} P &= \left[\begin{pmatrix} 0 & 0 & 0 \\ 0 & 0 & 0 \\ 0 & 0 & B-1 \end{pmatrix} + \Lambda^{-1} X_2 \Lambda + C \right] \\ &= \begin{pmatrix} a & 0 & d \\ 0 & b & 0 \\ d & 0 & c \end{pmatrix}. \end{aligned}$$

It then follows,

$$\begin{pmatrix} \Omega_{ox} \\ \Omega_{oy} \\ \Omega_{oz} \end{pmatrix} = \Lambda \begin{pmatrix} \Omega'_{ox} \\ \Omega'_{oy} \\ \Omega'_{oz} \end{pmatrix} = \Lambda P^{-1} \Lambda^{-1} Y \begin{pmatrix} \dot{\theta} \\ \dot{\phi} \sin\theta \end{pmatrix}, \tag{F.6}$$

$$\text{with} \quad P^{-1} = \frac{1}{ac - d^2} \begin{pmatrix} c & 0 & -d \\ 0 & \frac{ac-d^2}{b} & 0 \\ -d & 0 & a \end{pmatrix},$$

where

$$a = (M'_z - M'_0)\, n_z^2 + M'_0 + 1 - B\,(Z' R' t_z - 1)^2\,,$$

$$c = (M'_z - M'_0)\, t_z^2 - B Z'^2 R'^2 n_z^2 + M'_0,$$

$$b = A Z'^2 R'^2 \sin^2\theta + M'_0 + 1 + B - B Z'^2 R'^2 + 2 B Z' R' t_z,$$

$$d = (M'_z - M'_0)\, n_z t_z + B Z'^2 R'^2 n_z t_z - B Z' R' n_z,$$

$$\text{and} \quad ac - d^2 = (M'_z - M'_0)\left(-B Z'^2 R'^2 + M' + t_z^2 + 2 B Z' R' t_z - B t_z^2\right).$$

After some simplifications, the final expression for $\mathbf{\Omega}_o$ is,

$$\begin{pmatrix} \Omega_{ox} \\ \Omega_{oy} \\ \Omega_{oz} \end{pmatrix} = \begin{pmatrix} \frac{\sigma_1(\theta)}{\sigma_3(\theta)} \sin\phi & \frac{\sigma_2(\theta)}{\sigma_4(\theta)} \cos\phi \\ -\frac{\sigma_1(\theta)}{\sigma_3(\theta)} \cos\phi & \frac{\sigma_2(\theta)}{\sigma_4(\theta)} \sin\phi \\ 0 & \frac{\sigma_6(\theta)}{\sigma_4(\theta)} \end{pmatrix} \begin{pmatrix} \dot{\theta} \\ \dot{\phi} \sin\theta \end{pmatrix}, \tag{F.7}$$

$$\text{with} \quad \sigma_1 = B R' Z' \cos\theta - B + 1,$$

$$\sigma_2 = M'_z \left[(1 - B)\cos\theta + B R' Z'\right],$$

$$\sigma_3 = M_0' - B + AR'^2Z'^2\sin^2\theta - BR'^2Z'^2 + 2BR'Z'\cos\theta + 1,$$

$$\sigma_4 = \left(M_0'\sin^2\theta + M_z'\cos^2\theta\right)(1-B) + M_0'M_z' - BR'^2Z'^2\sin^2\theta \\ -BM_z'R'^2Z'^2 + 2BM_z'R'Z'\cos\theta,$$

$$\text{and} \quad \sigma_6 = \left[BR'^2Z'^2 - (1-B)\,M_0'\right]\sin\theta.$$

Reorganizing Eq. (F.1), cell-body translational velocity $\mathbf{V}_o$ can be written in a matrix form in the body fixed coordinates. I get,

$$\frac{1}{L}\begin{pmatrix} V_{ox} \\ V_{oy} \\ V_{oz} \end{pmatrix} = \frac{2}{3}\begin{pmatrix} AZ'R't_xt_y & -AZ'R't_x^2 + BZ'R' - Bt_z & Bt_y \\ AZ'R't_y^2 - BZ'R' + Bt_z & -AZ'R't_xt_y & -Bt_x \\ AZ'R't_yt_z - Bt_y & -AZ'R't_xt_z + Bt_x & 0 \end{pmatrix} \\ \cdot \begin{pmatrix} \Omega_{ox} \\ \Omega_{oy} \\ \Omega_{oz} \end{pmatrix} - \frac{2}{3}B\begin{pmatrix} n_x & b_x \\ n_y & b_y \\ n_z & b_z \end{pmatrix}\begin{pmatrix} \dot{\theta} \\ \dot{\phi}\sin\theta \end{pmatrix}$$

Substituting Eq. (F.7), the solution for $\mathbf{\Omega}_o$, in the above equation, it yields,

$$\frac{1}{L}\begin{pmatrix} V_{ox} \\ V_{oy} \\ V_{oz} \end{pmatrix} = \frac{2}{3}\begin{pmatrix} -\frac{\rho_1(\theta)}{\sigma_3(\theta)}\cos\phi & \frac{\rho_2(\theta)}{\sigma_4(\theta)}\sin\phi \\ -\frac{\rho_1(\theta)}{\sigma_3(\theta)}\sin\phi & -\frac{\rho_2(\theta)}{\sigma_4(\theta)}\cos\phi \\ \frac{\rho_3(\theta)}{\sigma_3(\theta)} & 0 \end{pmatrix}\begin{pmatrix} \dot{\theta} \\ \dot{\phi}\sin\theta \end{pmatrix},$$

$$\text{with} \quad \rho_1 = R'Z'\left[B - \left(A + B^2 - AB\right)\sin^2\theta\right] + BM_0'\cos\theta,$$

$$\rho_2 = BM_z'\left(M_0' + R'Z'\cos\theta\right),$$

$$\text{and} \quad \rho_3 = \left[R'Z'\left(A + B^2 - AB\right)\cos\theta + BM_0' - B^2R'^2Z'^2 + ABR'^2Z'^2\right]\sin\theta.$$

Finally, the velocity of cell center $\mathbf{V}_c = \mathbf{V_o} + \mathbf{\Omega_o} \times \mathbf{R}$ is given by,

$$\begin{pmatrix} V_{cx} \\ V_{cy} \\ V_{cz} \end{pmatrix} = \begin{pmatrix} \left(-\frac{2}{3}L\rho_1 + a\sigma_1\right)\frac{1}{\sigma_3}\cos\phi & \left(\frac{2}{3}L\rho_2 - a\sigma_2\right)\frac{1}{\sigma_4}\sin\phi \\ \left(-\frac{2}{3}L\rho_1 + a\sigma_1\right)\frac{1}{\sigma_3}\sin\phi & -\left(\frac{2}{3}L\rho_2 - a\sigma_2\right)\frac{1}{\sigma_4}\cos\phi \\ \frac{2}{3}L\frac{\rho_3}{\sigma_3} & 0 \end{pmatrix} \begin{pmatrix} \dot{\theta} \\ \dot{\phi}\sin\theta \end{pmatrix}, \quad \text{(F.8)}$$

To prepare for energy calculations, I transform $\mathbf{\Omega}_o$, $\mathbf{V}_o$, and $\mathbf{V}_c$ back into spherical coordinates as,

$$\begin{aligned} \begin{pmatrix} \Omega_{ot} \\ \Omega_{ob} \\ \Omega_{on} \end{pmatrix} &= \begin{pmatrix} \sin\theta\cos\phi & \sin\theta\sin\phi & \cos\theta \\ -\sin\phi & \cos\phi & 0 \\ \cos\theta\cos\phi & \cos\theta\sin\phi & -\sin\theta \end{pmatrix} \begin{pmatrix} \Omega_{ox} \\ \Omega_{oy} \\ \Omega_{oz} \end{pmatrix} \\ &= \begin{pmatrix} \left(\sigma_2\sin\theta + \sigma_6\cos\theta\right)\frac{\dot{\phi}\sin\theta}{\sigma_4} \\ -\frac{\sigma_1}{\sigma_3}\dot{\theta} \\ \left(\sigma_2\cos\theta - \sigma_6\sin\theta\right)\frac{\dot{\phi}\sin\theta}{\sigma_4} \end{pmatrix}, \end{aligned}$$

$$\begin{aligned} \begin{pmatrix} V_{ot} \\ V_{ob} \\ V_{on} \end{pmatrix} &= \begin{pmatrix} \sin\theta\cos\phi & \sin\theta\sin\phi & \cos\theta \\ -\sin\phi & \cos\phi & 0 \\ \cos\theta\cos\phi & \cos\theta\sin\phi & -\sin\theta \end{pmatrix} \begin{pmatrix} V_{ox} \\ V_{oy} \\ V_{oz} \end{pmatrix} \\ &= \frac{2}{3}L \begin{pmatrix} \left(-\frac{\rho_1}{\sigma_3}\sin\theta + \frac{\rho_3(\theta)}{\sigma_3(\theta)}\cos\theta\right)\dot{\theta} \\ -\frac{\rho_2}{\sigma_4}\sin\theta\dot{\phi} \\ -\left(\frac{\rho_1}{\sigma_3}\cos\theta + \frac{\rho_3(\theta)}{\sigma_3(\theta)}\sin\theta\right)\dot{\theta} \end{pmatrix}, \end{aligned}$$

$$\text{and} \quad \begin{aligned} \begin{pmatrix} V_{ct} \\ V_{cb} \\ V_{cn} \end{pmatrix} &= \begin{pmatrix} \sin\theta\cos\phi & \sin\theta\sin\phi & \cos\theta \\ -\sin\phi & \cos\phi & 0 \\ \cos\theta\cos\phi & \cos\theta\sin\phi & -\sin\theta \end{pmatrix} \begin{pmatrix} V_{cx} \\ V_{cy} \\ V_{cz} \end{pmatrix} \\ &= \begin{pmatrix} \left(\kappa_1\sin\theta + \kappa_3\cos\theta\right)\dot{\theta} \\ -\kappa_2\dot{\phi}\sin\theta \\ \left(\kappa_1\cos\theta - \kappa_3\sin\theta\right)\dot{\theta} \end{pmatrix}, \end{aligned}$$

$$\text{with} \quad \kappa_1 = \left(-\frac{2}{3} L\rho_1 + a\sigma_1 \right) \frac{1}{\sigma_3},$$

$$\kappa_2 = \left(\frac{2}{3} L\rho_2 - a\sigma_2 \right) \frac{1}{\sigma_4}$$

$$\text{and} \quad \kappa_3 = \frac{2}{3} L \frac{\rho_3}{\sigma_3}$$

APPENDIX G

THE EFFECTIVENESS OF VENUS REPORTER

The best way to calibrate [CheY] as a function of IPTG induction levels, is to use a CheY-Venus fusion protein, such that the fluorescence intensity of Venus directly reports the abundance of CheY protein. This is implemented in strain LX3, which contains a plasmid pMMB-fYV expressing CheY-Venus fusions under the control of an IPTG inducible *lac* promoter. To avoid possible interference in CheY function from the fusion protein, another strain LX1 was constructed. LX1 includes a plasmid pMMBYV, on which CheY and Venus proteins are expressed separately but sharing the same promoter.

Fluorescence pictures were taken following the instructions in Appendix C. The cellular protein copy number and concentration were plotted in Fig. G1. Throughout the whole IPTG induction concentration range ($0 - 100\,\mu$M), the two curves cover the same protein concentration range, $0.1 - 1\,\mu$M, suggesting that the expression level of CheY in LX1 strain can be well represented by Venus copy number or fluorescence intensity.

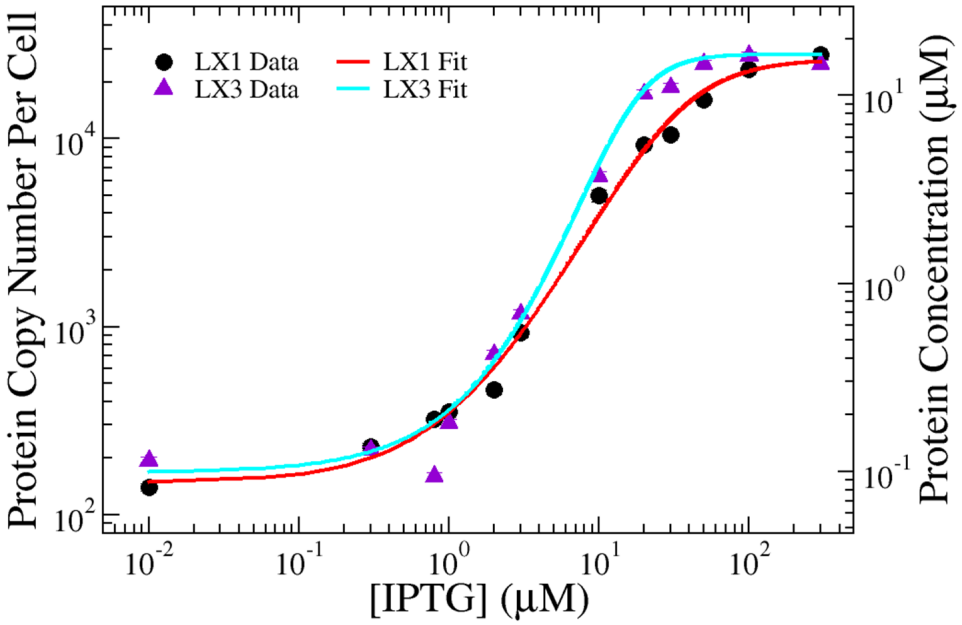

Figure G1: Intracellular CheY Concentration Calibration Curves. The red (cyan) sigmoidal curve represents Venus (CheY-Venus) copy number or intracellular concentration in LX1 (LX3) as a function of [IPTG]. Here the average volume of YM4, based on our measurements, is around $2.82\,\mu\mathrm{m}^3$.

APPENDIX H

SPEED AND SIZE DISTRIBUTIONS OF *VIBRIO ALGINOLYTICUS* STRAINS

Bacterial major axis length $2a$ and speed histograms are shown in Fig. H1 and in Fig. H2. Each panel represents: (A) YM4, (B) LX2, (C) LX1 with 0 μM IPTG, (D) LX1 with 0.3 μM IPTG, (E) LX1 with 1 μM IPTG, (F) LX1 with 3 μM IPTG, (G) LX1 with 10 μM IPTG, (H) LX1 with 30 μM IPTG, and (I) LX1 with 100 μM IPTG, respectively.

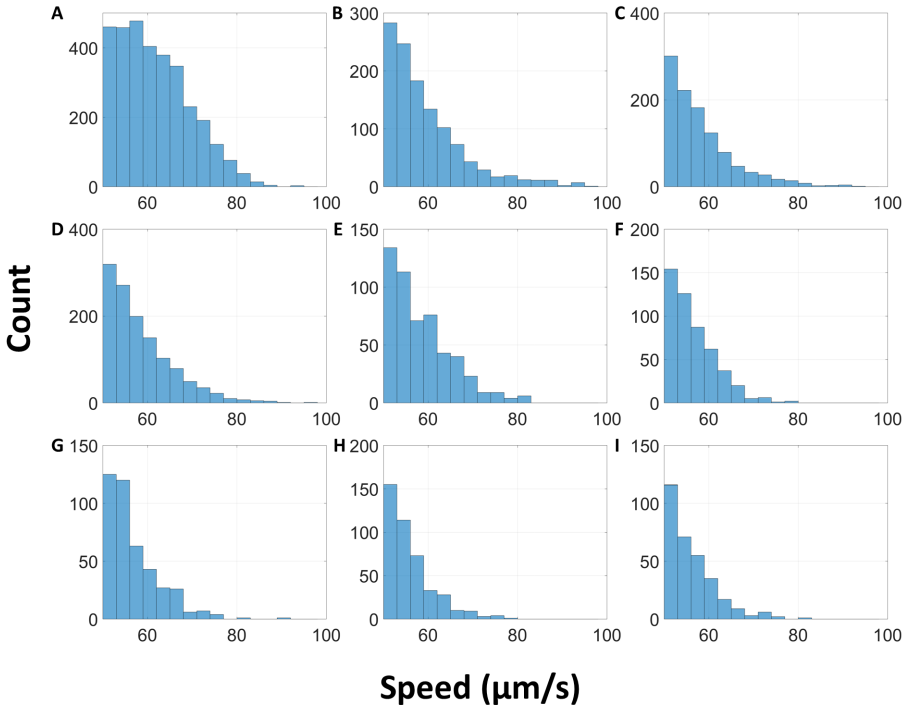

Figure H1: *Vibrio alginolyticus* Speed Histograms.

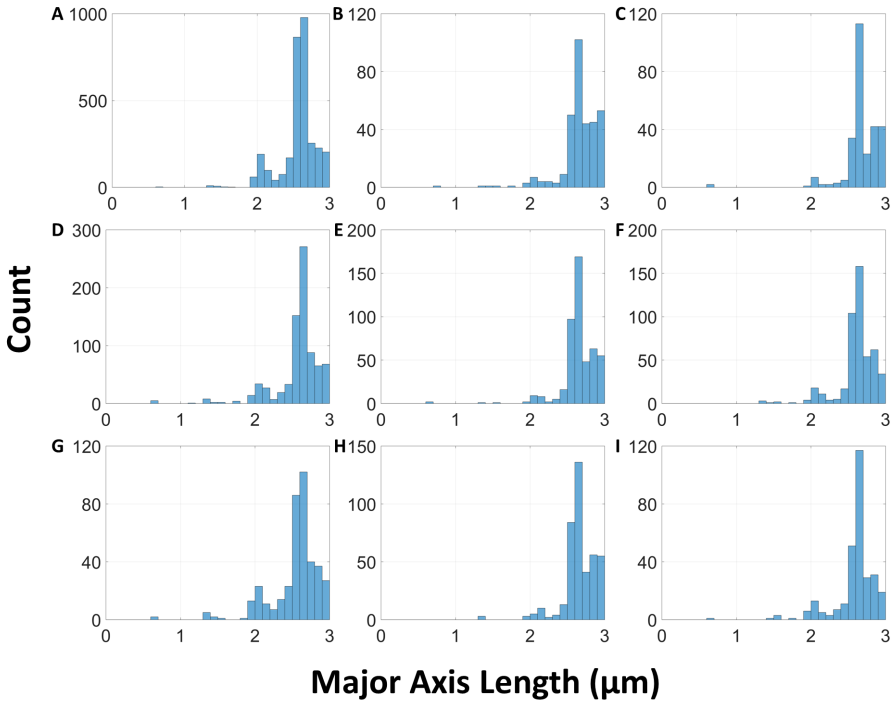

Figure H2: *Vibrio alginolyticus* Major Axis Length Histograms.

BIBLIOGRAPHY

[1] Mads Kaern, Timothy C. Elston, William J. Blake, and James J. Collins. Stochasticity in gene expression: from theories to phenotypes. *Nat Rev Genet*, 6(6):451–464, 2005.

[2] David Dubnau and Richard Losick. Bistability in bacteria. *Molecular Microbiology*, 61(3):564–572, 2006.

[3] Michael B. Elowitz, Arnold J. Levine, Eric D. Siggia, and Peter S. Swain. Stochastic gene expression in a single cell. *Science*, 297(5584):1183–1186, 2002.

[4] Ertugrul M. Ozbudak, Mukund Thattai, Iren Kurtser, Alan D. Grossman, and Alexander van Oudenaarden. Regulation of noise in the expression of a single gene. *Nature Genetics*, 31:69–73, 2002.

[5] Nir Friedman, Long Cai, and X. Sunney Xie. Linking stochastic dynamics to population distribution: An analytical framework of gene expression. *Phys. Rev. Lett.*, 97:168302, Oct 2006.

[6] Aaron Novick and Milton Weiner. Enzyme induction as an all-or-none phenomenon. *Proceedings of the National Academy of Sciences of the United States of America*, 43(7):553–566, 1957.

[7] Paul J. Choi, Long Cai, Kirsten Frieda, and X. Sunney Xie. A stochastic single-molecule event triggers phenotype switching of a bacterial cell. *Science (New York, N.Y.)*, 322(5900):442, 2008.

[8] W. Boos and H. Shuman. Maltose/maltodextrin system of *Escherichia coli*: transport, metabolism, and regulation. *Microbiol. and Mol. Biol. Reviews*, 62:204–229, 1998.

[9] Edo Kussell and Stanislas Leibler. Phenotypic diversity, population growth, and information in fluctuating environments. *Science*, 309(5743):2075–2078, 2005.

[10] Francois Jacob and Jacques Monod. Genetic regulatory mechanisms in the synthesis of proteins. *J Mol Biol*, 3:318–56, 1961.

[11] Linda L. McCarter. Polar flagellar motility of the *Vibrionaceae*. *Microbiology and Molecular Biology Reviews*, 65(3):445–462, 2001.

[12] Howard C Berg. *E. coli in Motion*. Springer Science & Business Media, 2008.

[13] Patrick J. Mears, Santosh Koirala, Chris V. Rao, Ido Golding, and Yann R. Chemla. *Escherichia coli* swimming is robust against variations in flagellar number. *eLife*, 3:e01916, 2014.

[14] Yang Yang, Jing He, Tuba Altindal, Li Xie, and Xiao-Lun Wu. A non-poissonian flagellar motor switch increases bacterial chemotactic potential. *Biophysical Journal*, 109(5):1058–1069, 2015.

[15] Victor Sourjik. Receptor clustering and signal processing in *E. coli* chemotaxis. *Trends in Microbiology*, 12(12):569–576, 2004.

[16] Noreen R. Francis, Gina E. Sosinsky, Dennis Thomas, and David J. DeRosier. Isolation, characterization and structure of bacterial flagellar motors containing the switch complex. *Journal of Molecular Biology*, 235(4):1261 – 1270, 1994.

[17] N. Hosogi, H. Shigematsu, H. Terashima, M. Homma, and K. Nagayama. Zernike phase contrast cryo-electron tomography of sodium-driven flagellar hook-basal bodies from *Vibrio alginolyticus*. *J Struct Biol*, 173(1):67–76, 2011.

[18] Li Xie, Tuba Altindal, Suddhashil Chattopadhyay, and Xiao-Lun Wu. Bacterial flagellum as a propeller and as a rudder for efficient chemotaxis. *Proceedings of the National Academy of Sciences*, 108(6):2246–2251, 2011.

[19] Kwangmin Son, Jeffrey S. Guasto, and Roman Stocker. Bacteria can exploit a flagellar buckling instability to change direction. *Nat Phys*, 9(8):494–498, 2013.

[20] Stephen P Timoshenko and James M Gere. *Theory of Elastic Stability 2nd edn*. McGraw-Hill, 1961.

[21] Marc Erhardt, Hanna M Singer, Daniel H Wee, James P Keener, and Kelly T Hughes. An infrequent molecular ruler controls flagellar hook length in *Salmonella enterica*. *The EMBO Journal*, 30(14):2948–2961, 2011.

[22] E. M. Ozbudak, M. Thattai, H. N. Lim, B. I. Shraiman, and A. Van Oudenaarden. Multistability in the lactose utilization network of *Escherichia coli*. *Nature*, 427(6976):737–40, 2004.

[23] Rachel A. Schubert, Ian B. Dodd, J. Barry Egan, and Keith E. Shearwin. Cro's role in the CI-Cro bistable switch is critical for λ's transition from lysogeny to lytic development. *Genes & Development*, 21(19):2461–2472, 2007.

[24] H. Maamar and D. Dubnau. Bistability in the *Bacillus subtilis* K-state (competence) system requires a positive feedback loop. *Mol Microbiol*, 56(3):615–24, 2005.

[25] W. K. Smits, C. C. Eschevins, K. A. Susanna, S. Bron, O. P. Kuipers, and L. W. Hamoen. Stripping *Bacillus*: ComK auto-stimulation is responsible for the bistable response in competence development. *Mol Microbiol*, 56(3):604–14, 2005.

[26] T. Eppler, P. Postma, A. Schutz, U. Volker, and W. Boos. Glycerol-3-phosphate-induced catabolite repression in *E. coli*. *J. Bacteriol.*, 184:3044–3052, 2002.

[27] E. Chapman-McQuiston and X. L. Wu. Stochastic receptor expression allows sensitive bacteria to evade phage attack. Part I: Experiments. *Biophysical Journal*, 94(11):4525–4536, 2008.

[28] A. R. Ureta, R. G. Endres, N. S. Wingreen, and T. J. Silhavy. Kinetic analysis of the assembly of the outer membrane protein LamB in *Escherichia coli* mutants each lacking a secretion or targeting factor in a different cellular compartment. *J Bacteriol*, 189(2):446–54, 2007.

[29] T. Nagai, K. Ibata, E. S. Park, M. Kubota, K. Mikoshiba, and A. Miyawaki. A variant of yellow fluorescent protein with fast and efficient maturation for cell-biological applications. *Nat Biotechnol*, 20(1):87–90, 2002.

[30] F. W. J. Teale and G. Weber. Ultraviolet fluorescence of the aromatic amino acids. *Biochemical Journal*, 65(3):476–482, 1957.

[31] I. Golding, J. Paulsson, S. M. Zawilski, and E. C. Cox. Real-time kinetics of gene activity in individual bacteria. *Cell*, 123(6):1025–36, 2005.

[32] Yuichi Taniguchi, Paul J. Choi, Gene-Wei Li, Huiyi Chen, Mohan Babu, Jeremy Hearn, Andrew Emili, and X. Sunney Xie. Quantifying *E. coli* proteome and transcriptome with single-molecule sensitivity in single cells. *Science (New York, N.Y.)*, 329(5991):533–538, 2010.

[33] Ji Yu, Jie Xiao, Xiaojia Ren, Kaiqin Lao, and X. Sunney Xie. Probing gene expression in live cells, one protein molecule at a time. *Science*, 311(5767):1600–1603, 2006.

[34] Kirill A. Datsenko and Barry L. Wanner. One-step inactivation of chromosomal genes in *Escherichia coli* K-12 using PCR products. *Proceedings of the National Academy of Sciences*, 97(12):6640–6645, 2000.

[35] Conghui You, Hiroyuki Okano, Sheng Hui, Zhongge Zhang, Minsu Kim, Carl W. Gunderson, Yi-Ping Wang, Peter Lenz, Dalai Yan, and Terence Hwa. Coordination of bacterial proteome with metabolism by cyclic AMP signalling. *Nature*, 500(7462):301–306, 2013.

[36] Hiroshi Akashi and Takashi Gojobori. Metabolic efficiency and amino acid composition in the proteomes of *Escherichia coli* and *Bacillus subtilis*. *Proceedings of the National Academy of Sciences*, 99(6):3695–3700, 2002.

[37] Roger Y Adelberg Stanier, Edward A Ingraham, John L Roger Y Stanier, Edward A Adelberg, and John L Ingraham. *The microbial world*. Prentice Hall College Div.

[38] Geoffrey Zubay, W Parson, and DE Vance. *Principles of biochemistry*. WCB, 1995.

[39] Maxime Durot, Pierre-Yves Bourguignon, and Vincent Schachter. Genome-scale models of bacterial metabolism: reconstruction and applications. *FEMS microbiology reviews*, 33(1):164–190, 2009.

[40] Gerhard Gottschalk. *Bacterial metabolism*. Springer Science & Business Media, 2012.

[41] E Almaas, B Kovacs, T Vicsek, ZN Oltvai, and A-L Barabási. Global organization of metabolic fluxes in the bacterium *Escherichia coli*. *Nature*, 427(6977):839–843, 2004.

[42] Toshifumi Inada, Keiko Kimata, and Hiroji Aiba. Mechanism responsible for glucose-lactose diauxie in *Escherichia coli*: challenge to the cAMP model. *Genes to Cells*, 1(3):293–301, 1996.

[43] William F Loomis and Boris Magasanik. Glucose-lactose diauxie in *Escherichia coli*. *Journal of bacteriology*, 93(4):1397–1401, 1967.

[44] Matthew F Traxler, Dong-Eun Chang, and Tyrrell Conway. Guanosine 3', 5'-bispyrophosphate coordinates global gene expression during glucose-lactose diauxie in *Escherichia coli*. *Proceedings of the National Academy of Sciences of the United States of America*, 103(7):2374–2379, 2006.

[45] Adam M Feist, Christopher S Henry, Jennifer L Reed, Markus Krummenacker, Andrew R Joyce, Peter D Karp, Linda J Broadbelt, Vassily Hatzimanikatis, and Bernhard Ø Palsson. A genome-scale metabolic reconstruction for *Escherichia coli* K-12 MG1655 that accounts for 1260 ORFs and thermodynamic information. *Molecular systems biology*, 3(1), 2007.

[46] Jeffrey D Orth, Tom M Conrad, Jessica Na, Joshua A Lerman, Hojung Nam, Adam M Feist, and Bernhard Ø Palsson. A comprehensive genome-scale reconstruction of *Escherichia coli* metabolism-2011. *Molecular systems biology*, 7(1):535, 2011.

[47] Daniel Segre, Dennis Vitkup, and George M Church. Analysis of optimality in natural and perturbed metabolic networks. *Proceedings of the National Academy of Sciences*, 99(23):15112–15117, 2002.

[48] Richard I Leavitt and HE Umbarger. Isoleucine and valine metabolism in *Escherichia coli* XI. K-12 valine inhibition of the growth of *Escherichia coli* strain. *Journal of bacteriology*, 83(3):624–630, 1962.

[49] T Meinnel, Y Mechulam, and S Blanquet. Methionine as translation start signal: a review of the enzymes of the pathway in *Escherichia coli*. *Biochimie*, 22:1061–1075, 1991.

[50] R C Greene. *Biosynthesis of methionine*. ASM Press, Washington, D.C., 1996.

[51] N L Tuite, K R Fraser, and C P O'Byrne. Homocysteine toxicity in *Escherichia coli* is caused by a perturbation of branched-chain amino acid biosynthesis. *J. Bacteriology*, 187:4362–4371, 2005.

[52] Lewis I Pizer. Glycine synthesis and metabolism in *Escherichia coli*. *Journal of Bacteriology*, 89(4):1145–1150, 1965.

[53] Margot K Sands and Richard B Roberts. The effects of a tryptophan-histidine deficiency in a mutant of *Escherichia coli*. *Journal of bacteriology*, 63(4):505, 1952.

[54] Gunther S Stent and Sydney Brenner. A genetic locus for the regulation of ribonucleic acid synthesis. *Proceedings of the National Academy of Sciences of the United States of America*, 47(12):2005–2014, 1961.

[55] Tim Durfee, Anne-Marie Hansen, Huijun Zhi, Frederick R. Blattner, and Ding Jun Jin. Transcription profiling of the stringent response in *Escherichia coli*. *Journal of Bacteriology*, 190(3):1084–1096, 2008.

[56] Brian J. Paul, Melanie B. Berkmen, and Richard L. Gourse. DksA potentiates direct activation of amino acid promoters by ppGpp. *Proceedings of the National Academy of Sciences*, 102(22):7823–7828, 2005.

[57] A. Teich, S. Meyer, H. Y. Lin, L. Andersson, S.-O. Enfors, and P. Neubauer. Growth rate related concentration changes of the starvation response regulators σ^S and ppGpp in glucose-limited fed-batch and continuous cultures of *Escherichia coli*. *Biotechnology Progress*, 15(1):123–129, 1999.

[58] John C Stephens, Stanley W Artz, and Bruce N Ames. Guanosine 5'-diphosphate 3'-diphosphate (ppGpp): positive effector for histidine operon transcription and general signal for amino-acid deficiency. *Proceedings of the National Academy of Sciences*, 72(11):4389–4393, 1975.

[59] Jose Sy and Fritz Lipmann. Identification of the synthesis of guanosine tetraphosphate (MS I) as insertion of a pyrophosphoryl group into the 3'-position in guanosine 5'-diphosphate. *Proceedings of the National Academy of Sciences*, 70(2):306–309, 1973.

[60] Thomas M. Wendrich, Gregor Blaha, Daniel N. Wilson, Mohamed A. Marahiel, and Knud H. Nierhaus. Dissection of the mechanism for the stringent factor RelA. *Molecular Cell*, 10(4):779–788, 2002.

[61] William A. Haseltine, Ricardo Block, Walter Gilbert, and Klaus Weber. MSI and MSII made on ribosome in idling step of protein synthesis. *Nature*, 238(5364):381–384, 1972. 10.1038/238381a0.

[62] William A. Haseltine and Ricardo Block. Synthesis of guanosine tetra- and pentaphosphate requires the presence of a codon-specific, uncharged transfer ribonucleic acid in the

acceptor site of ribosomes. *Proceedings of the National Academy of Sciences*, 70(5):1564–1568, 1973.

[63] Larissa Brown, Daniel Gentry, Thomas Elliott, and Michael Cashel. DksA affects ppGpp induction of RpoS at a translational level. *Journal of bacteriology*, 184(16):4455–4465, 2002.

[64] Lisa U Magnusson, Bertil Gummesson, Predrag Joksimović, Anne Farewell, and Thomas Nyström. Identical, independent, and opposing roles of ppGpp and DksA in *Escherichia coli*. *Journal of bacteriology*, 189(14):5193–5202, 2007.

[65] Anna Perederina, Vladimir Svetlov, Marina N Vassylyeva, Tahir H Tahirov, Shigeyuki Yokoyama, Irina Artsimovitch, and Dmitry G Vassylyev. Regulation through the secondary channel-structural framework for ppGpp-DksA synergism during transcription. *Cell*, 118(3):297–309, 2004.

[66] Brian J. Paul, Wilma Ross, Tamas Gaal, and Richard L. Gourse. rRNA transcription in *Escherichia coli*. *Annual Review of Genetics*, 38(1):749–770, 2004.

[67] M. Kajitani and A. Ishihama. Promoter selectivity of *Escherichia coli* RNA polymerase. Differential stringent control of the multiple promoters from ribosomal RNA and protein operons. *J Biol Chem*, 259(3):1951–7, 1984.

[68] Melanie M Barker, Tamas Gaal, Cathleen A Josaitis, and Richard L Gourse. Mechanism of regulation of transcription initiation by ppGpp. I. Effects of ppGpp on transcription initiation in vivo and in vitro. *Journal of molecular biology*, 305(4):673–688, 2001.

[69] Andrew D. Laurie, Lisandro M. D. Bernardo, Chun Chau Sze, Eleonore Skärfstad, Agnieszka Szalewska-Palasz, Thomas Nyström, and Victoria Shingler. The role of the alarmone (p)ppGpp in σ^N competition for core RNA polymerase. *Journal of Biological Chemistry*, 278(3):1494–1503, 2003.

[70] Miki Jishage, Kristian Kvint, Victoria Shingler, and Thomas Nyström. Regulation of σ factor competition by the alarmone ppGpp. *Genes & Development*, 16(10):1260–1270, 2002.

[71] Thomas Nyström. MicroReview: Growth versus maintenance: a trade-off dictated by RNA polymerase availability and sigma factor competition? *Molecular Microbiology*, 54(4):855–862, 2004.

[72] Lisa U. Magnusson, Anne Farewell, and Thomas Nyström. ppGpp: a global regulator in *Escherichia coli*. *Trends in Microbiology*, 13(5):236 – 242, 2005.

[73] J. E. Cabrera and D. J. Jin. The distribution of RNA polymerase in *Escherichia coli* is dynamic and sensitive to environmental cues. *Mol Microbiol*, 50(5):1493–505, 2003.

[74] Photometric assay for measuring the intracellular concentration of branched-chain amino acids in bacteria. *Journal of Microbiological Methods*, 56(1):133 – 136, 2004.

[75] H. Eagle, K. A. Piez, and M. Levy. The intracellular amino acid concentrations required for protein synthesis in cultured human cells. *J Biol Chem*, 236:2039–42, 1961.

[76] Eliora Z Ron, Sonia Rozenhak, and NILI Grossman. Synchronization of cell division in *Escherichia coli* by amino acid starvation: strain specificity. *Journal of Bacteriology*, 123(1):374–376, 1975. 1095561[pmid] J Bacteriol.

[77] E Ron, NILI Grossman, and CHARLES E Helmstetter. Control of cell division in *Escherichia coli*: effect of amino acid starvation. *Journal of bacteriology*, 129(2):569–573, 1977.

[78] Nili Grossman, Eliora Z Ron, and Conrad L Woldringh. Changes in cell dimensions during amino acid starvation of *Escherichia coli*. *J Bacteriol*, 152(1):35–41, 1982.

[79] Cedric Cagliero and Ding Jun Jin. Dissociation and re-association of RNA polymerase with DNA during osmotic stress response in *Escherichia coli*. *Nucleic acids research*, page gks988, 2012.

[80] Y. Magariyama, S. Suglyama, K. Muramotor, Y. Maekawa, I. Kawagishi, Y. Imae, and S. Kudo. Very fast flagellar rotation. *Nature*, 371:752, 1994.

[81] Suddhashil Chattopadhyay and Xiao-Lun Wu. The effect of long-range hydrodynamic interaction on the swimming of a single bacterium. *Biophysical Journal*, 96(5):2023–2028, 2009.

[82] H. P. Grossart, G. F. Steward, J. Martinez, and F. Azam. A simple, rapid method for demonstrating bacterial flagella. *Appl Environ Microbiol*, 66(8):3632–6, 2000.

[83] J Gray and GJ Hancock. The propulsion of sea-urchin spermatozoa. *Journal of Experimental Biology*, 32(4):802–814, 1955.

[84] James Lighthill. Flagellar hydrodynamics. *SIAM review*, 18(2):161–230, 1976.

[85] Alfred Shapere and Frank Wilczek. Gauge kinematics of deformable bodies. *Am. J. Phys*, 57(6):514–518, 1989.

[86] Li Xie, Tuba Altindal, Suddhashil Chattopadhyay, and Xiao-Lun Wu. Bacterial flagellum as a propeller and as a rudder for efficient chemotaxis. *Proceedings of the National Academy of Sciences*, 108(6):2246–2251, 2011.

[87] Y. Sowa, H. Hotta, M. Homma, and A. Ishijima. Torque-speed relationship of the Na^+-driven flagellar motor of *Vibrio alginolyticus*. *J Mol Biol*, 327(5):1043–51, 2003.

[88] Li Xie, Chunliang Lu, and Xiao-Lun Wu. Marine bacterial chemoresponse to a stepwise chemoattractant stimulus. *Biophysical Journal*, 108(3):766–774, 2014.

[89] Hemang Thakor, Sarah Nicholas, Ian M. Porter, Nicole Hand, and Richard C. Stewart. Identification of an anchor residue for CheA-CheY interactions in the chemotaxis system of *Escherichia coli*. *Journal of Bacteriology*, 193(15):3894–3903, 2011.

[90] Yun-Kyeong Kim and Linda L. McCarter. Analysis of the polar flagellar gene system of *Vibrio parahaemolyticus*. *Journal of Bacteriology*, 182(13):3693–3704, 2000.

[91] Hiroyuki Terashima, Hajime Fukuoka, Toshiharu Yakushi, Seiji Kojima, and Michio Homma. The vibrio motor proteins, *MotX and MotY*, are associated with the basal body of Na^+-driven flagella and required for stator formation. *Molecular Microbiology*, 62(4):1170–1180, 2006.

[92] Pushkar P Lele, Richard W Branch, Vedhavalli SJ Nathan, and Howard C Berg. Mechanism for adaptive remodeling of the bacterial flagellar switch. *Proceedings of the National Academy of Sciences*, 109(49):20018–20022, 2012.

[93] Pushkar P. Lele, Basarab G. Hosu, and Howard C. Berg. Dynamics of mechanosensing in the bacterial flagellar motor. *Proceedings of the National Academy of Sciences*, 110(29):11839–11844, 2013.

[94] Nicolas J. Delalez, Richard M. Berry, and Judith P. Armitage. Stoichiometry and turnover of the bacterial flagellar switch protein FliN. *mBio*, 5(4), 2014.

[95] J. Yuan, R. W. Branch, B. G. Hosu, and H. C. Berg. Adaptation at the output of the chemotaxis signalling pathway. *Nature*, 484(7393):233–6, 2012.

[96] I. Kawagishi, Y. Maekawa, T. Atsumi, M. Homma, and Y. Imae. Isolation of the polar and lateral flagellum-defective mutants in *Vibrio alginolyticus* and identification of their flagellar driving energy sources. *Journal of Bacteriology*, 177(17):5158–5160, 1995.